



Universitat Autònoma de Barcelona

ADVERTIMENT. L'accés als continguts d'aquesta tesi queda condicionat a l'acceptació de les condicions d'ús establertes per la següent llicència Creative Commons:  http://cat.creativecommons.org/?page_id=184

ADVERTENCIA. El acceso a los contenidos de esta tesis queda condicionado a la aceptación de las condiciones de uso establecidas por la siguiente licencia Creative Commons:  <http://es.creativecommons.org/blog/licencias/>

WARNING. The access to the contents of this doctoral thesis it is limited to the acceptance of the use conditions set by the following Creative Commons license:  <https://creativecommons.org/licenses/?lang=en>



**Universitat Autònoma
de Barcelona**

**STUDIES ON As AND Sb OXOANIONS
ADSORPTION**

**Use of mass spectroscopy and synchrotron
techniques on process characterisation**

Verónica Verdugo Andrés

Tesis doctoral

Doctorado en Química

Directores: Manuel Valiente Malmagro

Cristina Palet Ballús

Departamento de Química

Facultad de Ciencias

2019



Memoria presentada para aspirar al Grado de Doctor por

Verónica Verdugo Andrés

Visto bueno, los supervisores

Dr. Manuel Valiente Malmagro

Dra. Cristina Palet Ballús

Bellaterra (Cerdanyola del Vallés) a 3 de Junio de 2019



**Universitat Autònoma
de Barcelona**

The work presented in this PhD thesis has been developed under support of the following projects:

- *“Technological evolution of chemical speciation and synchrotron technologies for the characterization and development of environmental systems and biomaterials” (CHEMSYNCHRO)*. CTM2012-30970. R&D National Project supported by Ministerio de Educación y Ciencia de España
- *“Especiación química: de medio ambiente a la salud, un enfoque nexus” (CHEMNEXUS)* CTM2015-65414-C2-1-R. . R&D National Project supported by Ministerio de Educación y Ciencia de España.
- *“Advanced multifunctional nanostructured materials applied to remove arsenic in argentinian groundwater” (NANOREMOVAS)* H2020-MSCA-RISE-2014, Project Number 645024.

Moreover, I would like to thank:

- Generalitat de Catalunya, for the Pre-Doctoral grant “FI-2015” (2015-2018)
- NANOREMOVAS Project and Instituto de Investigaciones en Ciencia y Tecnología de Materiales (INTEMA), especially to Ceramic división for a 3 months stay under the supervisión of Raul A. Procaccini.
- DEPRO research group, Chemistry Engineering and Biomolecular Department in Univerisdad de Cantabria for a 1 mothn stay under the supervision of Jonathan Albo and Manuel Alvarez Guerra
- European Synchrotron Radiation Facility (ESRF, Grenoble, France), for the possibility to develop the experiments in their installations, especially, to the Beamline BM-25 and to Eduardo Salas Colera for his technical support.
- ALBA Synchrotron (Cerdanyola del Valles, Barcelona, Spain), for the possibility to develop the experiments in their installations, especially, to the CLAESS Beamline and MIRAS beamline and Carlo Marini, Wojciech Olszewski, Nitya Ramanan and Ibraheem Youseff for their technical support.
- Following laboratory services: Servei de Microscòpia (UAB), Servei de Difracció de Raigs X (UAB), Catalan Institute of Nanoscience and Nanotechnology (ICN2), Institut de Ciència de Materials de Barcelona (ICMAB-CSIC), for their availability to perform experiments in their facilities.

In addition, the congresses and scientific meeting where the PhD thesis results have been presented are detailed:

- **Novena trobada de Joves Investigadors dels Països Catalans.** Oral Communication *“Advance antimony recovery materials based on Superparamagnetic iron oxide Nanoparticles (SPION)”*. 3rd to 5th February 2016. Perpignan (France)
- **2016 International Symposium on Metal Complexes (ISMEC).** Poster Communication. *“Effective removal of antimony from aqueous solution using Forager sponge[®] and SPION-loaded onto Forager sponge[®]”*. 7th to 10th June 2016. Barcelona (Spain)
- **International Conference on Chemistry and the Environment 2017 (ICCE 2017).** Poster Communication. *“Efficient Sb(III)/Sb(V) Adsorption by SPION Supported on Metalzorb[®] Sponge”*. 18th to 21st June 2017. Oslo (Norway).
- **XXXVI Reunión Bienal de la Real Sociedad Española de Química.** Oral Communication *“Adsorption mechanisms on Metalzorb[®] sponge and SPION-Metalzorb[®] system”*. 25th to 29th June 2017. Sitges (Barcelona)
- **10th World Congress of Chemical Engineering.** Poster Communication. *“Influence of oxidation state in Arsenic adsorption-desorption on Metalzorb[®] sponge”*. 1st to 5th June 2017. Barcelona (Spain)

SUMMARY

The studies that have been carried out in the present PhD thesis Project are based on the development of an improved adsorption process for oxoanions removal, specifically arsenic and antimony due to their toxicity and commercial value. The upgrades are focused on the possibility of adsorbent reuse (As), and on synthetic methods that could endow materials scientists with tools to precisely tailor their structures/pores and have accurate control of adsorption (Sb). For this, adsorption-desorption studies of arsenic and antimony have been performed using a commercial polymeric adsorbent, Metalzorb[®] sponge, and its modification by SuperParamagnetic Iron Oxide Nanoparticles (SPION).

Adsorption-desorption studies will be performed in batch mode. Analytical techniques (ICP-MS, UV-Vis spectrometry) were used to obtain information regarding the Sb and As content in solution. Microscopy techniques (TEM and SEM) were applied to characterise the nanoparticles. Spectroscopic techniques (FTIR and XAS) were used to characterise the adsorption process mechanisms.

Arsenic desorption process has been performed by applying an electrochemical potential to the solution containing the adsorbent loaded with As(V) to achieve its reduction to As(III) and its desorption from Metalzorb[®] sponge. This reduction process is not possible without a chemical reagent. The use of inert electrodes does not produce any As(V) reduction. Whereas a combination of Sn and Sn coating on stainless steel mesh as working and counter electrode, respectively, present the best results (60% of As(V) reduction), also forming a white precipitate (As-Sn compound properly characterised), which indicate that Sn plays a key role in As removal.

Concerning the Metalzorb[®] sponge, a new application of enhanced adsorbent material for Sb removal is envisaged. The pathway used for SPION loaded into sponge influences the physicochemical properties of the adsorbent and the sorption process. Among the different synthesis evaluated, direct synthesis shows the best characteristics, producing SPION nanoparticles diffusion inside of the matrix of the sponge, increasing the adsorbent stability and their sorption properties. Furthermore, it is the fastest adsorbent due to the NP placement on the external sponge surface, as well as the presence of smaller NPs internally (≈ 4.75 nm). There is an increase of the adsorption sites, creating a larger contact area between loaded-SPION/target solution, and enhancing the adsorption kinetics and producing a decrease in the diffusion layer.

Comparison of this material with Metalzorb[®] sponge suggest that both are appropriate adsorbents for antimony (Sb(III) and Sb(V)). However, the presence of SPION improves the removal process enhancing bare sponge adsorption properties. Sb adsorption on the sponge is influenced by pH, contact time, initial concentration and temperature. The strong pH influence, S-type isotherm profiles, the strong effect of interfering anions, and the easy chemical desorption using ionic and complexation stripping agents indicate that Sb(III) and Sb(V) are adsorbed to the sponge by weak interactions. The presence of SPION reduce the pH influence and the influence of interfering anions and shows an L-type isotherm. These evidence, together with almost inexistent desorption with the stripping agent used indicates that Sb(III) and Sb(V) are adsorbed to the sponge+SPION system by strong interactions. XAS and FTIR measurements

confirm these results. With a lower affinity, Sb(III) and Sb(V) are absorbed into the bare sponge through H-bonding and electrostatic interaction, which indicates the formation of outer-sphere complexes. The presence of SPION facilitates the formation of the Fe-O-Sb bonds. For Sb(III), adsorption is independent of the pH, indicating that inner-sphere complexes are formed with a partial Sb(III) oxidation. On the contrary, Sb(V) adsorption depends on the pH, reducing its sorption capacity up to 40 % when the pH increases from 8 to 9. This pH dependency indicates that inner- and outer-sphere complexes are generated during Sb(V) adsorption.

RESUMEN

Los estudios que se han llevado a cabo en la presente tesis doctoral se basan en el desarrollo de mejoras del proceso de adsorción para la eliminación de oxoaniones, en concreto arsénico y antimonio, por su toxicidad y valor comercial. Las mejoras se centran en la posibilidad de reutilizar el adsorbente (arsénico), y en los métodos sintéticos de adsorbentes que permitan controlar el proceso de adsorción (antimonio). Para ello, se han realizado estudios de adsorción-desorción en discontinuo, de ambos oxoaniones, utilizando un adsorbente comercial polimérico, Metalzorb® sponge y su modificación mediante Nanopartículas de Oxidos de Hierro Superparamagnéticos (SPION). Diferentes técnicas analíticas (ICP-MS, espectrofotometría UV-Vis) se han utilizado para obtener la concentración de As y Sb en las disoluciones. Técnicas de microscopía como SEM y TEM se aplicaron para la caracterización de las nanopartículas y diferentes técnicas espectroscópicas (FTIR y XAS) han sido utilizadas para caracterizar el proceso de adsorción y su mecanismo.

La desorción del As se ha llevado a cabo mediante la aplicación de un potencial a una solución que contenía la esponja cargada con As(V), para intentar reducirlo a As(III) y con ello conseguir su desorción de la esponja. No ha sido posible llevar a cabo este proceso de reducción sin un reactivo químico que actúe como agente reductor. El uso de electrodos inertes no ha dado resultados favorables. Los mejores resultados se han obtenido con el uso combinado de un electrodo de estaño y una rejilla de acero recubierta de estaño como electrodos de trabajo y contraelectrodo, respectivamente, alcanzando un 60% de eliminación de As. Durante este proceso se observa la formación de un precipitado blanco (compuesto por As y Sn) que indica que el estaño juega un papel clave en este proceso.

En relación con la esponja, se ha desarrollado un nuevo material como adsorbente para la eliminación de Sb. La forma de inmovilizar el SPION en la esponja influye en las propiedades fisicoquímicas del adsorbente y en el proceso de adsorción. Entre las diferentes síntesis evaluadas, la síntesis del SPION directamente sobre la superficie de la esponja presenta las mejores características, ya que favorece la difusión de las nanopartículas en la matriz de la esponja, aumentando la estabilidad del adsorbente y mejorando su capacidad de adsorción. Además, presenta la cinética de adsorción más rápida debido a la presencia de nanopartículas tanto en la superficie como en el interior (≈ 4.75 nm), aumentando la superficie de contacto entre el SPION de la esponja con la solución de antimonio, y mejorando tanto la cinética de adsorción como el proceso de difusión.

La comparación de este material con la esponja sugiere que ambos materiales son adecuados para la adsorción de Sb (Sb(III) y Sb(V)). Sin embargo, la presencia de SPION mejora el proceso. La adsorción del Sb en la esponja esta fuertemente influenciada por el pH, el tiempo de contacto, la concentración inicial y la temperatura. Esto, junto a su fácil desorción mediante compuestos aniónicos y agentes complejantes en solución indica que el Sb(III) y el Sb(V) interactúan débilmente con la esponja. La presencia del SPION disminuye la dependencia de la adsorción de Sb de estos factores, lo que junto a su difícil desorción, indica que interactúa de una forma más estable con el SPION. Las medidas de XAS y FTIR confirman estos resultados. El Sb(III) y Sb(V) debido a su menor afinidad en la esponja modificada se absorben en la esponja a través de puentes de H o interacciones electrostáticas, lo que indica la formación de complejos de esfera externa. La presencia del SPION facilita la formación de enlaces Fe-O-Sb, formándose complejos de esfera interna.

INDEX

ABBREVIATIONS

CHAPTER 1. GENERAL INTRODUCTION

1. BACKGROUND	3
2. PROBLEM DESCRIPTION	4
3. RESEARCH OBJECTIVES.....	6
4. STRUCTURE OF THE THESIS.....	6
5. REFERENCES	9

PART 1. ARSENIC

CHAPTER 2. ELECTROCHEMICAL REGENERATION FOR ARSENIC REMOVAL

Under patent protection

PART 2. ANTIMONY

CHAPTER 3. ANTIMONY: ENVIRONMENTAL SIGNIFICANCE, POLLUTION AND REMOVAL TECHNIQUES

1. INTRODUCTION	19
Why is antimony important?	19
2. ANTIMONY CHEMISTRY.....	20
2.1. Sb redox chemistry.....	22
2.2. Complexation with Dissolved Organic Ligands	24
3. GLOBAL MARKET AND USES OF Sb.....	25
4. ANTIMONY IN THE ENVIRONMENT.....	27
5. ANTIMONY TOXICITY AND HEALTH EFFECTS	28
6. OVERVIEW OF ANTIMONY REMOVAL TECHNOLOGIES.....	30
7. CONCLUSIONS	36
8. REFERENCES	36

CHAPTER 4. OPTIMIZATION AND CHARACTERIZATION OF SUPERPARAMAGNETIC IRON OXIDE (SPION) ADSORBENT FOR ANTIMONY REMOVAL

Under patent protection

CHAPTER 5. CHARACTERISATION OF Sb(III) AND Sb(V) SORPTION PROCESS ON THE SPONGE AND SPONGE+SPION SYSTEM

Under patent protection

CHAPTER 6 SPECTROSCOPIC STUDY OF THE ADSORPTION OF Sb(III) AND Sb(V) ON SPONGE-SPION-DIRECT SYSTEM

1. INTRODUCTION	49
1.1. Adsorption mechanism	50
1.2. Metal oxide surface in water	51
1.3. Adsorption on inorganic species by metal oxide materials	52
1.4. Spectroscopy method for sorption mechanism determination.....	54
2. OBJECTIVES.....	56
3. MATERIALS AND METHOD	57
3.1. Chemicals and reagents	57
3.2. Synthesis of adsorbent materials.....	57
3.2.1. Sponge pretreatment.....	57
3.2.2. Sponge+SPION system synthesis.....	57
3.3. Adsorption experiments.....	58
3.4. Characterisation	58
4. RESULTS.....	60
4.1. pH influence	60
4.2. FTIR analysis	64
4.3. XAS measurements	68
4.4. Sorption mechanism	72
5. CONCLUSIONS	76
6. REFERENCES	77

CONCLUSIONS

CHAPTER 7 GENERAL CONCLUSIONS

1. CONCLUSIONS	85
Chapter 2. Electrochemical regeneration for arsenic removal	85
Chapter 3. Antimony environmental significance pollution and removal techniques	85
Chapter 4. Optimisation and characterisation of superparamagnetic iron oxide (SPION) adsorbent for antimony removal	86
Chapter 5. Characterisation of Sb(III) and Sb(V) sorption process on the sponge and sponge+spion system	86
Chapter 6. Spectroscopic study of the adsorption mechanism of Sb(III) and Sb(V) on Sponge- SPION-direct system.....	86
2. FUTURE PERSPECTIVES.....	87

ANNEXES

Annexe 1. INSTRUMENTAL TECHNIQUES.....	92
Annexe 2. ELECTROCHEMICAL SETUP REVIEW ¹⁻³	116
Annexe 3. MAGNETISM.....	120
Annex 4. KINETIC AND ISOTHERM MODEL	128
Annexe 5. COMPLEXATION CONSTANTS.....	136

ABBREVIATIONS

BET	Brunauer–Emmett–Teller
CE	Counter Electrode
CRM	Critical Raw Material
CV	Cyclic Voltammetry
EC	Electrocoagulation
EDS	Energy Dispersive Spectrometer
EDTA	Ethylenediaminetetraacetic acid
EPDM	Ethylene Propylene Diene Monomer
EXAFS	Extended X-Ray Absorption Fine Structure
FC	Field Cooling
FP-XRF	Field Portable X-Ray Fluorescence spectrometry
FTIR	Fourier-transform Infrared spectroscopy
GAB	Guggenheim, Anderson and de Boer
HRTEM	High resolution Transmission Electron Microscopy
ICP-MS	Inductively Coupled Plasma Mass Spectrometry
IPDM	IntraParticle Diffusion Model
LA	Lead Acid Batteries
NP	Nanoparticle
PET	Polyethylene Terephthalate
PFO	Pseudo first order model
PSO	Pseudo second order model
PVDF	Polyvinylidene Fluoride
RE	Reference Electrode
SCE	Saturated Calomel Electrode
SEM	Scanning Electron Microscopy
SG	Savitzky–Golay
SPION	SuperParamagnetic Iron Oxide Nanoparticles
SQUID	Superconducting Quantum interference Device
TEM	Transmission electron Microscopy
TGA	Thermogravimetric analysis
TMAOH	Savitzky–Golay
WE	Working Electrode
XAS	X-Ray Absorption spectroscopy

XANES	X-Ray Absorption Near Edge Structure
XPS	X-Ray Photoelectron Spectroscopy
XRD	X-Ray Diffraction
ZFC	Zero Field cooling

CHAPTER 1

GENERAL INTRODUCTION

1. BACKGROUND.....	3
2. PROBLEM DESCRIPTION.....	4
3. RESEARCH OBJECTIVES	6
4. STRUCTURE OF THE THESIS	6
5. REFERENCES.....	9

1. BACKGROUND

The removal and recovery of metals and metalloids from soils and waters are important due to their toxicity (i.e., chromium, arsenic, antimony, platinum, among others) and/or their commercial value as a result of their inclusion in the Critical Raw Material (CRM) European list. The CRM list includes those raw materials which are economically and strategically important for the European economy but have a high-risk associated with their supply¹, such as antimony, indium or vanadium, and their recovery is essential.

Intensive industrial development has contributed to the increased pollution of the environment with these hazardous metals and metalloids. Most of these elements are redox sensitive, and some of their oxidation states can form oxyanions in solution². Oxyanions (or oxoanions) are polyatomic negatively charged ions containing oxygen with the general formula $AxOy^{z-}$ (where A represents a chemical element and O represents an oxygen atom) which are characterised by a central atom, A, which is a Lewis acid³. Those compounds represent a range of different species depending both on pH and redox potential⁴. Oxyanions of As, Se, Sb, Cr, V and Mo are commonly found trace pollutants in various waste streams², accompanied by large amounts of more common anions (CO_3^{2-} , Cl^- , NO_3^- , PO_4^{3-} and SO_4^{2-})⁵. These oxyanions have considerable commercial value as a result of their various industrial applications and some present significant environmental challenges because of their toxicity towards living organisms⁵.

Sources of oxyanions contamination in the environment can come from both anthropogenic activities and natural geochemical cycles. The main sources of hazardous oxyanions are alkaline wastes originating from high-temperature processes with the thermal treatment of waste, fossil fuel combustion, and ferrous or non-ferrous metal smelting⁴. However, they are also produced in microelectronics, electroplating, metal finishing, battery manufacturing, tannery, metallurgy, and fertiliser and pesticides industries^{2,6}. The anthropogenic pollution generated by these industrial activities joint to the natural pollution formations promotes dissolution of weak-acid oxyanion species, like arsenic, vanadium, or antimony, which pollute groundwater sources used by local communities. Past research initiatives and the legislation in waste management have focused on contaminants of high concentration and toxicity such as Cu, Cd, Hg, Pb and Zn whereas oxoanionic species have received considerably less attention because of their much lower total solid phase concentrations. However, they are often found in relatively high concentrations in leachates compared to the cationic species due to their high solubility⁴.

These metal and metalloid oxyanions are toxic, nonbiodegradable⁶⁻⁹ and present a high solubility in water¹⁰, which gives them the ability to bioaccumulate in the environment and the food chain¹⁰⁻¹². Thus, these species are hazardous even at low concentrations. They can be transferred into living organisms via inhalation, ingestion, and skin adsorption, causing irreversible effects⁶. Considering the harmful properties of metal and metalloid oxyanions, their effective elimination from water and wastewater is becoming a key issue for the environment and public health protection.

2. PROBLEM DESCRIPTION

A detailed study of the oxyanions removal is a very large experimental work and become unapproachable for a Spanish PhD thesis period. Therefore, a selection has been made taking into account both the previous work in our research group (mainly concerning As and Se) and the European Union priorities, previously indicated. For these reasons, arsenic and antimony, in wider extension, have been the target elements in the present studies. As and Sb are potentially toxic contaminants, with millions of individuals affected by As toxicosis and tens to hundreds of thousands of individuals likely affected by mine waste-derived Sb¹³. Both are metalloids, having properties of metals and non-metals, and belong to Group VA of the periodic table (third and fourth elements, respectively). These trace elements with similar chemistry and toxicity are naturally occurring and commonly present together^{14,15}.

Arsenic is mostly present in natural waters as dissolved As(III)-bearing species [As(OH)₃] or dissolved As(V)-bearing species [AsO(OH)₃] and dissociated species, with As(V) being considered less toxic^{6,13}. Typical concentrations of As in unpolluted waters are <10 µg/L and frequently <1 µg/L. On the other hand, typical Sb concentrations in unpolluted waters are <1 µg/L, but concentrations can reach 100 times these levels in areas close to anthropogenic sources¹⁶. Sb is present in natural waters as both dissolved Sb(III), predominantly as Sb(OH)₃, and dissolved Sb(V), predominantly as Sb(OH)₆⁻, the latter being considered less toxic^{13,16}.

Despite the naturally occurring of both elements in the environment, anthropogenic sources are the main responsible for their presence in the environment. The significance to human health and the impact in the environment have explained the recent increasing interest for arsenic and antimony abundance, behaviour and remediation¹⁷. Arsenic and antimony are both considered pollutants of priority interest by the European Union and by the Environmental Protection Agency of the United States. The World Health Organization (WHO) established, in 1993, 10 µg/L as the guideline value for arsenic in drinking water¹⁸. This value was defined considering the treatment performance, analytical achievability and the risks related to human health. For antimony, UE and USA limits are 5 µg/L and 6 µg/L, respectively^{17,18}. The more stringent maximum

contaminant level along with the severe contamination crisis occurring worldwide have driven researchers and authorities to upgrade treatment technologies to remove arsenic and antimony from waste streams¹⁹.

Existing technologies for water As and Sb remediation include precipitation, membrane technology, coagulation/flocculation, biological processes, advanced oxidation processes (AOPs) and adsorption¹⁷. Each method has advantages and inconveniences and, in some of them, there are decontamination protocols implemented in sequence to mitigate its drawbacks¹⁰. Conventional decontamination and disinfection methods, currently used, suffer from high operating cost and generation of secondary pollutants and, even more importantly, are not able to eliminate the generate waste of waters decontamination. Adsorption of pollutants with porous materials is a suitable alternative to remove contaminants from our water ecosystems in an efficient manner. Mesoporous clay materials, zeolites, bioadsorbents, polymeric resins and carbonaceous materials have demonstrated, to some extent, good performances towards different contaminants present in aqueous media. One of the main advantages of the adsorption process is the possibility of adsorbent reuse, enhancing the economical quotation in a real application. For this reason, it is necessary to accomplish for a cheap, easy and environmentally friendly desorption process integrated into the adsorption system to enable the adsorbent reuse. On the other hand, their main drawback is the lack of synthetic methods that could endow materials scientists with tools to precisely tailor their structures/pores, and consequently to provide an accurate control of the adsorption kinetics, capacity and selectivity for pollutants, which is of main relevance towards increasing the performances of adsorbents and implementing efficient water reclamation protocols¹⁰.

In order to enhance the adsorption advantages and to study a novel adsorbent, two main studies will be developed in this PhD thesis.

Initially, the As adsorption/desorption process for adsorbent reuse will be performed. A widely studied adsorbent, Metalzorb® sponge, will be employed²⁰⁻²². Previous studies have characterised the As adsorption process, indicating that As(V) present a higher affinity to this material than As(III). Thus, the desorption process has been designed, taking advantage of this affinity difference. Muñoz et al.²⁰ and Morillo et al.²² used chemical desorption whereas Liu et al.²³ improve the thermic and redox desorption using tin. The next step is used here, applying a potential to the solution containing the sponge loaded with As(V) in order to achieve the As reduction to As(III) followed with its desorption, facilitating and marking down the process.

As far as the adsorbent preparation is a concern, a novel material for Sb adsorption has been developed. It consists of the Metalzorb® sponge modification by loading SuperParamagnetic Iron Oxide Nanoparticles (SPION). This material has been previously and satisfactorily used for As adsorption, and its efficiency for Sb removal

has been described in the present study. Also, the synthesis pathway is evaluated in order to determine the conditions for a most favourable adsorbent and to characterise the interactions between SPION and the sponge.

3. RESEARCH OBJECTIVES

This research aims to provide a better understanding of the adsorption mechanism of oxoanions, mainly for Sb, on the sponge and sponge+SPION adsorbents, and to develop a new desorption process for the adsorbent reuse. To achieve these objectives, the followings tasks have been envisaged:

- 1) To demonstrate the feasibility of an electrochemical As(V) desorption system for the adsorbent regeneration taking advantage of the different As(III) and As(V) adsorption affinity
- 2) To study the interaction between SPION and the sponge to form the nanostructure adsorbent for Sb removal, identifying most appropriate synthesis pathway to obtain the highest adsorbent properties, and improving the technical weakness of the original material.
- 3) To evaluate the capacity of the sponge and sponge+SPION system to adsorb antimony, as Sb(III) and Sb(V) and their possible application to the recovery and removal of this metalloid with enhanced selectivity from wastewater effluent. To determine the optimal parameters and best conditions for the Sb removal in batch mode.
- 4) To elucidate the mechanisms of interaction between the sponge and the sponge+SPION system with Sb from aqueous systems, combining macroscopic and spectroscopic techniques.

4. STRUCTURE OF THE THESIS

The present studies are described in three blocks of contents containing seven chapters. An overview of the structure of this dissertation is given in Figure 1.1. The following paragraphs outline the content of the individual chapters.

Chapter 1 presents a general overview of this dissertation, including background, problem description, research objectives and thesis structure.

The first part contains the **Chapter 2**, which provides a literature review of As and previous studies about As adsorption-desorption process using Metalzorb® sponge as adsorbent material. Also, the investigation of the possible As(V) reduction to As(III) to produce the As desorption from the sponge, is here presented, together with the evaluation of the different operational conditions involved.

The second part contains **Chapter 3, 4, 5 and 6**, is focused on Sb adsorption/desorption processes. **Chapter 3** presents a literature review of the importance of Sb removal according to its toxicity, commercial value and available technologies for the remediation of Sb-laden wastewaters. The challenges and limitation encountered while applying Sb removal technology in practice are highlighted. **Chapter 4** gives an insight into the effect of the adsorbent preparation pathways on Sb adsorption capacity and establishing the methodology providing maximum adsorption in order to determine the preliminary working conditions to use the related materials as adsorbents. Characterisation of the different target materials is studied, and the interaction between the SPION and sponge that allows the SPION binding is also investigated. **Chapter 5** characterises Sb adsorption process in both adsorbents, studying kinetic and isotherm performance. The effect of different ions (most common anions present in water such as nitrates or sulphates and metallic cations) and temperature on Sb adsorption are also investigated. Finally, in this chapter is also evaluated the chemical Sb desorption using different anionic and complexant compounds as stripping agents. **Chapter 6** study the Sb adsorption mechanism in both adsorbents by including the results obtained in Chapter 5 with the characteristics of the pH influence on the adsorption process and the results of a XAS spectroscopy study.

Chapter 7 summarises the research performed and draws general and specific conclusions on the knowledge gained from this dissertation. It also discusses and recommends future research trends.

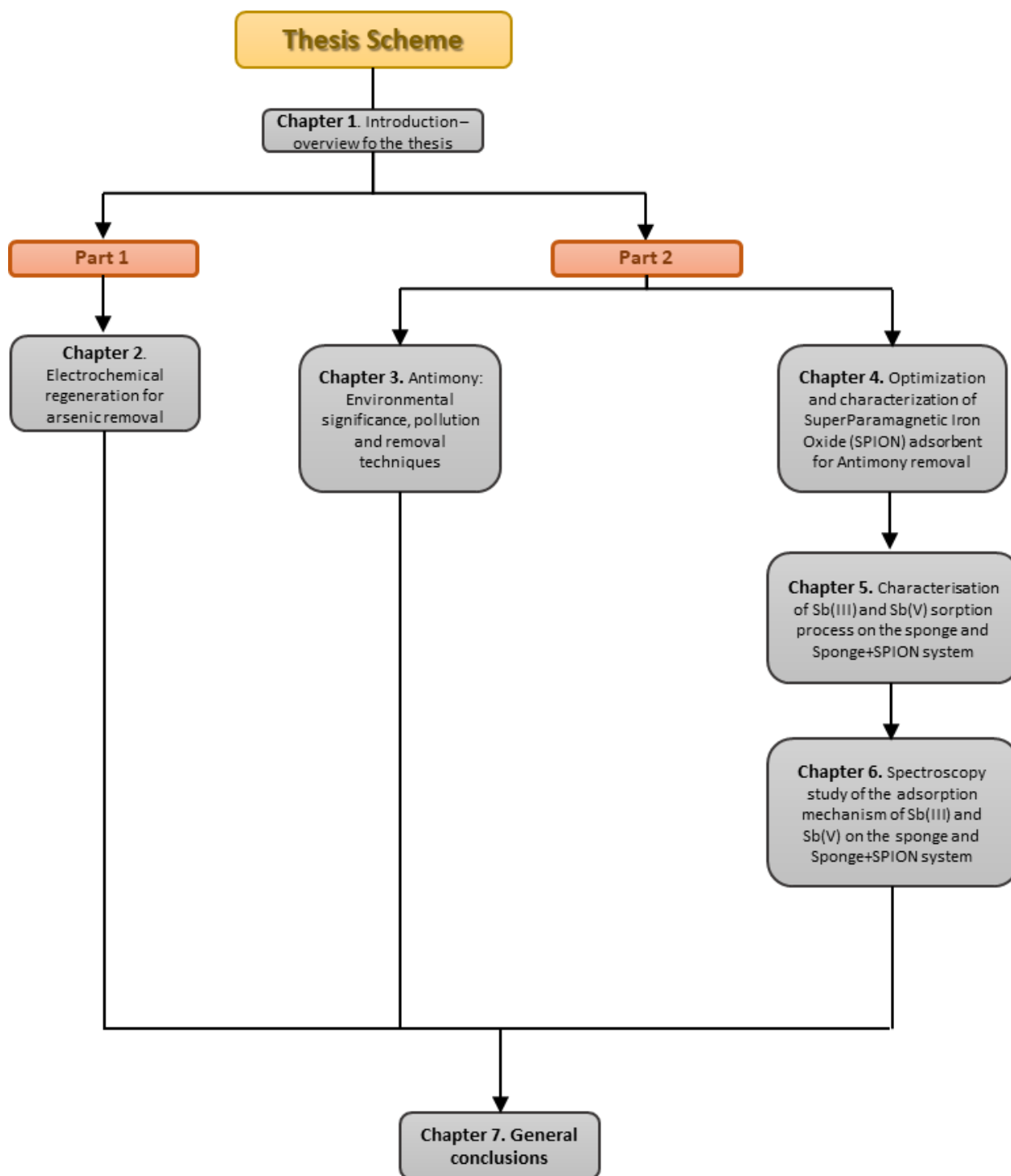


Figure 1.1. Overview of the chapters in this PhD thesis Chapter

5. REFERENCES

- (1) European Commission. *Study on the Review of the List of Critical Raw Materials*; 2017.
- (2) Weidner, E.; Ciesielczyk, F. Removal of Hazardous Oxyanions from the Environment Using Metal-Oxide-Based Materials. *Materials (Basel)*. **2019**, *12* (6), 927.
- (3) Adegoke, H. I.; Adekola, F. A.; Fatoki, O. S.; Ximba, B. J. Sorptive Interaction of Oxyanions with Iron Oxides: A Review. *Polish J. Environ. Stud.* **2013**, *22* (1), 7–24.
- (4) Cornelis, G.; Johnson, C. A.; Gerven, T. Van; Vandecasteele, C. Leaching Mechanisms of Oxyanionic Metalloid and Metal Species in Alkaline Solid Wastes: A Review. *Appl. Geochemistry* **2008**, *23* (5), 955–976.
- (5) Kailasam, V.; Rosenberg, E. Oxyanion Removal and Recovery Using Silica Polyamine Composites. *Hydrometallurgy* **2012**, *129–130*, 97–104.
- (6) Bhattacharya, P.; Jacks, G.; Frisbie, S. H.; Smith, E.; Naidu, R.; Sarkar, B. *Heavy Metals in the Environment*; Sarkar, B., Ed.; Marcel Dekker, 2002.
- (7) Wang, Y.; Ding, S.; Shi, L.; Gong, M.; Xu, S.; Zhang, C. Simultaneous Measurements of Cations and Anions Using Diffusive Gradients in Thin Films with a ZrO-Chelex Mixed Binding Layer. *Anal. Chim. Acta* **2017**, *972*, 1–11.
- (8) Hajji, S.; Montes-Hernandez, G.; Sarret, G.; Tordo, A.; Morin, G.; Ona-Nguema, G.; Bureau, S.; Turki, T.; Mzoughi, N. Arsenite and Chromate Sequestration onto Ferrihydrite, Siderite and Goethite Nanostructured Minerals: Isotherms from Flow-through Reactor Experiments and XAS Measurements. *J. Hazard. Mater.* **2019**, *362* (June 2018), 358–367.
- (9) Verbinnen, B.; Block, C.; Van Caneghem, J.; Vandecasteele, C. Recycling of Spent Adsorbents for Oxyanions and Heavy Metal Ions in the Production of Ceramics. *Waste Manag.* **2015**, *45*, 407–411.
- (10) Mon, M.; Bruno, R.; Ferrando-Soria, J.; Armentano, D.; Pardo, E. Metal-Organic Framework Technologies for Water Remediation: Towards a Sustainable Ecosystem. *J. Mater. Chem. A* **2018**, *6* (12), 4912–4947.
- (11) Zghida, H.; Baouab, M. H. V.; Gauthier, R. Sorption of Chromium Oxy-Anions onto Cationized Ligno-Cellulosic Material. *J. Appl. Polym. Sci.* **2003**, *87* (10), 1660–1665.
- (12) Galal-Gorchev, H. Dietary Intake, Levels in Food and Estimated Intake of Lead, Cadmium, and Mercury. *Food Addit. Contam.* **1993**, *10* (1), 115–128.
- (13) Cidu, R.; Dore, E.; Biddau, R.; Nordstrom, D. K. Fate of Antimony and Arsenic in Contaminated Waters at the Abandoned Su Suergiu Mine (Sardinia, Italy). *Mine Water Environ.* **2017**, *37* (1), 151–165.
- (14) Lehr, C. R.; Kashyap, D. R.; McDermott, T. R. New Insights into Microbial Oxidation of Antimony and Arsenic. *Appl. Environ. Microbiol.* **2007**, *73* (7), 2386–2389. <https://doi.org/10.1128/AEM.02789-06>.
- (15) An, Y. J.; Kim, M. Effect of Antimony on the Microbial Growth and the Activities of Soil Enzymes. *Chemosphere* **2009**, *74* (5), 654–659.
- (16) Filella, M.; Belzile, N.; Chen, Y.-W. Antimony in the Environment: A Review Focused on Natural Waters II. *Earth-Science Rev.* **2002**, *59* (1–4), 265–285.
- (17) Ungureanu, G.; Santos, S.; Boaventura, R.; Botelho, C. Arsenic and Antimony in Water and Wastewater: Overview of Removal Techniques with Special Reference to Latest Advances in Adsorption. *J. Environ. Manage.* **2015**, *151*, 326–342.

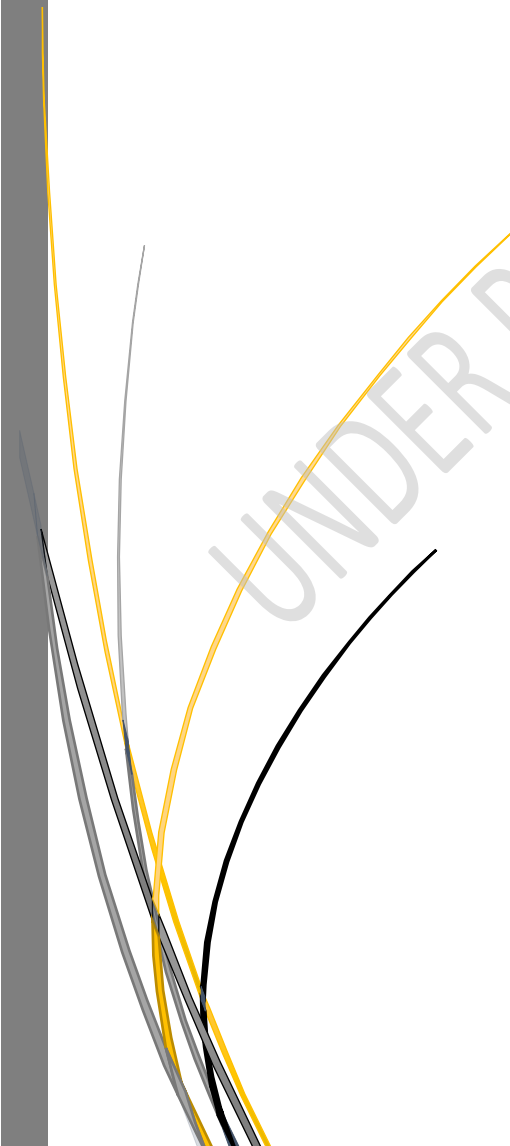
- (18) World Health Organization. *Guidelines for Drinking Water Quality. 4th Ed.*; 2011.
- (19) Lan, B.; Wang, Y.; Wang, X.; Zhou, X.; Kang, Y.; Li, L. Aqueous Arsenic (As) and Antimony (Sb) Removal by Potassium Ferrate. *Chem. Eng. J.* **2016**, *292*, 389–397.
- (20) Muñoz, J. A.; Gonzalo, A.; Valiente, M. Arsenic Adsorption by Fe(III)-Loaded Open-Celled Cellulose Sponge. Thermodynamic and Selectivity Aspects. *Environ. Sci. Technol.* **2002**, *36* (15), 3405–3411.
- (21) Muñoz, J. A.; Gonzalo, A.; Valiente, M. Kinetic and Dynamic Aspects of Arsenic Adsorption by Fe(III)-Loaded Sponge. *J. Solution Chem.* **2008**, *37* (4), 553–565.
- (22) Morillo, D.; Pérez, G.; Valiente, M. Efficient Arsenic(V) and Arsenic(III) Removal from Acidic Solutions with Novel Forager Sponge-Loaded Superparamagnetic Iron Oxide Nanoparticles. *J. Colloid Interface Sci.* **2015**, *453*, 132–141.
- (23) He, L. Development of Reagent-Less Processes for Water Decontamination. Tuning of Temperature and Redox Parameters to Remove Toxic Oxyanions., 2015.

PART 1. ARSENIC

CHAPTER 2

ELECTROCHEMICAL REGENERATION FOR ARSENIC REMOVAL

UNDER PATENT PROTECTION



PART 2. ANTIMONY

CHAPTER 3

ANTIMONY: ENVIRONMENTAL SIGNIFICANCE, POLLUTION AND REMOVAL TECHNIQUES

1. INTRODUCTION.....	65
Why is antimony important?.....	65
2. ANTIMONY CHEMISTRY	66
2.1. Sb redox chemistry	68
2.2. Complexation with Dissolved Organic Ligands.....	70
3. GLOBAL MARKET AND USES OF Sb.....	71
4. ANTIMONY IN THE ENVIRONMENT	73

1. INTRODUCTION

Antimony (Sb) is a natural element, located in group 15 of the periodic table, just after arsenic, which occurs naturally in rocks, water and soils at the levels of 0.15-2 mg/kg, < 1 mg/mL and 0.3-8.6 mg/kg, respectively^{1,2}. However, Sb can be present at elevated concentrations in different natural compartments due to its mobilisation from minerals and related rocks as well as human-induced activities such as mining, military training, smelting and use of pharmaceuticals and pesticides².

The history of Sb goes back to Ancient Egypt, where it was used as a cosmetic. However, until the 16th century, it was not properly isolated. Nowadays it is used in a wide variety of products and processes. Its production comes from stibnite ore (Sb_2S_3) but also occurs as oxide (Sb_2O_3), and as antimonides and sulphoantimonides of different metals (lead, copper, zinc, silver, or gold). Due to the industrial demand and the fact that over 90% of the supplies of this metalloid comes from China, there is a growing interest in Sb removal and recovery, so the European Union and EE.UU are import-dependent of this product³.

These observations have led the European Commission to highlight antimony as a critical raw material in 2014, with an expected supply-demand gap exceeding 10 % over the period 2015–2020, which is the highest amongst all critical metals⁴.

Apart from this, Sb has no beneficial biological role. It has high acute toxicity, can induce chronic health effects and is a potential carcinogenic. Due to their toxicity, Sb compounds are considered pollutants of primary concern by the Environmental Protection Agency and the Council of the European Communities. The European Union established a maximum admissible concentration of antimony in drinking water of 5 $\mu\text{g/L}$, and USEPA set the national primary drinking water standard at 6 mg/L ⁵.

Why is antimony important?

In the past, antimony was not considered as a worrying component in wastewater treatment compared to heavy metal contaminants or organic pollutants. However, the awareness concerning antimony pollution has increased in recent years due to the more studies related to its toxicity. Countries of particular concern where the contamination of Sb has been described so far to be significantly associated with geogenic sources, such as mine ores, geothermal and volcanic systems include the USA, China, Australia, New Zealand, Japan, Mexico, Spain and Slovakia^{2,6-8}. However, due to geological similarities among different countries, Sb occurrence and its adverse effects can be expected in many other countries around the world where the problem has not been described so far. In addition, the increasing use of products containing Sb inevitably leads to the release of Sb into the environment, for example, the use of Sb as flame retardant in plastic, batteries

and electronic devices, which are landfiling causing the leaching of Sb to soils and water^{9,10}. Moreover, since its consideration as Critical Raw Material in 2010, special interest has emerged related to secondary sources of Sb and valorisation method for recovery and reuse Sb from solid and wastewater.

To reach this goal, it is necessary first, remove Sb from polluted water and then recover it for reuse. For these reasons, this PhD thesis will be focused on the first step of this “big” goal, that is to remove Sb from wastewater.

2. ANTIMONY CHEMISTRY

Sb is a unique trace element which main chemical characteristics are summarised in Table 3.1

Table 3.1 Properties of the element antimony relevant to the understanding of its solution chemistry (modified from Filella et al.¹¹)

Property (unit)	Value
<i>General</i>	
Atomic number	51
Periodic Table Group	15
Periodic Table Block	p-block
<i>Electronic configuration</i>	
Ground state electron configuration	[Kr]. 4d ¹⁰ .5s ² .5p ³
Shell structure	2.8.18.18.5
<i>Atomic mass</i>	121.760
<i>Natural occurring isotopes</i>	¹²¹ Sb (57.21%) ¹²³ Sb (42.79%)

Antimony shares many similar physiological and chemical properties with arsenic (which has been studying deeper than Sb); both have a strong affinity for sulfur than oxygen (chalcophile). However, the coordination of Sb(V) with oxygen differs greatly from that of As(V). In contrast to As(V) which is smaller and thus tetrahedrally coordinated, Sb(V) coordinates octahedrally with oxygen.

Table 3.2 lists the classes and individual Sb compounds found in environmental and biological systems. As it is observed, antimony exists in four oxidation states (-3,0,+3,+5) but is mainly found in two oxidation states (+3 and +5) in environmental, biological and geochemical samples¹². Inorganic species predominate over organic species in most environmental systems.

Table 3.2. Common Sb chemical species found in natural system¹³

	Name	Formula
<i>Minerals</i>	Stibinite	Sb ₂ S ₃
	Valentinite	Sb ₂ O ₃ (orthorhombic)
	Senarmonrite	Sb ₂ O ₃ (cubic)
	Cervantite	Sb ₂ O ₄
<i>Aqueous species (+5 oxidation state)</i>	Antimonic acid	Sb(OH) ₅
	Antimonate	Sb(OH) ₆ ⁻ (or SbO ₃ ⁻)
<i>Aqueous species (+3 oxidation state)</i>	Antimonous acid	Sb(OH) ₃ (or HSbO ₂)
	Antimonite	Sb(OH) ₂ ⁺ Sb(OH) ₄ ⁻
	Sulfidic complexes	H ₂ Sb ₂ S ₄ HSb ₂ S ₄ ⁻ Sb ₂ S ₄ ²⁻
<i>Gases</i>	Stibine	SbH ₃
	Trimethylstibine	Sb(CH ₃) ₃
<i>Other methylated species</i>	Methylstibonic acid (MSA)	(CH ₃)SbO(OH) ₂
	Dimethylstibonic acid (DMSA)	(CH ₃) ₂ Sb(O)OH
	Trimethylstiboxide	(CH ₃) ₃ Sb

Focussing on aquatic systems, chemical equilibrium of Sb(III) and Sb(V) species is schematically presented in Figure 3.1, according to solution pH. Both Sb(III) and Sb(V) ions hydrolyse easily in aqueous solution, thus making it difficult to keep antimony ions stable in solution except in highly acidic media. Among Sb(V) species, antimonic acid (Sb(OH)₅) cannot be isolated as a pure phase; it is a relatively strong acid that condenses to form polymer as the pH increases¹¹. According to thermodynamic equilibrium calculations (Figure 3.1b), the antimonate ion Sb(OH)₆⁻ is the predominant species in aqueous solutions at pH values above 2.7¹⁴. Trivalent Sb(III) predominates as the neutral antimonite Sb(OH)₃ (Figure 3.1a) between pH 1.4 and 11.8. Accordingly, significant formation of Sb(OH)₂⁺ only occurs at very low pH values and formation of Sb(OH)₄⁻ only at very high pH values⁵. Also, the possible formation of polymerised species (Sb₆O₁₀²⁻ and Sb₄O₇²⁻) has been suggested in solutions containing 10⁻¹ – 10⁻² mol/L antimony (8.3-16-1 mol/L NaOH), at far from environmentally significant concentration levels^{11,14}.

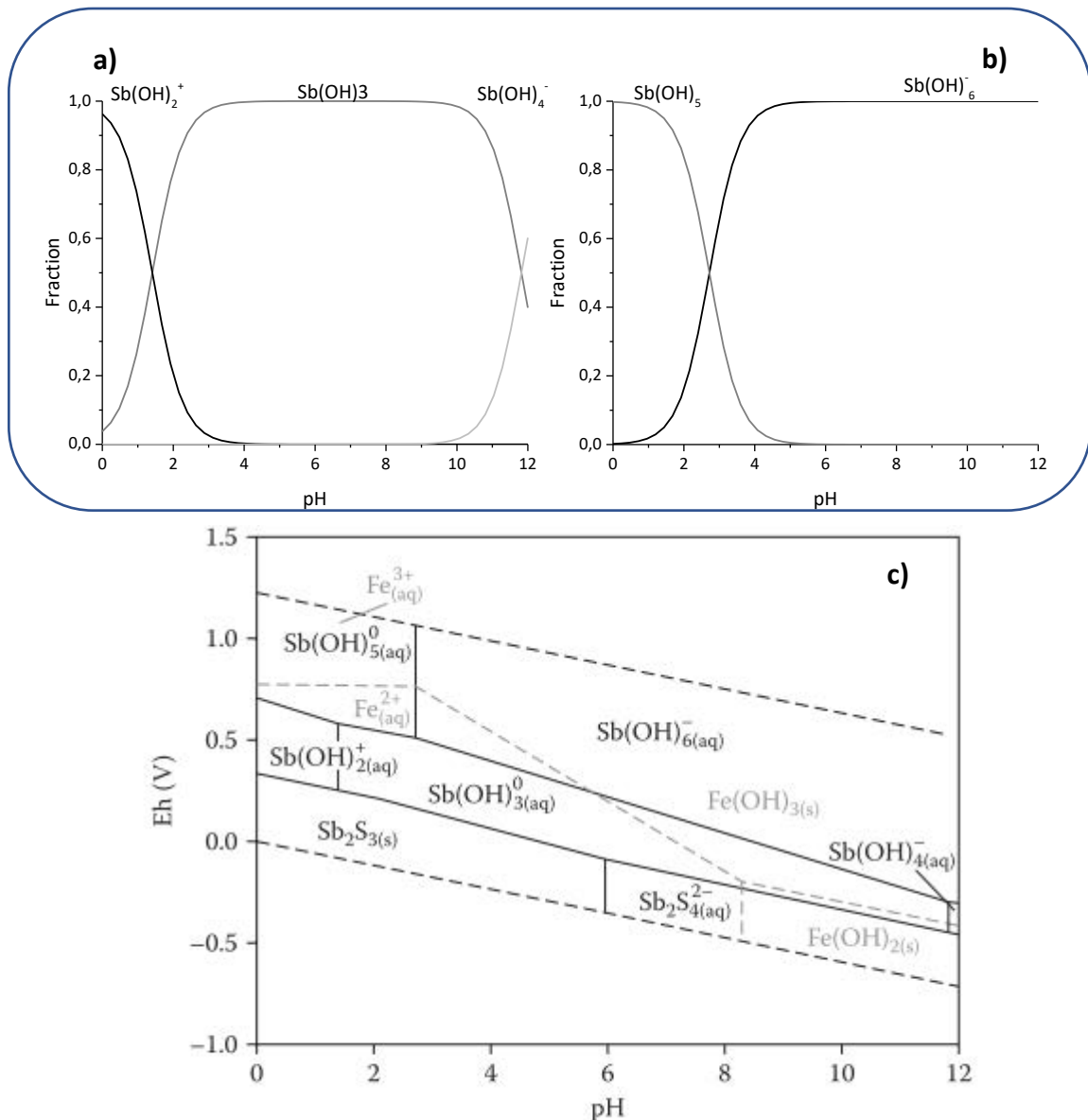


Figure 3.1. a) Speciation Sb diagram in aqueous solution as a function of pH, 25°C using HYDRA and MEDUSA software¹⁵; a) Sb(III) diagram; b) Sb(V) diagram. c) Eh(V)-pH diagram for aqueous Sb species (+3 and +5) in the Sb-S-H₂O system ($[\text{Sb}_{\text{tot}}] = 0.01 \mu\text{M}$ and $[\text{S}_{\text{tot}}] = 10\text{mM}$). Areas of predominance of Fe species are indicated by grey dashed lines.⁵

2.1. Sb redox chemistry

Since the solubility, mobility, bioavailability, and toxicity of Sb depend on its oxidation state, it is essential to understand the redox chemistry of Sb. The Eh(V)-pH (redox potential-pH) diagram illustrates the redox behaviour of antimony (Figure 3.1c). According to this diagram, antimony is presented as soluble Sb(OH)_6^- in oxic system and as soluble Sb(OH)_3 in anoxic ones at natural pH values. Under reducing conditions, and in the presence of sulfur, stibnite, $\text{Sb}_2\text{S}_3(\text{s})$ is formed at low to intermediate pH values. At higher pH values, the SbS_2^- species replaces stibnite¹¹. For very dilute systems, such as

the one depicted in Figure 3.1c, the dominant species are said to be independent of antimony concentrations¹⁶. However, where more concentrated solutions are concerned, Sb(V) may form polynuclear species under acidic conditions ($\text{pH} < 7$)¹⁶. Actually, several sources have reported the presence of both Sb(III) and Sb(V) in both oxic and anoxic waters, which contradicts the calculated thermodynamic data^{16,17}, due to biological process or slow redox reaction.

Concerning slow redox reactions, it is well known that interconversion of different redox species under changing redox conditions does not necessarily occur instantaneously. This slow conversion is often the reason why no thermodynamic equilibrium is observed between ionic species of different oxidation states. According to Latimer et al.¹⁸, the Sb(V)/Sb(III) couple is capable of attaining rapid equilibrium in both acid and basic solutions. However, if the redox process is accompanied by hydrolysis reactions or if the acidity of the solution increases^{19,20}, the overall process can be much slower. No systematic studies exist on Sb(III) oxidation kinetics under natural water conditions. Published observations seem to indicate that, at natural antimony levels, Sb(III) is gently oxidised to Sb(V). However, the addition of organic substances such as EDTA, tartaric acid, lactic, citric, ascorbic acids²¹ to natural or synthetic solutions has been shown to have a stabilising effect on Sb(III). Solutions of Sb(III) prepared from potassium antimonyl tartrate have been reported to be stable for long periods. Not much information is available on Sb(V) reduction kinetics in anoxic media.

Microbial redox processes also can directly control the speciation, mobility and transport of Sb species in the environment. Antimony oxidising bacteria such as *Stibiobacter senarmontii*, *Pseudomonas*, *Agrobacterium tumefaciens*, among others, play a crucial role in the biogeochemical cycling of Sb, transforming toxic Sb(III) to less toxic Sb(V) species²². In contrast, some microorganism as the anaerobic metal reducer *Shewanella oneidensis* strain MR1 is capable of using Sb(V) as a terminal electron acceptor²³.

As regarding this PhD thesis, iron oxides will be used for Sb removal. Thus it is necessary to study the redox relation between Sb and iron (Fe). Redox reactions between Sb and Fe were found to be particularly complex. Iron can act as a reducing as well as an oxidising agent of Sb. In accordance with the Eh-pH diagram (Figure 3.1c), there is evidence that Fe(II) in solution reduced Sb(V) to Sb(III) in alkaline, anaerobic waters²⁴. Also, Sb(V) reduction has been observed when Fe is in the form of magnetite (Fe_3O_4) and mackinawite (FeS)²⁵ or by green rust²⁶ at acidic to alkaline pH in the absence of oxygen. On the contrary, Fe(III) (and other metals such as Mn(IV)) present in the form of (hydr)oxides oxidised Sb(III) under aerobic conditions at both alkaline and acidic pH^{27,28}. The latter reaction was assumed to be catalysed by the metal(hydr)oxides, which form intermediate products such as hydroxyl ions or Fe(IV) radicals when reacting with oxygen²⁹.

2.2. Complexation with Dissolved Organic Ligands

As it was introduced before, organic ligands can complex with Sb stabilising it in aqueous solution. Dissolved organic carbon that potentially interacts with Sb in the soil solution can be divided into:

- low molecular weight (l.m.w.) organic ligands such as citric or tartaric acid
- high molecular weight (h.m.w.) fulvic and humic acids.

In this work, we only will consider low molecular weight organic ligands because we will use them mainly as desorbing agents. Also, the Sb(III) compound used for adsorption studies is potassium antimonyl tartrate due to its good stability in solutions.

In aquatic systems, a part of total Sb was found as complexes with low-weight organic ligands in the dissolved fraction. Regarding hard-soft behaviour, Sb(III) is commonly classified as a borderline metal, which makes its interaction with a soft ligand like -SH, and a hard ligand such as -COOH, both possible¹¹. A comprehensive overview of the available thermodynamic data for Sb(III) complexes with carboxyl-, phenyl-, thiol-, and amine-bearing ligands was given by Filella et al. (2005)³⁰. Also, some studies have been done regarding the solution chemistry of Sb(III)-polyaminocarboxylic acids (CDTA, DTPA, EDTA)³¹. Although significant complexation has been observed at acidic pH values, these ligands do not prevent Sb(III) hydrolysis from occurring at pH>6 at the antimony concentrations used in these studies.

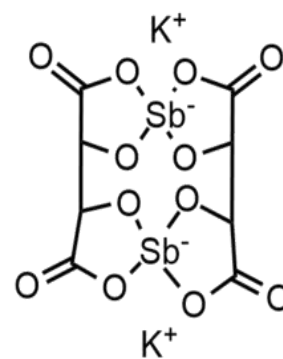


Figure 3.2 Potassium antimonyl tartrate structure

A well known Sb(III) complex, used in this PhD thesis, is potassium antimonyl tartrate or tartar emetic, $K_2[Sb_2(C_4O_6H_2)_2] \cdot 3H_2O$ (Figure 3.2). It has been known in medicine for over 300 years and is used for the treatment of schistosomiasis and leishmaniasis. This bis[tartrato(4-)]-bridged dimer anion has been extensively studied in solid phase. It exists in an essentially neutral form in compounds with both uni- and divalent-counter ions. In aqueous solutions, potassium antimonyl tartrate maintains its structure, and Sb(III) comes out as the anionic Sb(III)-tartrate complex³²⁻³⁴.

Although Sb(V) is known to form complexes with various l.m.w. organic acids, practically no thermodynamic data are available for Sb(V)³⁰. It is known that Sb(V) forms complexes with polyhydric alcohols, polyhydric phenols, and α -hydroxy acids³⁰.

Tella and Pokrovski (2008, 2009)^{34,35} determined the stability and structure of aqueous complexes formed by Sb(III) or Sb(V) with simple organic ligands over a wide pH range

using X-ray absorption fine-structure (XAFS) spectroscopy combined with potentiometric measurements. Both Sb(V) and Sb(III) showed negligible complexation with monofunctional organic ligands (acetic acid) or with dicarboxylic acids in which the carboxylic groups are nonadjacent (adipic acid). In contrast, organic ligands with adjacent carboxylic or hydroxyl groups (e.g., oxalic or citric acid) formed stable bidentate chelates with both species in a pH range from 3 to 9.

3. GLOBAL MARKET AND USES OF Sb

Figure 3.3 summarises the main Sb uses. As it can be observed, antimony is mainly used in the form of Sb_2O_3 , as flame retardant in plastics, coatings, and electronics, due to its synergetic effect with halogenated flame retardants, which minimises the amount of halogenated flame retardant required since they are recognized as global contaminants and are associated with adverse health effects in animals and humans. This application takes up most of the world's antimony production. Antimony is also used in catalysts for the production of polyethylene terephthalate (PET) polymers and as an additive in glass in the form of sodium antimonite, which acts as a decolorising agent for optical glass in cameras, photocopiers, binoculars, and fluorescent light tubes. Antimony metal is used as a hardener in lead alloys such as the lead electrodes in lead-acid (LA) batteries. The average antimony content of automotive battery alloys has declined from 7 to 1.6 % in recent years, as Ca, Al, and Sn alloys have been used as replacements. Other minor uses include paint pigments, semiconductors (including in Li-ion batteries present nowadays in most electronic devices³⁶), pesticides, ammunition and medicines (i.e. leishmaniasis treatment³⁷)^{3,38}.

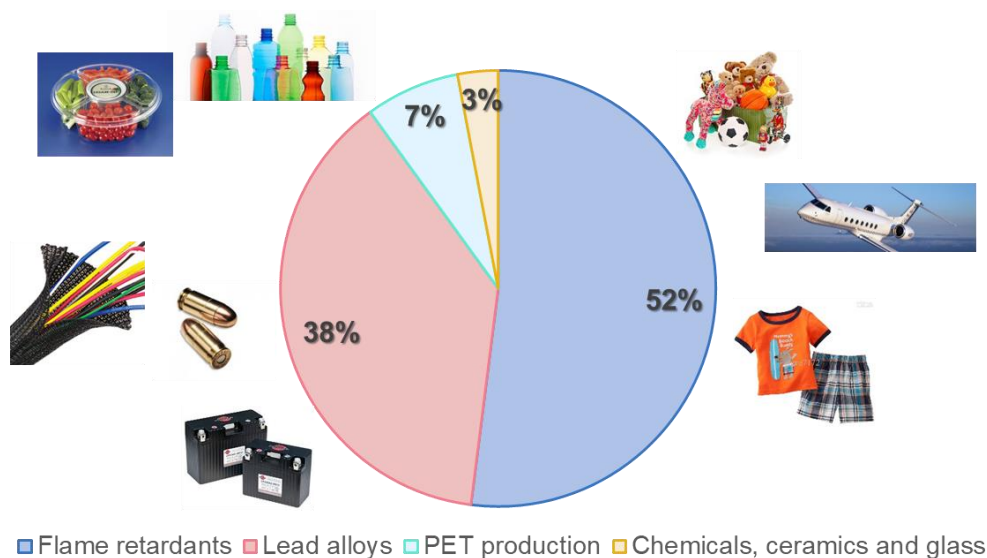


Figure 3.3. Estimated global antimony consumption (modify from Dupont et al. 2016)³

During the past 110 years, China has been the main Sb provider in the world, accounting for over 78% of the global Sb production which is predominantly associated with the major mined ore deposit located in the province of Hunan². China also holds the largest reserves. The dependence on China, combined with the strong industrial demand for antimony, has raised concerns over the supply security, especially due to its abundance in the earth’s crust is quite low what make that the current reserves (1,800,000 t) allow for only 10–11 more years of production at the current speed^{3,39}.

Figure 3.4 shows the distribution of primary and secondary production as well as the portion of illegal (non-reported) primary mining based on a 2011 consulting report³. Despite the presence of some deposits, no antimony is currently mined in Europe or the U.S.A. These observations have led the European Commission to highlight antimony as a Critical Raw Material in 2014, with an expected supply-demand gap exceeding 10 % over the period 2015–2020, which is the highest amongst all critical metals. The processing of antimony ores and the production of antimony metal is also concentrated in China due to its high smelting capacity. Most of the antimony industry in Europe and the U.S.A. is therefore dependent on the import of Chinese antimony metal and is focused on the production of high-purity products and applications.

Secondary supply, through recycling and valorisation of industrial residues, could be a solution to ensure a more secure long-term supply of antimony and could also make Europe and the U.S.A. less reliable on Chinese antimony, thus lowering geopolitical risks. Today, secondary production of antimony is mainly restricted to the recycling of antimony-containing lead alloys from lead-acid battery recycling plants. However, interesting future secondary sources could include industrial residues (e.g., mine tailings, process residues, manufacturing scrap) from the production of lead, copper, gold, and antimony.

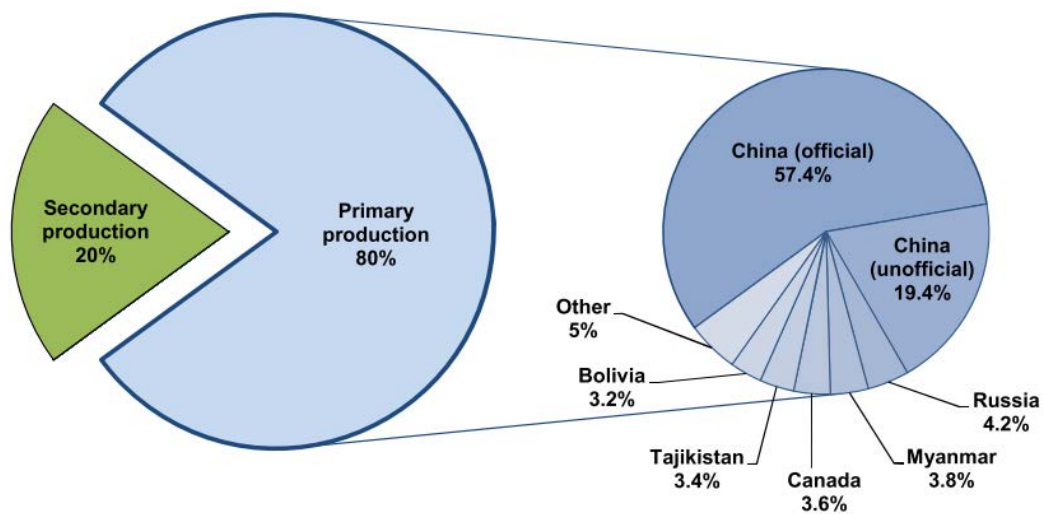


Figure 3.4. Distribution of antimony ore production in 2010 (196,484 t)³

4. ANTIMONY IN THE ENVIRONMENT

More than 200 antimony minerals are found in nature. Primary antimony minerals are typically sulfides, mainly because antimony has a higher affinity for sulfur than oxygen (chalcophile). Under ambient pH and temperature, most primary antimony minerals are fairly stable and thus are relatively insoluble. However, in oxygen-rich environments, sulfide minerals react with oxygen to produce secondary minerals. These can become unstable and result in antimony release¹⁶.

Due to increased antimony-bearing mineral mining/processing over the past few decades, there has been increased deposition of antimony into the environment⁴⁰ as is reflected in Figure 3.5. The anthropogenic sources, such as mining, military training, smelting and use of pharmaceuticals and pesticides², contribute to a significant portion of the pollution. Soil concentrations close to these sources can reach values of 15,000 mg/kg and even 80,200 mg/kg¹⁶.

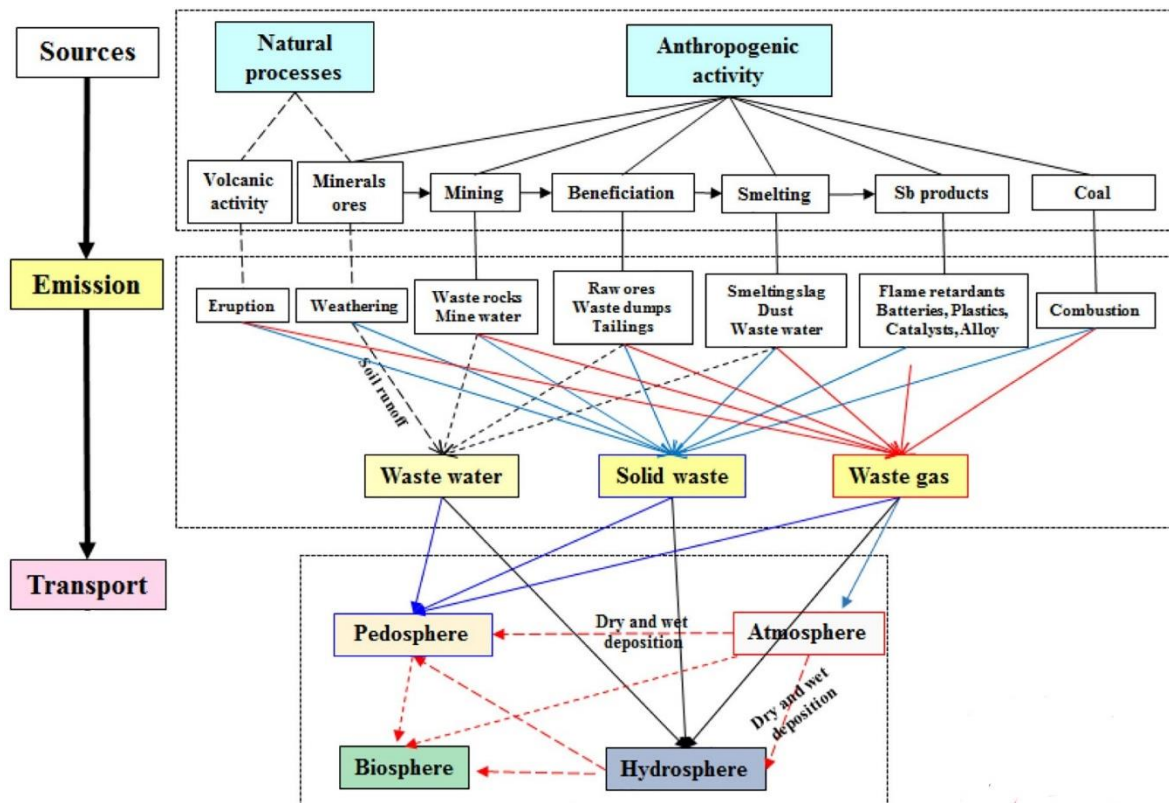


Figure 3.5 Pollution sources of Sb in the environment⁴¹.

As a result of these natural and anthropogenic sources, Sb exists in the particle form in the atmosphere in concentration from several ng/m³ to scores of ng/m³. Although Sb is not the main pollutant in the atmosphere, the continuous mining, smelting, and burning fossil fuels led to a mass increase of Sb into the atmosphere⁴⁰.

Antimony is also present in the aquatic environment as a result of rock weathering, soil runoff and anthropogenic activities. Typical concentrations of dissolved antimony in unpolluted waters are less than 1 mg/L, except for hot springs where the concentrations can sometimes exceed 500 mg/L, although the likelihood of encountering this situation is low¹⁶. However, in the proximity of anthropogenic sources, concentrations can reach up to 100 times natural levels¹².

Furthermore, Sb has been detected in plants, animals, and humans. Sb can enter humans and animal bodies through breathing, eating or body surface contact, and exists in the form of organic antimony. The usual proportion of antimony in the human body is 0.1 µg/g where it can be found in human's bone, hair and blood. It was reported that a certain amount of Sb in algae and other freshwater plants was detected, confirming that Sb could be transferred and accumulated in plants. Sb is not a necessary element for plants, but plants can absorb the dissolved Sb where exists in the organic form, being monomethyl Sb the main organic form. In the untreated terrestrial plants, the concentration of Sb was between 0.2 ng/g and 50 ng/g, but in contaminated areas, the Sb content in plants was much higher⁴⁰ (reaching Sb concentration of 400 mg/kg or higher⁴²).

5. ANTIMONY TOXICITY AND HEALTH EFFECTS

Sb is toxic to human and organisms and even suspected as a carcinogen. Besides, antimony and its compounds were considered as pollutants of priority interest by the Environmental Protection Agency of the United States and the European Union¹². The World Health Organization, China, USEPA and European Union drinking water standards are set to 10 µg/L, 5 µg/L, 6 µg/L and 5 µg/L, respectively. Antimony is on the list of hazardous substances under the Basel convention concerning the restriction of transfer of hazardous waste across borders.

In general, inorganic compounds of Sb are more toxic than its organic species and the Sb(III) compounds are predicted to be approximately 10-fold more toxic than Sb(V) oxo-anionic species¹². As it was introduced in the previous section, significant exposure to antimony occurs through both, anthropogenic and natural sources. Then, antimony and antimonide enter into human body. Human exposure routes are shown in Figure 3.6. Sb uptake occurs by breathing air, drinking water, and eating foods that contain it. Also by contact with soils, water and other substances where Sb is presented. Great concern is increasing due to human exposure to antimony for antimony migration from plastics

used in plastic bottles or food packaging^{43–46}. Occupational exposure to Sb is common in smelting and mining industry and antimony process workers⁴⁷.

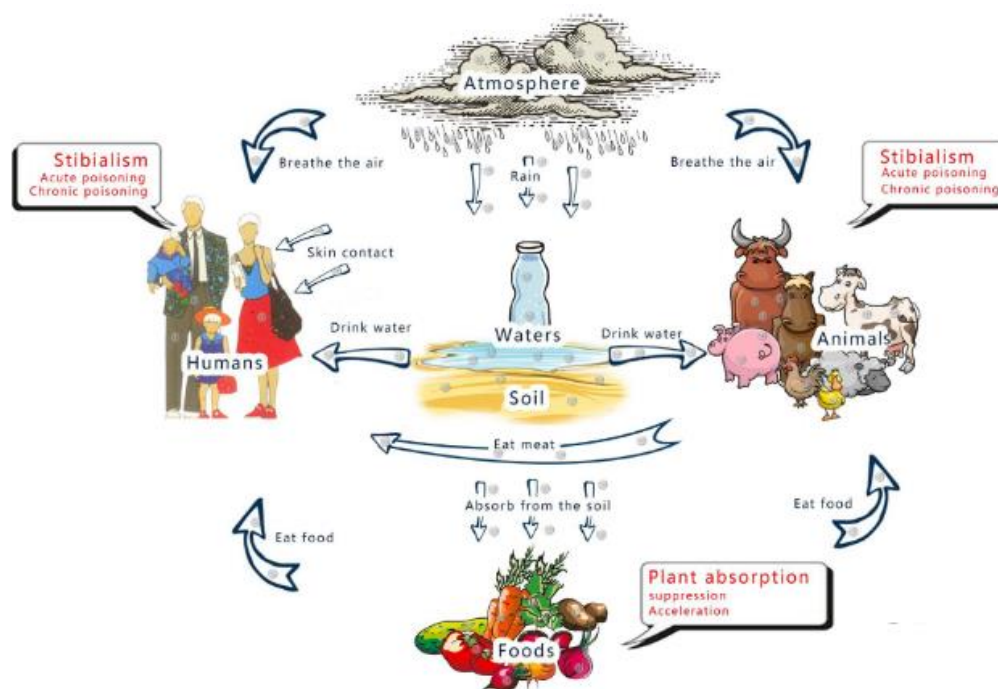


Figure 3.6. *Sb exposure media and pathways*⁴⁰

If the Sb uptake is performed by inhalation, Sb particles are deposited in lungs where pass through the lining of the lungs and enter the bloodstream. This process could take days or weeks. On the other hand, if Sb is incorporated into the body by oral uptake, it enters the blood after few hours. The amount and the form of antimony in the food or water will affect the amount of antimony entering in the blood. Once in the blood, it will be distributed throughout the body with the highest amounts in the blood, spleen, liver, and kidneys, causing Sb poisoning (Table 3.3). Antimony will leave our body in faeces and urine over several weeks⁴⁸.

Furthermore, antimonide is potentially toxic to the human body's immune system (e.g., nervous system, gene, and physique growth). It is toxic and carcinogenic to humans and organisms, leading harms to the liver, skin, lungs and even cardiovascular system. Excessive Sb can lead to acute heart diseases, which is suspected to be one of the tensions concerning sudden infant death syndrome.

Table 3.3 *Principal harmful antimony effects in human health*^{2,40,48}

Exposure	Toxic effect
<i>Acute exposure</i>	
Inhalation	Irritation of skin and eyes (antimony spots) Ocular conjunctivitis
Oral uptake	Irritation of gastrointestinal mucosa (vomiting, abdominal cramps, diarrhoea, cardiac toxicity) Muscle pain Enuresis and urine toxin and even causes liver cirrhosis, muscle necrosis, nephritis, pancreatitis
<i>Chronic exposure</i>	
Inhalation	Infection of the respiratory tract, myocardial and liver Lung function changes, bronchitis, emphysema, early tuberculosis, pleural adhesions and even pneumoconiosis
Oral uptake	Destruction of optic nerves, uveitides and retinal bleeding Headache coughing, anorexia, troubled sleep and vertigo

6. OVERVIEW OF ANTIMONY REMOVAL TECHNOLOGIES

As it was introduced in the previous sections, antimony and its compounds were considered as pollutants of priority interest by the Environmental Protection Agency of the United States and the European Union¹². Typical concentrations of antimony encountered in wastewater are dependent on anthropogenic activities and are produced by various industrial activities such as mining, lead-acid batteries production, car brake linings production, PET production, recycling plants (due to flame retardants in consumer electronics)^{49,50}. Apart from sources mentioned above, antimony can be found in wastewaters from glass production facilities (up to the 450 mg/L, depending on the technology), in streams from incineration plants (up to the 4 mg/L) and in wastewaters from anode sludge treatment (up to the 500 mg/L)⁵¹. Considering legal limits and toxic effects, the removal of this metalloid from water/ wastewater (due to anthropogenic activities or natural reasons) is mandatory.

Different technologies have been used and proposed to remove antimony from aqueous media. Each of these technologies has some advantages and disadvantages and are summarized in Table 3.4.

Taking into account the advantages and disadvantages of the removal methods presented in Table 3.4, the selection of the most appropriate one requires to consider the final desired concentration, as well as, the associated costs and the feasibility of monitoring this goal, that is to say, the selected one should have the ideal characteristics presented in Figure 3.7⁵². Concerning Sb, it is necessary also consider that the natural distribution of inorganic Sb species (Sb(III) and Sb(V)) in water influences both the treatment strategy and the removal efficiency⁵³. The anionic characteristics of Sb(V) (Sb(OH)_6^-) promote its removal, whereas the neutral characteristics of Sb(III) (Sb(OH)_3) limit its removal efficiency in conventionally applied physicochemical treatment methods at near neutral pH values⁵².

<p>Safety & Reliability</p> <ul style="list-style-type: none"> • Operation process should be safe, reliable and robust • Effective in removing both Sb(III) and Sb(V) species • Occupational health should be considered. 	<p>Operation & Maintenance</p> <ul style="list-style-type: none"> • Simple operational and maintenance requirements <ul style="list-style-type: none"> • Minimal energy requirements • Optimum pH range for the removal.
<p>Economy</p> <ul style="list-style-type: none"> • Affordable set-up, operation and maintenance 	<p>Water Quality</p> <ul style="list-style-type: none"> • Method must be effective enough • Method must perform well in the combined presence of potentially competing ions <ul style="list-style-type: none"> • Method itself must not be an unwanted contaminants source

Figure 3.7. Requirements for an ideal wastewater system

Table 3.4 Water treatment for Sb removal (Adapted from Ahmed et al. (2016) and Carolin et al. (2017)^{54,55}

Techniques	Comments	Advantages	Disadvantages	Ref
<i>Precipitation</i>	<ul style="list-style-type: none"> In combination with other techniques 	Effective, simple, inexpensive to operate	Generation of a sludge, utilisation of chemical is high	56 57
<i>Coagulation/flocculation</i>	<ul style="list-style-type: none"> Not specifically method for Sb removal Ferric coagulant is better than alum. Effective (98% Sb(V) removal using ferric as coagulant) More effective for Sb(III) 	Cost effective, Dewatering qualities	Generation of sludge, utilisation of chemical is high	52,55,58–60
<i>Membrane filtration (Nano- and Ultrafiltration)</i>	<ul style="list-style-type: none"> Efficient depends on Sb oxidation state and pH Chelating porous hollow-fibre membranes to remove Sb(III) 	High removal of heavy metals, lower space requirement	Very expensive membrane fouling, complex process	40,52,61,62
<i>Osmosis Reverse</i>	<ul style="list-style-type: none"> Better effects of removal Sb(V) than Sb(III) No significant dependence of the solution pH 	No toxic by-product is produced	Sludge production and very expensive Pressure needed. Filters get clogged, regeneration, recharge, and replacement at times is needed, thus possess high capital and operational costs	40,57,63,64
<i>Adsorption</i>	<ul style="list-style-type: none"> Widely applied technique Different sorbents 	Flexibility and simplicity of design, ease of operation, and insensitivity to toxic pollutants	Adsorbent requires regeneration	57,65
<i>Ion Exchange</i>	<ul style="list-style-type: none"> Like adsorption Chemical bonded needed XAD- 8 ion-exchange resin has a strong exchange capacity for Sb(III) and Sb(V) 	High transformation of component Good removal of a wide range of heavy metals	Removes only limited metal ions, operational cost is high Absorbent material requires regeneration and disposal problems	40
<i>Electrochemical treatment</i>	<ul style="list-style-type: none"> Electrodepositing (Concentration between 1500 and 3500 mg Sb/L⁶⁶ and 10 and 29 mg Sb/L) 96-100% Sb removal 	Rapid process but effective for particular metal ion	High energy cost and generation of by-products	55,66–68
<i>Oxidation</i>	<ul style="list-style-type: none"> Previous a coagulation, adsorption processes or membrane filtration, to enhance the treatment efficiency Oxidant reagents: chlorine, O₃, TiO₂, H₂O₂, iron, etc 	No need for electricity	Rusting occurs in the system due to the usage of oxidation	57,63,69
<i>Phytoremediation, bioremediation and biofilter</i>	<ul style="list-style-type: none"> Effective bioremediation of antimony using sulfate-reducing Different plants efficient for Sb accumulating 	Simple, economical and applicable	Slow and time-consuming Need proper waste disposal Research needed	63,70

Conventional methodologies (precipitation, oxidation, coagulation-flocculation, etc.) have their utility as a non-selective treatment for the volume reduction of the contaminant by the concentration of toxic part and the separation of the non-toxic part. However, these methodologies do not let the reuse of the waste with a beneficial aim. On the other hand, the main objective of the separation techniques is the selective metal recovery and subsequently, to produce an efficient economic process by facilitating a suitable use of recovered metals.

Therefore, separation methodologies can get the volume reduction of the generated solid wastes and, at the same time, the partial or completely recycle of the recovered fraction of the clean solution.

Regarding the shortcomings of most of these methods, it must be highlighted the high investment and maintenance costs, secondary pollution and complicated procedure involved in the treatment. Conversely, **adsorption processes** do not add undesirable by-products and have been found to be superior to other techniques for wastewater treatment regarding simplicity of design and operation, process speed and insensitivity to toxic substances⁷¹.

Nowadays, the adsorption process has become one of the leading technique in Sb removal due to its advantages (Figure 3.8). However, the advantages of adsorption are limited by the diffusion process that slows down the adsorption rates due to the diffusion barriers of adsorbent materials. Another drawback is the need to discharged the loaded adsorbent or recycled it, which implies the use of chemical reagents that contribute to contaminate the environment and reduce economic efficiency.

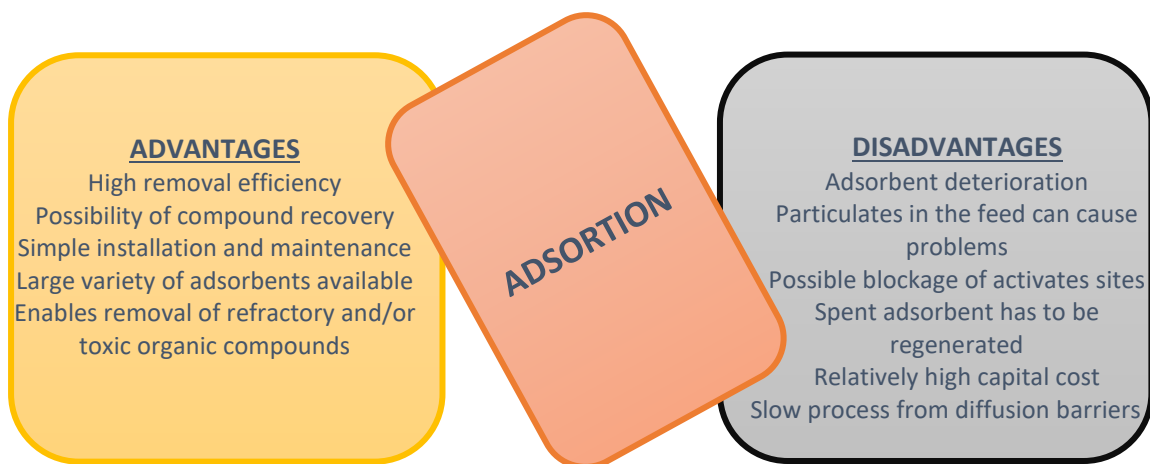


Figure 3.8 Advantages and disadvantages of adsorption as removal technique⁷²

One of the drawbacks can be solved by adsorbents regeneration by the desorption process because adsorption is a reversible technique, and the regenerated adsorbent can be reused for several purposes. Several methods are available for the regeneration of adsorbents. Based on the regeneration, the adsorption is considered an environmentally

acceptable method. Thermal regeneration, pressure swing method and electrochemical regeneration are the available methods widely used for the regeneration process. Chemical and electrochemical desorption process will be studied in this PhD thesis in Chapter 5 for Sb chemical desorption, and in Chapter 2 for electrochemical desorption (using As as example).

Diffusion problems can be solve using an appropriate adsorbent. A variety of material for Sb adsorption have been studied, including metal oxides, carbon-based materials or biosorbents as observed in Table 3.5. Among the several types of adsorbents, metal oxides have been studied extensively in the last years for their potential to remove Sb from water through adsorption. Manganese, alumina, as well as iron oxides, such as goethite, ferrihydrite, or hematite (Table 3.5) have been tested and found to remove antimony from drinking water effectively. Iron oxides are recognised as effective solid phases for the adsorption and attenuation of Sb in anthropogenic and geogenic systems. Goethite (α -FeOOH) is a common Sb adsorbent, but it is devised in adsorption capacity⁷³. On the other hand, hematite coated magnetic nanoparticles have been proved to be an excellent adsorbent for Sb⁷⁴. Also, fresh ferric hydroxide (in-situ FeOxHy) shows a good adsorptive behaviour towards Sb(III) and Sb(V)⁷⁵. Magnetic iron oxide particles have been considered as a low-cost adsorbent for Sb contamination because of the high separation ability from solution⁷⁶.

Nevertheless, most of the adsorbents present the typical weakness of adsorption process: diffusional barriers that drag out adsorption process, lack of selectivity and lack of sensibility (low adsorption at low concentrations). To mitigate their drawbacks a selective adsorbent must be used which convective properties to enhance the diffusion.

Table 3.5. *Sb adsorbents materials*

Adsorbent	Sb oxidation state	Ref.
<i>Carbon-based material & Organic materials</i>		
Graphene	Sb(V)	Dong et al. 2015 ⁷⁷
Mercapto- functionalized silica-supported organic-inorganic hybrid sorbent	Sb(III)	Fan et al. 2016 ⁷⁸
Polyamide-graphene composite	Sb(III)	Saleh et al. 2017 ⁷⁹
<i>Biosorbents</i>		
Zr (IV)-loaded saponified orange waste	Sb(III)/Sb(V)	Biswas et al. 2009 ⁸⁰
Fe(III)-loaded saponified orange waste	Sb(III)/Sb(V)	Biswas et al. 2009 ⁸⁰
Lichen (<i>Physcia Tribacia</i>)	Sb(III)	Uluzluet et al. 2015 ⁸¹
Aerobic granulates	Sb(V)	Wang et al. 2015 ⁸²
Brown Seaweeds	Sb(III)/Sb(V)	Ungureanu et al. 2017 ⁸³
Soybean stover-biochar	Sb(III)/Sb(V)	Vithanage et al. 2015 ⁸⁴
<i>Metal oxide, hydroxides and minerals</i>		
Hierarchical macro-/mesoporous amorphous alumina	Sb(V)	Duo et al. 2015 ⁸⁵
Goethite	Sb(III)/Sb(V) Sb(III)	Leuz et al. 2006 ²⁸ Xu et al. 2011 ¹¹
Fe-Mn binary oxides		Yang et al. 2018 ^{1286,87}
Iron oxyhydroxides	Sb(III)/Sb(V)	Guo et al. 2014 ⁸⁸
Hematite modified with magnetic nanoparticles	Sb(III)	Shan et al. 2014 ⁷⁴
Fe ²⁺ -doped Mg-Al layered double hydroxides NPs	Sb(V)	Kameta et al. 2015 ⁸⁹
Iron oxide-coated sand	Sb(V)	Cai et al. 2015 ⁹⁰
Carbon Nanofiber+ZrO ₂ nanoparticles	Sb(III)/Sb(V)	Luo et al. 2015 ⁹¹
Kaolinite	Sb(III)	Xi et al. 2016 ⁹²
Ferrihydrite	Sb(III)/Sb(V)	Qi et al. 2016 ⁹³
Zn-Al Sulphate Layered Double Hydroxide	Sb(V)	Ardau et al. 2016 ⁹⁴
Iron-copper binary oxides	Sb(V)	Li et al. 2016 ⁷⁶
Zr-MOF	Sb(III)/Sb(V)	He et al. 2017 ⁹⁵
La-doped magnetic biochars	Sb(V)	Wang et al. 2018 ⁹⁶
NH ₂ -Fe ₃ O ₄ -NTA core-shell magnetic nanoparticles	Sb(III)	Hao et al. 2019 ⁹⁷

7. CONCLUSIONS

Due to its scarcity, toxicity and the effects which produce on human health, Sb has been considered as Critical Raw material, and a pollutant of priority interest, thus its removal and recovery from drinking water are compulsory.

Despite the challenges mentioned above, adsorption treatment has emerged as “the best treatment” practice for Sb-wastewater due to its advantages such as low cost, simplicity, flexibility and the possibility for Sb recovery and the reuse of the adsorbent. The adsorption process can competently reduce the total effluent content of antimony while allowing for lower operating costs and easier operation.

Among the different materials used as adsorbents, iron oxides are promising materials due to their high affinity for Sb and their good properties for the adsorption process. In Chapter 4, iron oxides properties and characteristics will be discussed, especially for superparamagnetic iron oxide nanoparticles. In this concern, a critical fact is the nanoparticles handling for both separations from treated liquor and to avoid nanoparticles aggregation. To overcome both barriers, the use of special nanoparticles support has been proposed that also offers excellent properties to minimise the diffusion barriers that limits the adsorption dynamics.

8. REFERENCES

- (1) Pierart, A.; Shahid, M.; Séjalon-Delmas, N.; Dumat, C. Antimony Bioavailability: Knowledge and Research Perspectives for Sustainable Agricultures. *J. Hazard. Mater.* **2015**, *289*, 219–234.
- (2) Herath, I.; Vithanage, M.; Bundschuh, J. Antimony as a Global Dilemma: Geochemistry, Mobility, Fate and Transport. *Environ. Pollut.* **2017**, *223*, 545–559.
- (3) Dupont, D.; Arnout, S.; Jones, P. T.; Binnemans, K. Antimony Recovery from End-of-Life Products and Industrial Process Residues: A Critical Review. *J. Sustain. Metall.* **2016**, *2* (1), 79–103.
- (4) European Commission. *Study on the Review of the List of Critical Raw Materials*; 2017.
- (5) Hockmann, K.; Schulin, R. Leaching of Antimony from Contaminated Soils. In *Competitive Sorption and Transport of Heavy Metals in Soils and Geological Media*; Magdi Selim, H., Ed.; CRC Press, 2013; pp 119–147.
- (6) Pérez-Sirvent, C.; Martínez-Sánchez, M. J.; Martínez-López, S.; Bech, J.; Bolan, N. Distribution and Bioaccumulation of Arsenic and Antimony in *Dittrichia Viscosa* Growing in Mining-Affected Semiarid Soils in Southeast Spain. *J. Geochemical Explor.* **2012**, *123*, 128–135.
- (7) Murciego, A. M.; Sánchez, A. G.; González, M. A. R.; Gil, E. P.; Gordillo, C. T.; Fernández, J. C.; Triguero, T. B. Antimony Distribution and Mobility in Topsoils and Plants (*Cytisus Striatus*, *Cistus Ladanifer* and *Dittrichia Viscosa*) from Polluted Sb-Mining Areas in Extremadura (Spain). *Environ. Pollut.* **2007**, *145* (1), 15–21.

- (8) Hiller, E.; Lalinská, B.; Chovan, M.; Jurkovič, Ľ.; Klimko, T.; Jankulár, M.; Hovorič, R.; Šottník, P.; Fláková, R.; Ženišová, Z.; et al. Arsenic and Antimony Contamination of Waters, Stream Sediments and Soils in the Vicinity of Abandoned Antimony Mines in the Western Carpathians, Slovakia. *Appl. Geochemistry* **2012**, *27* (3), 598–614.
- (9) Kiddee, P.; Naidu, R.; Wong, M. H. Metals and Polybrominated Diphenyl Ethers Leaching from Electronic Waste in Simulated Landfills. *J. Hazard. Mater.* **2013**, *252–253*, 243–249.
- (10) Cornelis, G.; Van Gerven, T.; Vandecasteele, C. Antimony Leaching from Uncarbonated and Carbonated MSWI Bottom Ash. *J. Hazard. Mater.* **2006**, *137* (3), 1284–1292.
- (11) Filella, M.; Belzile, N.; Chen, Y.-W. Antimony in the Environment: A Review Focused on Natural Waters II. *Earth-Science Rev.* **2002**, *59* (1–4), 265–285.
- (12) Filella, M.; Belzile, N.; Chen, Y.-W. Antimony in the Environment: A Review Focused on Natural Waters I. *Earth-Science Rev.* **2002**, *57* (1–2), 125–176.
- (13) Wilson, S. C.; Lockwood, P. V.; Ashley, P. M.; Tighe, M. The Chemistry and Behaviour of Antimony in the Soil Environment with Comparisons to Arsenic: A Critical Review. *Environ. Pollut.* **2010**, *158* (5), 1169–1181.
- (14) Baes, C. F.; Mesmer, R. S. *The Hydrolysis of Cations*; John Wiley & Sons, 1976.
- (15) Puigdomenech, I. Medusa. Royal Institut of Technology, Stockholm 1999.
- (16) Multani, R. S.; Feldmann, T.; Demopoulos, G. P. Antimony in the Metallurgical Industry: A Review of Its Chemistry and Environmental Stabilization Options. *Hydrometallurgy* **2016**, *164*, 141–153.
- (17) Pokrovski, G. S.; Borisova, A. Y.; Roux, J.; Hazemann, J.-L.; Petdang, A.; Tella, M.; Testemale, D. Antimony Speciation in Saline Hydrothermal Fluids: A Combined X-Ray Absorption Fine Structure Spectroscopy and Solubility Study. *Geochim. Cosmochim. Acta* **2006**, *70*, 4196–4214.
- (18) Latimer, W. M. The Oxidation States of the Elements and Their Potentials in Aqueous Solutions. Prentice-Hall: New York 1938, p 352.
- (19) Sherman, D. M.; Ragnarsdottir, K. V.; Oelkers, E. H. Antimony Transport in Hydrothermal Solutions: An EXAFS Study of Antimony(V) Complexation in Alkaline Sulfide and Sulfide-Chloride Brines at Temperatures from 25°C to 300°C at P(Sat). *Chem. Geol.* **2000**, *167* (1–2), 161–167.
- (20) Han-Wen, S.; Xiao-Quan, S.; Zhe-Ming, N. Selective Separation and Differential Determination of Antimony(III) and Antimony(V) by Solvent Extraction with N-Benzoyl-N-Phenylhydroxylamine and Graphite-Furnace Atomic-Absorption Spectrometry Using a Matrix-Modification Technique. *Talanta* **1982**, *29* (7), 589–593.
- (21) Daus, B.; Wennrich, R. Investigation on Stability and Preservation of Antimonite in Iron Rich Water Samples. *Anal. Chim. Acta* **2014**, *847*, 44–48.
- (22) Li, J.; Wang, Q.; Zhang, S.; Qin, D.; Wang, G. Phylogenetic and Genome Analyses of Antimony-Oxidizing Bacteria Isolated from Antimony Mined Soil. *Int. Biodeterior. Biodegrad.* **2013**, *76*, 76–80.
- (23) Ackermann, S. The Interaction of Iron Oxides and Sulfates with Antimony , Aqueous Solutions , and Bacteria : A Mineralogical and Geochemical Study, 2015.
- (24) Leuz, A. K.; Hug, S. J.; Wehrli, B.; Johnson, C. A. Iron-Mediated Oxidation of Antimony(III) by Oxygen and Hydrogen Peroxide Compared to Arsenic(III) Oxidation. *Environ. Sci. Technol.* **2006**, *40* (8), 2565–2571.
- (25) Kirsch, R.; Scheinost, A. C.; Rossberg, A.; Banerjee, D.; Charlet, L. Reduction of Antimony by Nano-Particulate Magnetite and Mackinawite. *Mineral. Mag.* **2008**, *72* (February), 185–189.
- (26) Mitsunobu, S.; Takahashi, Y.; Sakai, Y. Abiotic Reduction of Antimony(V) by Green Rust (Fe₄(II)Fe₂(III)(OH)₁₂SO₄ · 3H₂O). *Chemosphere* **2008**, *70* (5), 942–947.

- (27) Belzile, N.; Chen, Y. W.; Wang, Z. Oxidation of Antimony (III) by Amorphous Iron and Manganese Oxyhydroxides. *Chem. Geol.* **2001**, *174* (4), 379–387.
- (28) Leuz, A. K.; Mönch, H.; Johnson, C. A. Sorption of Sb(III) and Sb(V) to Goethite: Influence on Sb(III) Oxidation and Mobilization. *Environ. Sci. Technol.* **2006**, *40* (23), 7277–7282.
- (29) Kong, L.; Hu, X.; He, M. Mechanisms of Sb(III) Oxidation by Pyrite-Induced Hydroxyl Radicals and Hydrogen Peroxide. *Environ. Sci. Technol.* **2015**, *49* (6), 3499–3505.
- (30) Filella, M.; May, P. M. Critical Appraisal of Available Thermodynamic Data for the Complexation of Antimony(III) and Antimony(V) by Low Molecular Mass Organic Ligands. *J. Environ. Monit.* **2005**, *7* (12), 1226–1237.
- (31) Wu, D.; Pichler, T. Preservation of Co-Occurring As, Sb and Se Species in Water Samples with EDTA and Acidification. *Geochemistry Explor. Environ. Anal.* **2016**, *16* (2), 117–125.
- (32) Nishad, P. A.; Bhaskarapillai, A.; Velmurugan, S. Towards Finding an Efficient Sorbent for Antimony: Comparative Investigations on Antimony Removal Properties of Potential Antimony Sorbents. *Int. J. Environ. Sci. Technol.* **2017**, *14* (4), 777–784.
- (33) Filella, M.; Williams, P. A. Antimony Biomethylation in Culture Media Revisited in the Light of Solubility and Chemical Speciation Considerations. *Environ. Toxicol.* **2010**, *25* (5), 429–532.
- (34) Tella, M.; Pokrovski, G. S. Antimony(III) Complexing with O-Bearing Organic Ligands in Aqueous Solution: An X-Ray Absorption Fine Structure Spectroscopy and Solubility Study. *Geochim. Cosmochim. Acta* **2009**, *73* (2), 268–290.
- (35) Tella, M.; Pokrovski, G. S. Stability and Structure of Pentavalent Antimony Complexes with Aqueous Organic Ligands. *Chem. Geol.* **2012**, *292–293*, 57–68.
- (36) Goriparti, S.; Miele, E.; De Angelis, F.; Di Fabrizio, E.; Proietti Zaccaria, R.; Capiglia, C. Review on Recent Progress of Nanostructured Anode Materials for Li-Ion Batteries. *J. Power Sources* **2014**, *257*, 421–443.
- (37) Tiekink, E. R. T. Antimony and Bismuth Compounds in Oncology. *Crit. Rev. Oncol. Hematol.* **2002**, *42* (3), 217–224.
- (38) Anderson, C. G. Hydrometallurgically Treating Antimony-Bearing Industrial Wastes. *JOM* **2001**, *53* (1), 18–20.
- (39) U.S. Geological Survey. <https://minerals.usgs.gov/minerals/pubs/commodity/antimony/>.
- (40) Li, J.; Zheng, B. H.; He, Y.; Zhou, Y.; Chen, X.; Ruan, S.; Yang, Y.; Dai, C.; Tang, L. Antimony Contamination, Consequences and Removal Techniques: A Review. *Ecotoxicol. Environ. Saf.* **2018**, *156* (November 2017), 125–134.
- (41) He, M.; Wang, N.; Long, X.; Zhang, C.; Ma, C.; Zhong, Q.; Wang, A.; Wang, Y.; Pervaiz, A.; Shan, J. Antimony Speciation in the Environment: Recent Advances in Understanding the Biogeochemical Processes and Ecological Effects. *J. Environ. Sci. (China)* **2018**, 1–26.
- (42) Feng, R.; Wei, C.; Tu, S.; Ding, Y.; Wang, R.; Guo, J. The Uptake and Detoxification of Antimony by Plants: A Review. *Environ. Exp. Bot.* **2013**, *96*, 28–34.
- (43) Hansen, C.; Tsirigotaki, A.; Bak, S. A.; Pergantis, S. a; Stürup, S.; Gammelgaard, B.; Hansen, H. R. Elevated Antimony Concentrations in Commercial Juices. *J. Environ. Monit.* **2010**, *12* (4), 822–824.
- (44) Shotyk, W.; Krachler, M. Contamination of Bottled Waters with Antimony Leaching from Polyethylene Terephthalate (PET) Increases upon Storage. *Environ. Sci. Technol.* **2007**, *41* (5), 1560–1563.
- (45) Mihucz, V. G.; Záray, G. Occurrence of Antimony and Phthalate Esters in Polyethylene Terephthalate Bottled Drinking Water. *Appl. Spectrosc. Rev.* **2016**, *51* (3), 183–209.

- (46) Whitt, M.; Brown, W.; Danes, J. E.; Vorst, K. L. Migration of Heavy Metals from Recycled Polyethylene Terephthalate during Storage and Microwave Heating. *J. Plast. Film Sheeting* **2016**, *32* (2), 189–207.
- (47) McCallum, R. I. Occupational Exposure to Antimony Compounds. *J. Environ. Monit.* **2005**, *7* (12), 1245–1250.
- (48) ATSDR. *Toxicological Profile For Antimony and Compounds*; 2017.
- (49) Velzen, D. van; Langenkamp, H.; Herb, G. Antimony, Its Sources, Applications and Flow Paths into Urban and Industrial Waste: A Review. *Waste Manag. Res.* **1998**, *16* (1), 32–40.
- (50) Hargreaves, A. J.; Vale, P.; Whelan, J.; Constantino, C.; Dotro, G.; Cartmell, E. Mercury and Antimony in Wastewater: Fate and Treatment. *Water, Air, Soil Pollutionr Soil* **2016**, *227*, 89–106.
- (51) Avdić, N.; Müller-czygan, G. Treatment of Antimony-Rich Waste Streams. *Bull. teh Chem. Technol. Bosnia Herzegovina* **2013**, *40*, 47–49.
- (52) Du, X.; Qu, F.; Liang, H.; Li, K.; Yu, H.; Bai, L.; Li, G. Removal of Antimony (III) from Polluted Surface Water Using a Hybrid Coagulation-Flocculation-Ultrafiltration (CF-UF) Process. *Chem. Eng. J.* **2014**, *254*, 293–301.
- (53) Zheng, J. A.; Ohata, M.; Furuta, N. Antimony Speciation in Environmental Samples by Using High-Performance Liquid Chromatography Coupled to Inductively Coupled Plasma Mass Spectrometry. *Anal. Sci.* **2000**, *16* (1), 75–80.
- (54) Carolin, C. F.; Kumar, P. S.; Saravanan, A.; Joshiba, G. J.; Naushad, M. Efficient Techniques for the Removal of Toxic Heavy Metals from Aquatic Environment: A Review. *J. Environ. Chem. Eng.* **2017**, *5* (3), 2782–2799.
- (55) Ahmed, M. J. K.; Ahmaruzzaman, M. A Review on Potential Usage of Industrial Waste Materials for Binding Heavy Metal Ions from Aqueous Solutions. *J. Water Process Eng.* **2016**, *10*, 39–47.
- (56) Fu, F.; Wang, Q. Removal of Heavy Metal Ions from Wastewaters: A Review. *J. Environ. Manage.* **2011**, *92* (3), 407–418. <https://doi.org/10.1016/j.jenvman.2010.11.011>.
- (57) Ungureanu, G.; Santos, S.; Boaventura, R.; Botelho, C. Arsenic and Antimony in Water and Wastewater: Overview of Removal Techniques with Special Reference to Latest Advances in Adsorption. *J. Environ. Manage.* **2015**, *151*, 326–342.
- (58) Kang, M.; Kamei, T.; Magara, Y. Comparing Polyaluminum Chloride and Ferric Chloride for Antimony Removal. *Water Res.* **2003**, *37* (17), 4171–4179.
- (59) Guo, X.; Wu, Z.; He, M. Removal of Antimony(V) and Antimony(III) from Drinking Water by Coagulation-Flocculation-Sedimentation (CFS). *Water Res.* **2009**, *43* (17), 4327–4335.
- (60) Wu, Z.; He, M.; Guo, X.; Zhou, R. Removal of Antimony (III) and Antimony (V) from Drinking Water by Ferric Chloride Coagulation: Competing Ion Effect and the Mechanism Analysis. *Sep. Purif. Technol.* **2010**, *76* (2), 184–190.
- (61) Ma, B.; Wang, X.; Liu, R.; Qi, Z.; Jefferson, W. A.; Lan, H.; Liu, H.; Qu, J. Enhanced Antimony(V) Removal Using Synergistic Effects of Fe Hydrolytic Floccs and Ultrafiltration Membrane with Sludge Discharge Evaluation. *Water Res.* **2017**, *121*.
- (62) Liu, L.; Zhao, M.; Shi, Y.; Zhang, G.; Liu, Y. Removal of Antimony from Raw Water by Complexation-Ultrafiltration. *Chinese J. Environ. Eng.* **2017**, *11* (3).
- (63) Mubarak, H.; Chai, L.-Y.; Mirza, N.; Yang, Z.-H.; Pervez, A.; Tariq, M.; Shaheen, S.; Mahmood, Q. Antimony (Sb) – Pollution and Removal Techniques – Critical Assessment of Technologies. *Toxicol. Environ. Chem.* **2015**, *97* (10), 1296–1318.
- (64) Kang, M.; Kawasaki, M.; Tamada, S.; Kamei, T.; Magara, Y. Effect of PH on the Removal of Arsenic and Antimony Using Reverse Osmosis Membranes. *Desalination* **2000**, *131* (1–3), 293–298.

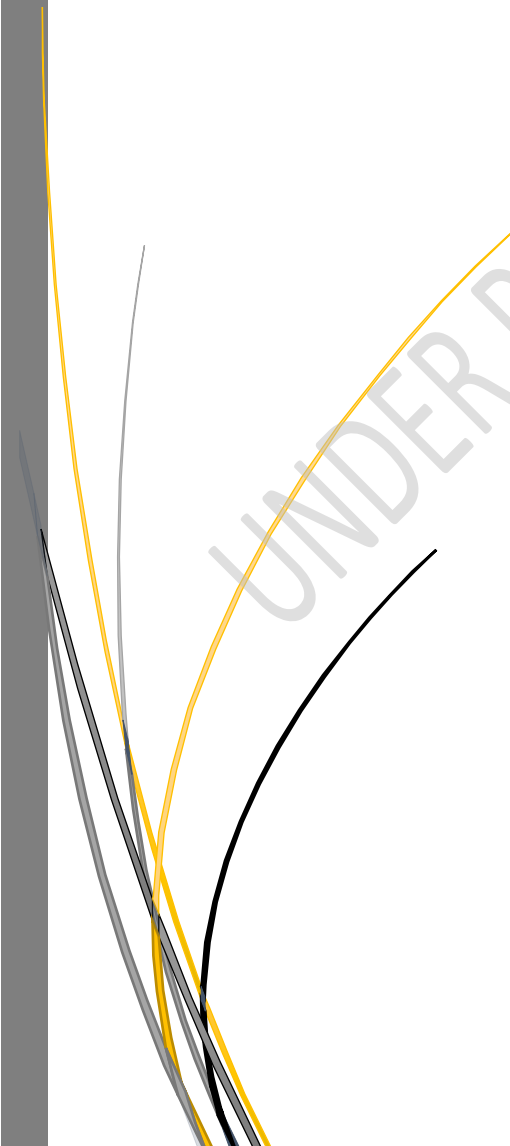
- (65) Ruihua, L.; Lin, Z.; Tao, T.; Bo, L. Phosphorus Removal Performance of Acid Mine Drainage from Wastewater. *J. Hazard. Mater.* **2011**, *190* (1–3), 669–676.
- (66) Koparal, S. S.; Özgür, R.; Öğütveren, Ü. B.; Bergmann, H. Antimony Removal from Model Acid Solutions by Electrodeposition. *Sep. Purif. Technol.* **2004**, *37* (2), 107–116.
- (67) Bergmann, M. E. H.; Koparal, A. S. Electrochemical Antimony Removal from Accumulator Acid: Results from Removal Trials in Laboratory Cells. *J. Hazard. Mater.* **2011**, *196*, 59–65.
- (68) Song, P.; Yang, Z.; Zeng, G.; Yang, X.; Xu, H.; Huang, J.; Wang, L. Optimization, Kinetics, Isotherms, and Thermodynamics Studies of Antimony Removal in Electrocoagulation Process. *Water. Air. Soil Pollut.* **2015**, *226* (11).
- (69) Patil, D. S.; Chavan, S. M.; Oubagaranadin, J. U. K. A Review of Technologies for Manganese Removal from Wastewaters. *J. Environ. Chem. Eng.* **2016**, *4* (1), 468–487.
- (70) Wang, H.; Chen, F.; Mu, S.; Zhang, D.; Pan, X.; Lee, D. J.; Chang, J. S. Removal of Antimony (Sb(V)) from Sb Mine Drainage: Biological Sulfate Reduction and Sulfide Oxidation-Precipitation. *Bioresour. Technol.* **2013**, *146*, 799–802.
- (71) *Emerging Compounds Removal from Wastewater. Natural and Solar Based Treatments*; Lofrano, G., Ed.; Springer, 2012.
- (72) Inglezakis, V. J.; Pouloupoulos, S. G. 2.1 Adsorption, Ion Exchange, and Catalysis. In *Adsorption, Ion Exchange and Catalysis*; Elsevier, 2006; pp 31–56.
- (73) Xi, J.; He, M.; Wang, K.; Zhang, G. Adsorption of Antimony(III) on Goethite in the Presence of Competitive Anions. *J. Geochemical Explor.* **2013**, *132*, 201–208.
- (74) Shan, C.; Ma, Z.; Tong, M. Efficient Removal of Trace Antimony(III) through Adsorption by Hematite Modified Magnetic Nanoparticles. *J. Hazard. Mater.* **2014**, *268*, 229–236.
- (75) He, Z.; Liu, R.; Liu, H.; Qu, J. Adsorption of Sb(III) and Sb(V) on Freshly Prepared Ferric Hydroxide (FeOxHy). *Environ. Eng. Sci.* **2015**, *32* (2), 95–102.
- (76) Li, Y.; Hu, X.; Ren, B.; Yue, J.; Yang, W. Preparation of Iron-Copper Binary Oxide and Its Effective Removal on Antimony(V) from Water. *Desalin. Water Treat.* **2016**, *57* (55), 26461–26471.
- (77) Dong, S.; Dou, X.; Mohan, D.; Pittman, C. U.; Luo, J. Synthesis of Graphene Oxide/Schwertmannite Nanocomposites and Their Application in Sb(V) Adsorption from Water. *Chem. Eng. J.* **2015**, *270*, 205–214.
- (78) Fan, H.-T.; Sun, W.; Jiang, B.; Wang, Q.-J.; Li, D.-W.; Huang, C.-C.; Wang, K.-J.; Zhang, Z.-G.; Li, W.-X. Adsorption of Antimony(III) from Aqueous Solution by Mercapto-Functionalized Silica-Supported Organic-Inorganic Hybrid Sorbent: Mechanism Insights. *Chem. Eng. J.* **2016**, *286*, 128–138.
- (79) Saleh, T. A.; Sari, A.; Tuzen, M. Effective Adsorption of Antimony(III) from Aqueous Solutions by Polyamide-Graphene Composite as a Novel Adsorbent. *Chem. Eng. J.* **2017**, *307*, 230–238.
- (80) Biswas, B. K.; Inoue, J.; Kawakita, H.; Ohto, K.; Inoue, K. Effective Removal and Recovery of Antimony Using Metal-Loaded Saponified Orange Waste. *J. Hazard. Mater.* **2009**, *172* (2–3), 721–728.
- (81) Uluozlu, O. D.; Sari, A.; Tuzen, M. Biosorption of Antimony from Aqueous Solution by Lichen (*Physcia Tribacia*) Biomass. *Chem. Eng. J.* **2010**, *163* (3), 382–388.
- (82) Wang, L.; Wang, J.; Zhang, R.; Liu, X.; Song, G.; Chen, X.; Wang, Y.; Kong, J. Highly Efficient As(V)/Sb(V) Removal by Magnetic Sludge Composite: Synthesis, Characterization, Equilibrium, and Mechanism Studies. *RSC Adv.* **2016**, *6*, 42876–42884.

- (83) Ungureanu, G.; Santos, S. C. R.; Volf, I.; Boaventura, R. A. R.; Botelho, C. M. S. Biosorption of Antimony Oxyanions by Brown Seaweeds: Batch and Column Studies. *J. Environ. Chem. Eng.* **2017**, *5* (4), 3463–3471.
- (84) Vithanage, M.; Rajapaksha, A. U.; Ahmad, M.; Uchimiya, M.; Dou, X.; Alessi, D. S.; Ok, Y. S. Mechanisms of Antimony Adsorption onto Soybean Stover-Derived Biochar in Aqueous Solutions. *J. Environ. Manage.* **2015**, *151*, 443–449.
- (85) Dou, X.; Mohan, D.; Zhao, X.; Pittman, C. U. Antimonate Removal from Water Using Hierarchical Macro-/Mesoporous Amorphous Alumina. *Chem. Eng. J.* **2015**, *264*, 617–624.
- (86) Xu, W.; Wang, H.; Liu, R.; Zhao, X.; Qu, J. The Mechanism of Antimony(III) Removal and Its Reactions on the Surfaces of Fe-Mn Binary Oxide. *J. Colloid Interface Sci.* **2011**, *363*, 320–326.
- (87) Yang, K.; Zhou, J.; Lou, Z.; Zhou, X.; Liu, Y.; Li, Y.; Ali Baig, S.; Xu, X. Removal of Sb(V) from Aqueous Solutions Using Fe-Mn Binary Oxides: The Influence of Iron Oxides Forms and the Role of Manganese Oxides. *Chem. Eng. J.* **2018**, *354* (August), 577–588.
- (88) Guo, X.; Wu, Z.; He, M.; Meng, X.; Jin, X.; Qiu, N.; Zhang, J. Adsorption of Antimony onto Iron Oxyhydroxides: Adsorption Behavior and Surface Structure. *J. Hazard. Mater.* **2014**.
- (89) Kameda, T.; Kondo, E.; Yoshioka, T. Equilibrium and Kinetics Studies on As(V) and Sb(V) Removal by Fe²⁺-Doped Mg-Al Layered Double Hydroxides. *J. Environ. Manage.* **2015**, *151*, 303–309.
- (90) Cai, Y.; Li, L.; Zhang, H. Kinetic Modeling of PH-Dependent Antimony (V) Sorption and Transport in Iron Oxide-Coated Sand. *Chemosphere* **2015**, *138*, 758–764.
- (91) Luo, J.; Luo, X.; Crittenden, J.; Qu, J.; Bai, Y.; Peng, Y.; Li, J. Removal of Antimonite (Sb(III)) and Antimonate (Sb(V)) from Aqueous Solution Using Carbon Nanofibers That Are Decorated with Zirconium Oxide (ZrO₂). *Environ. Sci. Technol.* **2015**, *49* (18), 11115–11124.
- (92) Xi, J.; He, M.; Kong, L. Adsorption of Antimony on Kaolinite as a Function of Time, PH, HA and Competitive Anions. *Environ. Earth Sci.* **2016**, *75* (2), 1–7.
- (93) Qi, P.; Pichler, T. Sequential and Simultaneous Adsorption of Sb(III) and Sb(V) on Ferrihydrite: Implications for Oxidation and Competition. *Chemosphere* **2016**, *145*, 55–60.
- (94) Arda, C.; Frau, F.; Lattanzi, P. Antimony Removal from Aqueous Solutions by the Use of Zn-Al Sulphate Layered Double Hydroxide. *Water, Air, Soil Pollut.* **2016**, *227*, 334.
- (95) He, X.; Min, X.; Luo, X. Efficient Removal of Antimony (III, V) from Contaminated Water by Amino Modification of a Zirconium Metal-Organic Framework with Mechanism Study. *J. Chem. Eng. Data* **2017**, *62* (4), 1519–1529.
- (96) Wang, L.; Wang, J.; Wang, Z.; He, C.; Lyu, W.; Yan, W.; Yang, L. Enhanced Antimonate (Sb(V)) Removal from Aqueous Solution by La-Doped Magnetic Biochars. *Chem. Eng. J.* **2018**, *354* (August), 623–632.
- (97) Hao, H.; Liu, G.; Wang, Y.; Shi, B.; Han, K.; Zhuang, Y.; Kong, Y. Simultaneous Cationic Cu (II)–anionic Sb (III) Removal by NH₂-Fe₃O₄-NTA Core-Shell Magnetic Nanoparticle Sorbents Synthesized via a Facile One-Pot Approach. *J. Hazard. Mater.* **2019**, *362* (August 2018), 246–257.

CHAPTER 4

OPTIMIZATION AND CHARACTERISATION OF SUPERPARAMAGNETIC IRON OXIDE (SPION) ADSORBENT FOR ANTIMONY REMOVAL

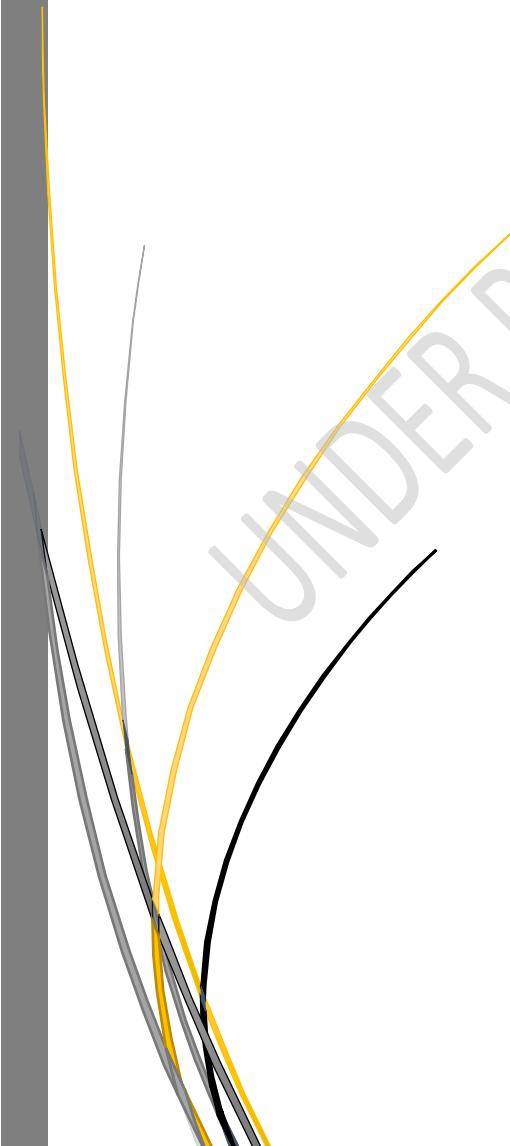
UNDER PATENT PROTECTION



CHAPTER 5

CHARACTERISATION OF Sb(III) AND Sb(V) SORPTION PROCESS ON THE SPONGE AND SPONGE+SPION SYSTEM

UNDER PATENT PROTECTION



CHAPTER 6

SPECTROSCOPIC STUDY OF THE ADSORPTION OF Sb(III) AND Sb(V) ON SPONGE-SPION-DIRECT SYSTEM

1. INTRODUCTION.....	195
1.1. Adsorption mechanism.....	196
1.2. Metal oxide surface in water	197
1.3. Adsorption on inorganic species by metal oxide materials	198
1.4. Spectroscopy method for sorption mechanism determination.....	200
2. OBJECTIVES	202
3. MATERIALS AND METHOD.....	203
4. RESULTS	206
4.1. pH influence.....	206
4.2. FTIR analysis.....	210
4.3. XAS measurements.....	214
4.4. Sorption mechanism.....	218
5. CONCLUSIONS.....	222
6. REFERENCES.....	223

1. INTRODUCTION

As it was introduced in Chapter 3, the adsorbents used to study the Sb adsorption process in this PhD thesis are Metalzorb® sponge, from this point as sponge, and also Sponge with SPION prepared by direct system (previously detailed), henceforth sponge+SPION.

As mentioned, Metalzorb sponge is an open-celled cellulose sponge which contains a water-insoluble polyamide chelating polymer formed by the reaction of polyethyleneimine and nitrilotriacetic acid. It is a heterogeneous material comprised of a range of functional groups, which have been confirmed in Chapter 4, section 4.1.4, by FTIR analysis. Its structure is shown in Figure 6.1¹. Observing the structure, the main chemical groups that may interact with Sb and facilitate its adsorption are amino and amide groups. After the acid pretreatment, these groups will have a positive charge and acidic proton², providing the pH of contact solution to be lower than 2.5 (pH_{zc} of sponge, Chapter 4, section 4.1.7). The existence of these groups will facilitate Sb adsorption.

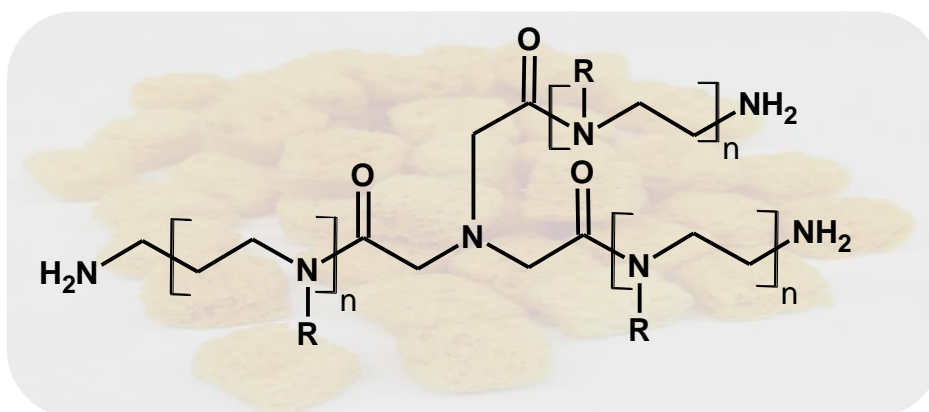


Figure 5.1 Metalzorb® sponge structure¹

After the synthesis of SPION on the sponge surface, besides the groups present in the sponge -FeOH groups corresponding to the SPION are also present and involved in the sorption process. The complex chemical composition of sponge+SPION system provides a complex surface chemistry, which is studied in this Chapter. The different functional groups in these materials will be able to interact with Sb chemical species in different ways to accomplish the adsorption.

1.1. Adsorption mechanism

As it is defined in Chapter 5, adsorption is the attachment of an ion in solution to a solid surface in contact with this solution. In general, the adsorption can be classified according to the type of interaction that occurs between the adsorbent and adsorbate. If there is an electron transfer or ion-pair formation between the adsorbent and adsorbate, then, the process is a chemical adsorption or chemisorption. In the case of electron transfer, the adsorption is of high energy, ranging from 40 to 800 kJ/mol and, consequently, desorption is difficult, and thus the process is irreversible, and only a monolayer is observed. Otherwise, if no electron transfer occurs, either ionic adsorption or physisorption occurs. In this case, the adsorption energies are lower, ranging from 5 to 40 kJ/mol and, consequently, desorption is easier than in chemisorption, and the process can be reversible, and multilayer adsorption is possible. Each case should be examined separately. Depending on if chemisorption or physisorption is the main route for the adsorption process, it will involve one or more of the following interactions:

- *Surface complex formation*: The formation of complex coordination bonds between metals and ligands at the surface, similar to the formation of complexes in solution.
- *Electrostatic interactions*: Solid surfaces are typically electrically charged. This electrostatic force, which is effective over greater distances than purely chemical forces, affects the surface complex formation and loosely binds other ions to the surface.
- *Hydrophobic adsorption*: Many organic substances, most notably lipids, are highly insoluble in water due to their non-polar nature. These substances become adsorbed to surfaces, not because they are attracted to the surface, but rather because they are repelled by water³.
- *Surface precipitation*: It can occur at metal ion concentration and pH values below those required for precipitation of the pure solid phase from aqueous solution⁴, due to the high metal concentration on the diffusion layer
- *Ion exchange*: including lattice-ion exchange and counterion exchange. Usually occurs throughout a polymeric solid. In ion exchange, ions of positive charge in some cases (cations) and negative charge in others (anions) from the fluid (usually an aqueous solution) replace different ions of the same charge initially in the solid.
- *Hydrogen-bonding*: important polar interaction in aqueous media. It can be considered as an extreme manifestation of a dipole-dipole interaction, which typically arises when hydrogen is attached to very electronegative atoms.

Adsorption process and mechanism will depend on the nature of the adsorbate, adsorbent surface and the pH of the solution (which influence previous ones). In this case, Sb speciation as a function of the pH has been described in Chapter 3. Here, the pH influence on the SPION surface is introduced due to the importance of surface groups on the sorption mechanism. Also, the main interaction that could be created for the Sb adsorption will be explained for a better understanding of Sb sorption mechanism on SPION.

1.2. Metal oxide surface in water

Surfaces are important because no material exists without surfaces. Fortunately, surfaces are the border between two phases, such as the solid and solution phase. Thus, part of the characteristics of surfaces originates from the underlying materials, but its behaviour is also determined by the bordering phase, e.g., an aqueous solution.⁵

Metal (hydr)oxide surfaces are widely studied because of their capability to interact with cations and anions. Considering a metal oxide surface, oxygen and metal atoms present at an oxide surface are incompletely coordinated hence have a partial charge (Figure 6.2a). Consequently, iron oxide surfaces immersed in water attract and bind water molecules (Figure 6.2b). The water molecules then dissociate, leaving a hydroxyl group bound to the surface metal ions (Figure 6.2c) (Equation 6.1):



Similarly, unbound oxygens react with water to leave a surface hydroxyl group (Equation 6.2):



The surface quickly becomes covered with hydroxyls ($\equiv\text{SOH}$), considered part of the surface rather than the solution. These hydroxyls can then act as either proton acceptors or proton donors through further association or dissociation reactions (Equations 6.3 and 6.4):

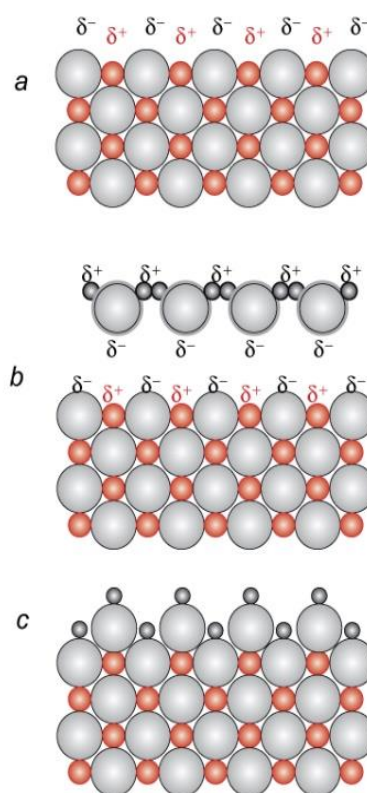
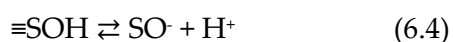
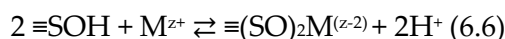


Figure 6.2. Interaction between water and SPION surface (Oxygen grey; metal, red and hydrogen dark grey)

We should not be surprised to find that these kinds of reactions are strongly pH-dependent. The protonated and deprotonated surface hydroxyl groups are shown in Equations 6.3 and 6.4 may further change in the presence of metal ions and form complexes involving one or two surface hydroxyl groups⁶ such as in Equation 6.5 and 6.6.



The complex and the sorption mechanisms for the formation of compounds in the last equations are explained in the next section.

1.3. Adsorption on inorganic species by metal oxide materials

In water treatment applications, the metal ion species in solution have to migrate to the surface of the suspended oxide, and they are either attracted or repulsed depending on the electric charge. When they are attracted, they get attached to a defect site first as a unimolecular layer and later in multilayers, depending on the concentration and porosity of the surface and the surface layer. Chemical reactions between the metal ion and the surface hydroxyl/hydrogen groups or ligand exchange may take place, and the metal ion is attached strongly. If the chemical reaction product is insoluble, it may deposit on the surface, and further diffusion is blocked, or a new surface with the properties of the new deposited surface may come into play.

This adsorption process could be produced due to different mechanisms (Figure 6.3):

- a) Adsorption of metals to the surface may occur through replacement of a surface proton.
- b) Ligands may be absorbed by replacement of a surface OH group.
- c) The adsorbed metal may bind an additional ligand.
- d) The adsorbed ligand may bind an additional metal.
- e) and f) An additional possibility is a multidentate adsorption, where a metal or ligand is bound to more than one surface site.

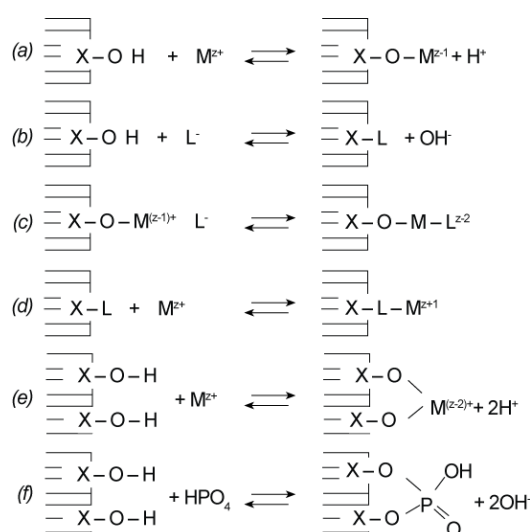


Figure 5.3. Different adsorption mechanisms on metal oxide

The chemical interaction of ions is strongly influenced by the electrostatic interaction between the surface and the adsorbing ions, which both are pH-dependent⁵. Adsorption of cations increases with increasing pH. Figure 6.4 shows that adsorption of metals on goethite goes from insignificant to nearly complete over a very narrow range of pH. This reflects surface protonation, at low pHs, but it also reflects the deprotonation and the extent of the hydrolysis of ions in solution as the pH increases.

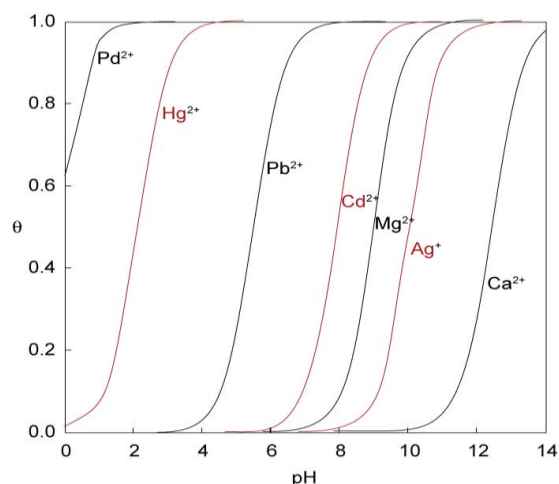


Figure 6.4. pH influence in cations adsorption

However, in Figure 6.5, the adsorption of anions decreases with increasing pH. As the pH increases, the surface charge is getting negative as the pHzc is reached, enhancing repulsive forces between surface groups and anions in solution.

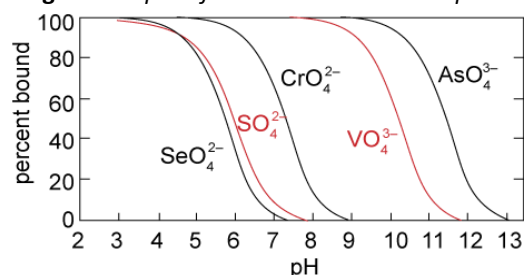


Figure 6.5. pH influence on anions adsorption

Independently if a cation or anion is adsorbed, two types of interaction can be performed. Strong interactions are generally related to the formation of inner-sphere complexes. Interactions forming outer-sphere complexes are weaker than inner-sphere. Combinations of inner- and outer-sphere complex formation are also reported⁵. These bonds are shown in Figure 6.6.

Inner- and Outer- sphere complex

Inner sphere complexes involve some degree of covalent bonding between the adsorbed species and atoms on the surface. It involves direct coordination of metal ion to a surface hydroxyl group by chemical binding (Equation 6.7). The surface hydroxyl group acts as a Lewis base containing non-bonding occupied orbitals (“lone pairs”). Interaction of a Lewis acid (metal ion, in our case, Sb) with the Lewis base ligand results in strong chemical bonds. Resulting distances between the metal ion and surface hydroxyl oxygen are relatively small⁷. This complex could be monodentate or bidentate complexes.

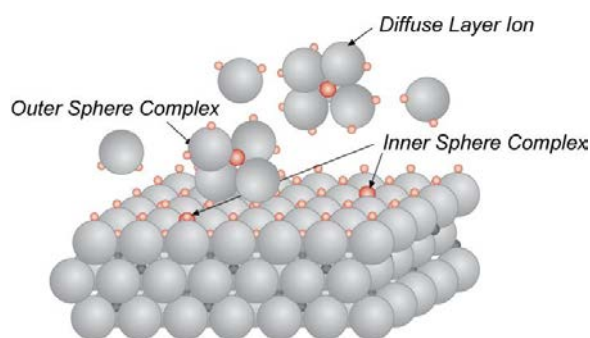
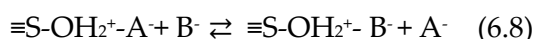


Figure 6.6. Inner-sphere and Outer-Sphere complexes



In an outer sphere complex, one or more water molecules separate the adsorbed ion and the surface (Equation 6.8); in this case, adsorption involves only electrostatic forces. The interaction is weak and has a large electrostatic contribution where a purely electrostatic attachment of negatively charged anions to positively charge surface hydroxyl groups takes place, whereby the hydration sphere of the metal ion remains unaffected⁷. The outer-sphere complexes have no common ligands with the metal ions of the adsorbent and remain at some minimum distance of approach.



IR and Raman's spectroscopy have shown that some oxoanion compounds as selenate SeO_3^{2-} ^{8,9}, sulphate SO_4^{2-} ¹⁰ and arsenate AsO_4^{3-} ^{11,12} may form inner- and outer- sphere complexes. Outer-sphere complex formation occurs at high pH, whereas at low pH, these anions are mainly bound as a monodentate inner-sphere complex. The pH-dependent partitioning of an ion between outer- and inner-sphere complexes is due to the difference in the structure of both complexes, resulting in a different location of the charge in the electrostatic field and a different pH dependency. The outer-sphere complexes will attribute less negative charge to the surface than the inner-sphere complexes, which lead to less co-adsorption of protons and a smaller pH dependency than the inner-sphere complex. Spectroscopy shows that, at high pH, the outer-sphere complex dominates⁵. The inner-sphere species may also be present but at a lower adsorption density. With lowering pH, the adsorption density of the outer-sphere complex will increase, but the inner-sphere complex will increase more because it has a larger pH dependency. The inner-sphere complex will, thus, start to dominate at some point and will further increase its relative presence due to mainly electrostatic competition between the inner- and outer-spheres complexes⁵.

The third possibility is that an ion may be held within the diffuse layer by long-range electrostatic forces

1.4. Spectroscopy method for sorption mechanism determination

Spectroscopy methods are extensively used to study the adsorption mechanisms of ions on surfaces based on the isoelectric point, surface morphology, ionic valence state and bonds with neighbouring atoms, surface functional group and spatial structure.¹³ Spectroscopy techniques are necessary to constrain the selection of surface complexes and surface reactions construction, in order to undertake reliable modelling work¹⁴, and include Fourier transform infrared (FTIR), X-ray absorption spectroscopy (XAS), X-ray photoelectron spectroscopy (XPS), and Raman spectroscopy.

No single technique can provide a complete description of the surface or the surface species. Due to the characteristics of the material and the techniques available, FTIR and XAS have been used for the study of Sb on the sponge and Sponge+SPION system. Several of these methods are summarised below, along with examples of the types of data derived from each method. However, more details of both techniques are included in Annex 1.

Infrared spectroscopy has proven to be a useful technique for studying the interactions of ions with surfaces. IR provides chemical bond information and can be utilised to distinguish the outer and inner layers of the complexation structure of an adsorption product, and it is an effective tool for studying the behaviour of Sb during adsorption. Direct evidence for inner-sphere surface complexation of anions via ligand exchange has come from IR spectroscopic characterisation using both dispersion IR and Fourier transform infrared (FTIR) spectrometers. One of the advantages of FTIR is that water peaks can be subtracted mathematically, allowing analyses of more realistic wet systems, unlike dispersion IR, which must be performed in a vacuum. Artefacts can be produced when extrapolating results from evacuated samples to aqueous solutions. For example, results from evacuated systems showed a predominance of bidentate surface complexes for most anions. However, the addition of water to bidentate surface complexes will drive the equilibrium to favour the formation of monodentate surface complexes¹⁵. The development of Attenuated Total Reflection infrared (ATR-FTIR) spectroscopic methods has led to many studies of species adsorbed to metal oxides, including iron oxides, but the application of this approach to investigate the molecular nature of adsorbed antimonate species has not hitherto been reported.¹⁶

An useful spectroscopic technique based on synchrotron radiation sources¹⁷, that has provided important insights into the mechanisms of metal sorption to mineral surfaces, is X-ray Absorption Spectroscopy (XAS). This method can be used on in situ samples with high sensitivity. Thus, it is considered the most effective means to study the adsorption mechanism of metal-metal systems with unique advantages in defining the microstructure of adsorbed products and providing an opportunity to model inner- or outer-sphere complexation. The fine structure of the X-ray absorption (XAFS) is also used to analyse the types of adsorption products. XAFS consists of the Near-Edge (XANES) and the Extended portions (EXAFS).

Synchrotron-based XANES analysis provides a powerful and unique method of characterising the oxidation state, chemical form, and local coordination environment of an element associated with various minerals and phases. XANES is an especially valuable tool when the sample volume is small, the sample is fine-grained, and the element is present in low concentrations or is sensitive to redox changes during sample preparation¹⁸. Extended X-ray absorption fine structure spectra (EXAFS) provide information including the average distance to, and the number and identity of atoms, in

the first and second coordination shells ($\sim 6 \text{ \AA}$ radius) around a metal ion. This information is used to determine whether the ion is adsorbed to the surface as an inner-sphere or outer-sphere complex, as a monodentate, bidentate, or tridentate complex, and as a mononuclear or multinuclear complex, or as a precipitate¹⁵.

In this work, the possible mechanisms and binding sites involved in the Sb adsorption are discussed based on the data obtained from pH influence adsorption experiments, pHzc data (from Chapter 4), Fourier Transform Infrared analysis (FTIR), Scanning Electron Microscopy (SEM) equipped with Energy Dispersive Spectrometer (EDS) and X-ray Absorption Spectroscopy (XAS) analysis.

2. OBJECTIVES

The main objective in this Chapter is to elucidate the mechanisms of interaction between Metalzorb® sponge and sponge+SPION with Sb in aqueous systems, combining mass spectroscopy and spectrophotometric techniques. For this purpose:

- The solution pH in the adsorption process has been studied as a key parameter affecting Sb adsorption. The goal is to explain how the pH affects both the Sb in solution and the SPION surface in the sorption mechanism.
- SEM-EDS is used to analyse the chemical elements on the material surface, present before and after Sb adsorption to support the results obtained on the pH influence.
- FTIR measurements and data analysis have been performed to identify the functional groups that are involved in the Sb adsorption.
- Synchrotron-radiation-based XANES and EXAFS analyses were employed to probe the molecular binding mechanism and possible redox reactions of the adsorbed Sb on SPION-sponge surfaces.

3. MATERIALS AND METHODS

3.1. Chemicals and reagents

Metalzorb sponge® was kindly supplied by Cleanway Environmental Partners, Inc. (Portland, USA).

It is an open-celled cellulose sponge which incorporates a water-insoluble polyamide chelating polymer (formed by the reaction of polyethyleneimine and nitrilotriacetic acid). This sponge contains free available ethyleneamine and iminodiacetate groups to interact with heavy metals ions by chelation and ion exchange¹⁹.

Analytical grade $\text{FeCl}_3 \cdot 6\text{H}_2\text{O}$ (Sigma-Aldrich, Germany), $\text{FeCl}_2 \cdot 4\text{H}_2\text{O}$ (Acros Organic, Belgium), CH_3COOH glacial (J. T. Baker, Germany), $\text{CH}_3\text{COONa} \cdot 3\text{H}_2\text{O}$ (Panreac, Spain) were used to prepare the solutions needed. Stock solutions of antimony (III) and antimony (V) were prepared from $\text{C}_4\text{H}_4\text{KO}_7\text{Sb} \cdot 0,5\text{H}_2\text{O}$ (Fluka, Switzerland) and $\text{K}[\text{Sb}(\text{OH})_6]$ (Scharlau, Spain) respectively. Double distilled water with a resistivity of $18 \text{ M } \Omega\text{m}^{-1}$ was used throughout all the experiments.

3.2. Synthesis of adsorbent materials

3.2.1. Sponge pretreatment

The sponge pretreatment was performed as described elsewhere¹⁹. Previous to the pretreatment, the sponge in cubic form was dried at 40°C for 24 h and then ground to obtain sponge powder. Then, the pretreatment is performed. The sponge powder was immersed in a hydrochloric acid solution for wiping their acidic form to activate the amino groups and to facilitate SPION immobilisation. This pretreatment is commented more detailed in Chapter 4, section 3.2.1.

3.2.2. Sponge+SPION system synthesis

SPION was synthesised directly onto the sponge by co-precipitation method²⁰. $\text{FeCl}_2 \cdot 4\text{H}_2\text{O}$ and $\text{FeCl}_3 \cdot 6\text{H}_2\text{O}$ in a molar ratio of 1:2 were dissolved in 100mL deoxygenated water in the presence of the sponge, under N_2 bubbling and at 40°C . After 1 h, 125 mL of deoxygenated aqueous solution of NaOH 0.5 M was added slowly while stirring the mixture. Then, the suspension was incubated for 1 h at 40°C .

During the incubation, the sponge acquired a darker colour due to the formation of Fe_3O_4 nanoparticles on the sponge. The final product was washed with deoxygenated water and magnetically separated from the washing solution. The washing process was repeated three times to remove any unreacted chemicals. More details about this synthesis and about the material characterization are described in Chapter 4.

3.3. Adsorption experiments

Experiments to determine the pH influence on Sb(III) and Sb(V) adsorption and chemical stability of sorbents were carried out with a 10 ppm solution in a pH range of 2 to 11 adjusted by acetic/acetate buffer 0.1M, HCl 0.1 M and NaOH 0.1 M. 25 mg of sorbent and 2.5 mL of an aqueous solution of Sb(III) or Sb(V) were shaken in 50 mL polypropylene tubes using a rotatory shaker, at room temperature for 24 h. After mixing, the solid phase was removed from the supernatant by filtration with cellulose acetate filters of 0.22 μm . The final pH was used as the pH value of the experiment.

The adsorption capacity (q_e , mg Sb/g adsorbent) is determined by applying equation 6.9 to the measured initial (C_o , mg/L) and equilibrium (C_e , mg/L) antimony concentration values of each experiment.

$$q_e = \frac{V(C_o - C_e)}{m} \quad (6.9)$$

where V (L) is the solution volume and m (g) is the adsorbent quantity. The concentration of metal ions in supernatant solution was determined by inductively coupled plasma mass spectrometry (ICP-MS, Thermo XSeries II, Thermo Scientific).

3.4. Characterisation

As indicated previously, in order to understand the binding mechanisms of the antimony adsorption process on both sponge and sponge+SPION adsorbents, the pH influence on Sb(III) and Sb(V) adsorption have been studied.

In addition, to get a deeper knowledge of these processes, samples of both sponge and sponge+SPION adsorbents after corresponding Sb adsorption experiments under pH for maximum capacity, were analysed by Transmission-Fourier Transform Infrared spectroscopy (FTIR) and the Energy Dispersive Spectrometer (EDS) capability of the Scanning Electron Microscopy (SEM).

Separate experiments at Synchrotron facilities were done, using such sponge samples, for X-ray Absorption Spectroscopy (XAS) measurements at the Fe and Sb K-edge to provide specific information on the oxidation state and the local coordination environment of Sb thus, complementing a better understanding the related adsorption mechanism.

FTIR was conducted on a Vertex70 spectrometer (TE Cooled DLaTGS Detector with KBr windows from 12000 to 350 cm^{-1} and 256 scans) in transmission mode. Samples for FTIR measurements were prepared as it was explained in section 3.3 related with adsorption

experiments, but the initial concentration was increased until 100 ppm of Sb in the solution, reaching at maximum sorption capacity around 10 mg Sb/g in both material and for both Sb species. These samples were ground with KBr in an agate mortar under a heat lamp, by mixing a fixed amount of sample (1% w/w) in KBr which was used to prepare the pellet.

A Scanning Electron Microscopy (SEM) (FEI Quanta 650F Environmental SEM) equipped with an Energy Dispersive Spectrometer (EDS) was used to determine other chemical elements present in the sponge after the adsorption of Sb(III) and Sb(V).

Samples used for XAS synchrotron measurements were prepared as it is explained in section 3.3. The pH was adjusted to 3.6, 5.6, and 11 using 0.1 M acetic/acetate buffer and NaOH 0.1M as appropriate. The aqueous and the solid phases were separated by centrifugation for the sponge and by decantation with a magnet in the case of the sponge+SPION system. The obtained solids were cleaned, dried and stored in 5 ml of sealed polypropylene tubes at room temperature before XAS measurements. Standard references of Sb_2O_3 , $\text{K}[\text{Sb}(\text{OH})_6]$, $\text{C}_4\text{H}_4\text{KO}_7\text{Sb} \cdot 0.5\text{H}_2\text{O}$, $\text{FeCl}_2 \cdot 4\text{H}_2\text{O}$, $\text{FeCl}_3 \cdot 6\text{H}_2\text{O}$, were also measured. All samples were milled, homogenised and pressed into a pellet. The samples were sealed in Kapton tape to help their manipulation. The appropriate amount of each reference compound was mixed with cellulose to obtain the optimum absorption jump. The homogenised mixture was also pelletized. The necessary amount of sample in each pellet was calculated with Absorbix v3.02.S3²¹.

XAS measurements were performed at the SpLine Spanish CRG Beamline BM25A at the European Synchrotron Radiation Facility (ESRF), Grenoble, France. The incident beam was monochromatized with a -70 °C ethanol cooled double Si(111) crystal, which gives an energy resolution of $\Delta E/E = 1.5 \cdot 10^{-4}$. An Sb foil and a Fe foil were used for energy calibration (30491 eV and 7112 eV respectively). Pure references compounds were measured in transmission mode at the Sb and Fe K-edges. The fluorescence detection mode was used for measuring at Sb K-edge. For this mode, a 13-elements Si(Li) solid state detector liquid nitrogen cooled was employed. Ionization chambers were used for monitoring the intensity of the beam for the measurements performed in transmission mode. Samples were fixed on a sample holder oriented at 45° to the orthogonal direction of the beam.

The XAS spectra were normalised to eliminate thickness dependence. The EXAFS signals were extracted following standard procedures using the program ATHENA and fitted using ARTEMIS. Both programs are distributed with the Demeter software package²². Pseudo radial distribution functions were obtained by Fourier transform of k^2 -weighted EXAFS signal within the k -range: 3.5–10.8 Å⁻¹ using a Kaiser-Bessel window.

4. RESULTS

Obtained results will include pH effects on the adsorption process and the different spectroscopic characterization studies of the adsorbent loaded samples.

4.1. pH influence

The influence of solution pH on the removal of Sb(III) and Sb(V) from wastewater using the sponge and sponge+SPION systems was examined since pH plays a crucial role in the antimony speciation and the protonation of the chemical groups of the surface, which are leading factors in adsorption processes. In addition, the Fe loss after the adsorption process was examined.

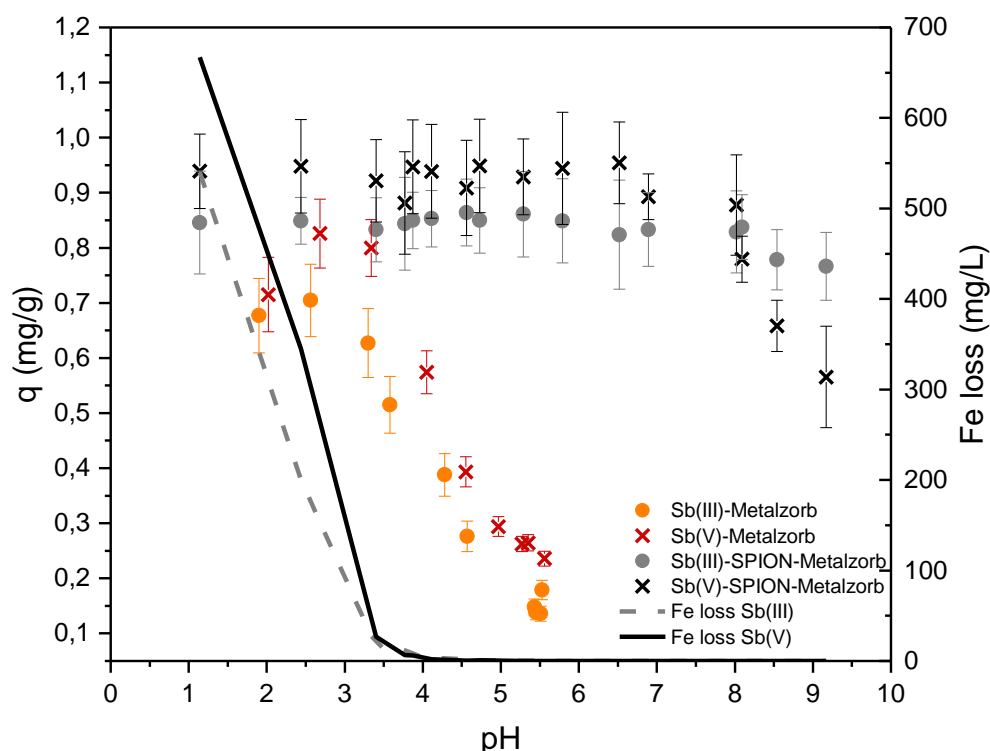


Figure 6.7. Effect of the pH on the adsorption of Sb(III) and Sb(V) in both materials. Working conditions: 25 mg of adsorbent, $[Sb]_{initial} = 10\text{ppm}$, 4h, 20°C.

As expected, the adsorption of Sb(III) and Sb(V) by the sponge is strongly dependent on pH. Figure 6.7 shows that when the initial pH rises from 2 to 3, the adsorption capacity increases slightly, reaching the maximum sorption capacity at pH 2.4 and 2.8 for Sb(III) and Sb(V), respectively (Figure 6.8). At that point, it decreases sharply as the pH increases, reaching a final pH of 5.5. This behaviour can be understood by taking into account the antimony speciation in aqueous solution and the pH-dependent properties of the adsorbent surface.

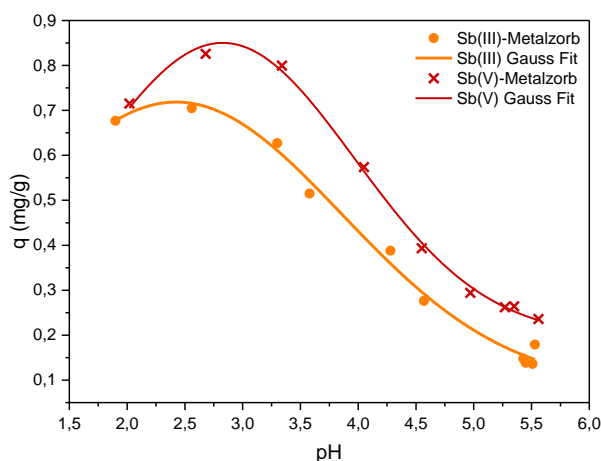


Figure 5.8 pH effect Gauss fitting

As seen in Figure 6.9, the speciation of antimony in aqueous solution depends on the pH and oxidation state²³. Sb(III) appears as a neutral compound, Sb(OH)_3 . It only appears as positive, Sb(OH)_2^+ , or negative species, Sb(OH)_4^- , under strongly acidic ($\text{pH} < 2$) or alkaline conditions ($\text{pH} > 10.4$), respectively. However, in the presence of tartrate, which is the Sb(III) complex used for this work, Sb(III) is found as the anionic Sb(III)-tartrate complex²⁴⁻²⁶, although certain percentage is also present as free Sb(OH)_3 depending on the initial concentration²⁷. The concentration of free Sb(III) as Sb(OH)_3 increases when the concentration of the Sb(III)-tartrate complex in solution reduces. For pH values higher than 2.7, Sb(V) is expected to be found as negatively charged species, Sb(OH)_6^- and it does only appear as neutral or positive species under strongly acidic conditions²⁸

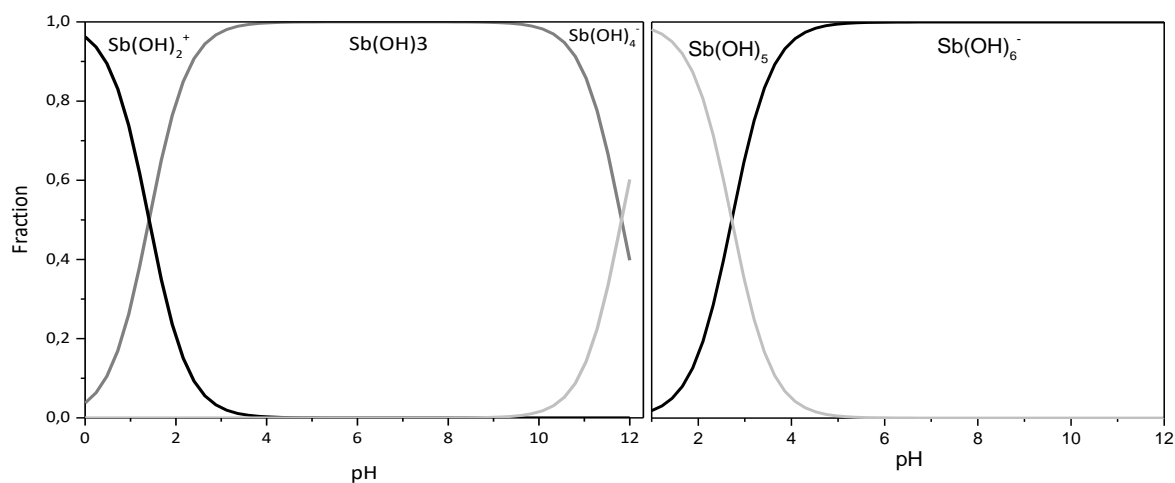


Figure 6.9 Speciation diagram of Sb in aqueous solution as a function of pH, 25 °C, theoretical data using HYDRA and MEDUSA software²⁹; a) Sb(III) diagram; b) Sb(V) diagram

On the other hand, the amino groups present in the sponge are protonated at pH lower than its pH_{zc} , which has been determined in Chapter 4, section 4.1.7. This is, for pH below 2.5 anions or negatively charged metals complexes could attach to the sponge¹⁹. Consequently, in agreement with the results shown in Figure 6.7 and 6.8, it is reasonable to think that Sb(III) and Sb(V) sorption on the sponge could be due to electrostatic

interactions or H-bonding, involving anionic antimony species and sponge protonated amino groups. In very acidic conditions, pH lower than 2.4 or 2.8 for Sb(III) and Sb(V), respectively, the adsorption is slightly less suitable probably due to the increase of electrostatic repulsion between positive species (Sb(III)) and sponge ammonium groups, and neutral species (Sb(V)) and the positive charge of the sponge ammonium groups. If the pH is increased beyond the pH_{zc} value, amine groups would be present in the neutral form.

Moreover, it is observed that the final pH (pH_f) is different from the initial pH (pH_{ini}), precisely, $pH_f < pH_{ini}$ when the pH is higher than 2 (Figure 6.10). This indicates a higher uptake of the hydroxyl ions present in the solution which compete with the antimony species and, as a result, there is a decreasing of the antimony sorption. In addition, the growth of OH^- in solution shifts the equilibrium to stabilise antimony species in the solution²⁴.

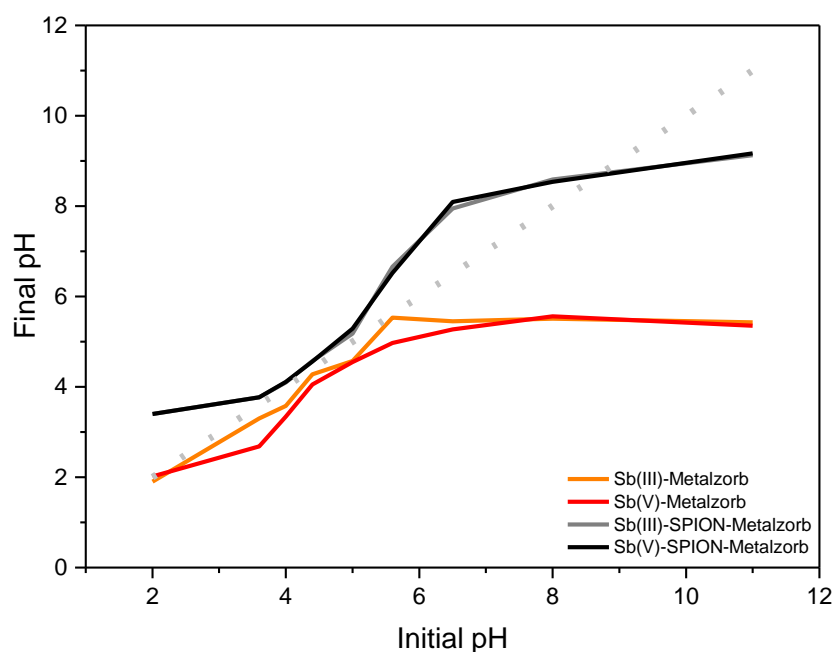


Figure 6.10. pH variation after Sb(III) and Sb(V) adsorption on the sponge and sponge+SPION system Conditions: 25 mg of adsorbent, [Sb]= 10ppm, 4h, 20°C

These results are confirmed by information obtained from the SEM-EDS analysis (Figure 6.11). For the sponge before the adsorption experiment (Figure 6.11a), the predominant elements present are carbon, oxygen and chloride. After adsorption (Figure 6.11 b and c), the chloride emission peak that it is expected at 2.6 keV cannot be distinguished from the background whereas the peaks for carbon and oxygen have still a strong contribution. In addition, the characteristics emission peaks for antimony are present. This suggests that the antimony adsorption on the sponge is produced by anion exchange, replacing chloride anions present on it.

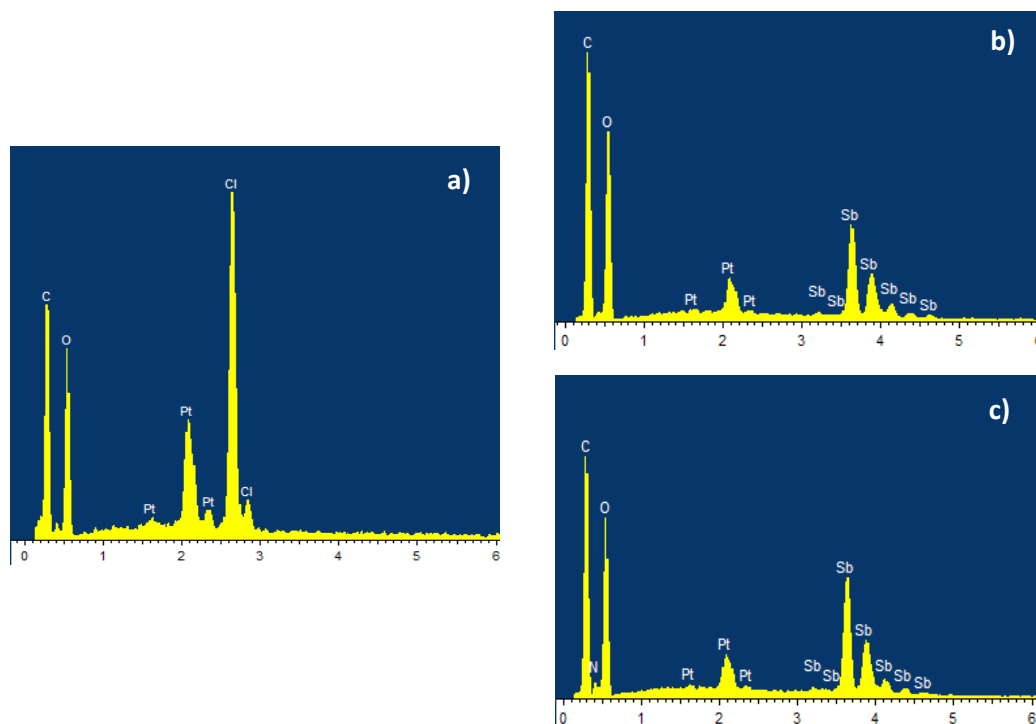


Figure 6.11. EDS of a) Sponge b) Sb(III) adsorbed on the sponge c) Sb(V) adsorbed on the[®] sponge. pH=3.

The presence of SPION improves the Sb(III) and Sb(V) sorption capacity, as observed in Figure 6.7. Regarding the dependence with pH, the adsorption of Sb(III) remains almost constant, whereas the adsorption of Sb(V) drops at basic pH ($\text{pH} > 8.0$). A decrease of Sb(V) down to 40% of the maximum value it is observed when reaching the pH of the pH_{zc} , pH 9 (determined in Chapter 4, sections 4.1.7). This behaviour can be interpreted considering two different types of interactions for each antimony species. In one hand, Sb(V) adsorption could be limited by anion exchange process with positive charge surface sites. SPION surface is pH-dependent, presenting a positive net surface charge when the pH is below 9 ($-\text{FeOH}_2^+$), a neutral when the pH is 9 ($-\text{FeOH}$) and negative if the pH is higher than 9 ($-\text{FeO}^-$)³⁰, as it is explained in Chapter 4. Whereas when increasing the pH, the negative charged sites on SPION surface increase, and this makes the repulsive forces between $\text{Sb}(\text{OH})_6^-$ and the negative sites of the surface grow, which produces an adsorption decrease. This behaviour could indicate that in Sb(V) adsorption on sponge+SPION system are involved electrostatic interactions by anion exchange³¹. In contrast, the adsorption of Sb(III) is less influenced by pH. Although Sb(III) is complexed with tartrate, free Sb(III), as $\text{Sb}(\text{OH})_3$, is present in the solution and it might also form a complex with iron that is stable over a wide pH range. Thus, when the amount of Sb(III) bound to iron increases, the concentration of Sb-Tartrate complex present in solution reduces and more free Sb(III) is present in the solution, what facilitates Sb(III) adsorption. Sb(III) is considered a stronger Lewis base than Sb(V)³². On the contrary, empty *d* orbitals in iron forming the SPION act as Lewis acids for the Sb electron-rich oxygen atoms, and consequently Sb can be adsorbed by creating oxygen bridges via ligand exchange with $-\text{OH}^-$ or $-\text{OH}_2^+$ groups located on SPION surface,

forming stable monodentate or bidentate inner-sphere complexes³³. Only at pH higher than 8, the adsorption slightly decreases. Leuz et al.³⁴ propose that adsorption of Sb(III) decrease due to the oxidation of Sb(III) and the subsequent desorption as Sb(V) in the presence of goethite. This oxidation process will be confirmed by XAS analysis.

It is also observed in Figure 6.10 that the adsorption process for both Sb species modifies the pH of the medium. In the pH range of 2-8, the pH of the solution shifts slightly to higher pH values. Above pH 8, the shift occurs toward lower pH. This slight shift in pH may be attributed to the adsorption reaction of Sb with the associated release of OH⁻ groups from the sorbent.

The concentration of Fe in water after adsorption under different pHs was measured in order to study the adsorbent stability. In Figure 6.7 is observed that the leaching of Fe under acidic conditions was significantly higher than the limit of iron concentration allowed in drinking water as established by the European Regulation (200 µg/L)³⁵. However, the Fe concentration in the final solution was negligible or not detected when the pH is higher than 4.5. These observations indicated that sponge+SPION system is a safe and stable adsorbent, when working in soft aqueous pH conditions.

All these results, together with the negligible iron loss of sponge+SPION system when the pH is higher than 4.5, allow us to determine that the optimum pH for this process are 3 for the sponge and between 4.5 and 8 for the sponge+SPION system.

4.2. FTIR analysis

FTIR spectrum of the sponge and sponge+SPION were measured to identify the functional groups which are affected by Sb adsorption. This information is useful to understand the binding sites of Sb on the different materials and therefore its adsorption mechanism.

Comparing the FTIR spectrum of the bare sponge before and after Sb adsorption, in Figure 6.12, some differences are observed. Due to the complexity of these spectrums and to better understand Sb adsorption affinity to single surface functional groups of the sponge (later on sponge+SPION system) FTIR analysis was conducted by first Savitzky-Golay (SG) second derivate and maximum normalisation.

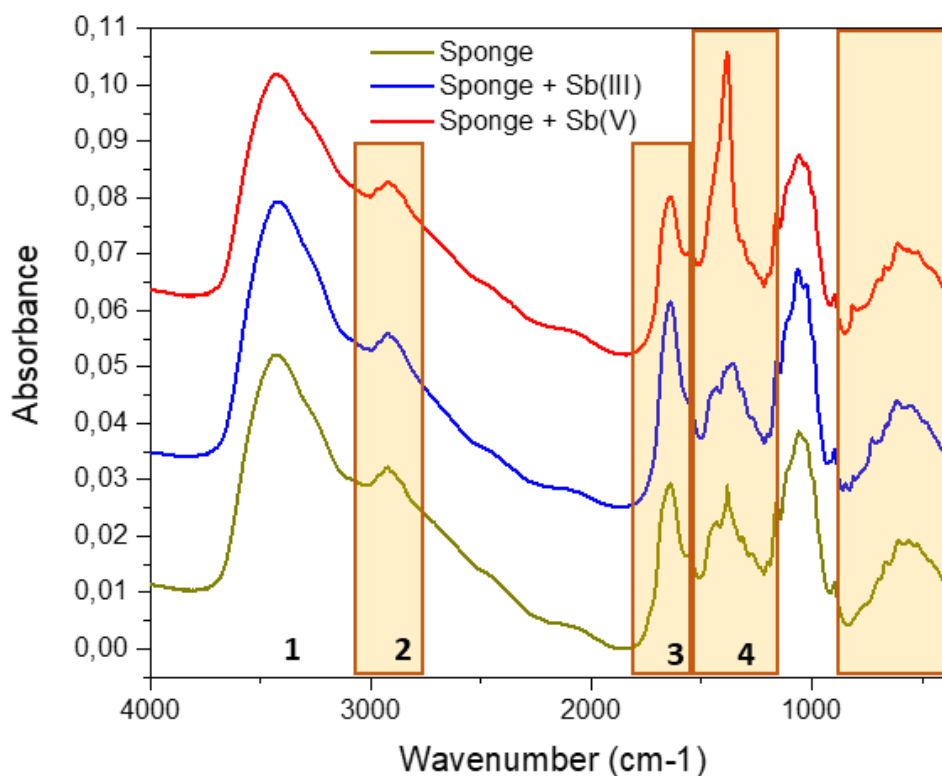


Figure 6.12. FTIR spectra of the bare sponge and for Sb(III) and Sb(V) adsorbed on the sponge

After Sb adsorption on the sponge, the appearance and disappearance of some bands are observed. For both Sb species, in 3700-3400 cm^{-1} region (Figure 6.12, region 1) it can be observed that there are changes on the position and intensity of peaks related to the modification of -OH groups, mainly to the presence of Sb^{36} , better observed in Figure 6.13. Bands at 2968 cm^{-1} and 2922 cm^{-1} (-CH₂ symmetric and asymmetric stretching) in the region 2 of Figure 6.12 also suffer modifications. In Figure 6.13, region 2, it can be observed as the first band, 2968 cm^{-1} , is shifted to higher wavenumber after Sb(V) adsorption whereas 2922 cm^{-1} band is shifted to low wavenumber for both Sb species. In addition, both bands increase their intensity upon Sb(V) adsorption. Moreover, the band related to -CH vibration at 1385 cm^{-1} , included in region 3 of Figure 6.12 is influenced by Sb (Figure 6.13). In the case of Sb(V), this band has an appreciable downshift. However, for Sb(III), the band maintains its position, but its intensity is reduced. The increase of these bands could indicate an increase in H-bonding after Sb adsorption³⁷, and the less intensity could indicate H-bonding breaking. The presence of less H-bonding when Sb(III) is adsorbed could be explained due to the existence of Sb(III)-tartrate complex. The presence of Sb-tartrate complex forces to move the amide group (amide V and VI) out of the plane by means of the -CH₂ groups which are next to the -CO and -NH groups. This implies a breaking of H bonds as is observed in the changes produced in the amide I and II (zone 3 and 4 in Figure 6.12) bands³⁸. The existence of this complex is confirmed due to the presence of bands characteristic of it:

- 617 cm^{-1} - Sb-O stretching³⁶
- 3435 cm^{-1} - -OH stretching vibrations of tartrate³⁹
- 1650 cm^{-1} - COO- antisymmetric stretching³⁹
- 1346 cm^{-1} - COO- symmetric stretching³⁹
- Doublet $1130\text{-}1070\text{ cm}^{-1}$ - axial stretching of C-O alcohol³⁹

These values are characteristics of coordination of carboxylic group to metal ions. Also, the intensity increase of the band at 1400 cm^{-1} is probably due to the presence of Sb(III)-complex, because of the 1400 cm^{-1} is the symmetric axial deformation of COO- in tartrate⁴⁰. Also, bands associated with amide vibration, in the regions 2 and 3 in Figure 6.12, suffered modification, which could be due to the effect of electrostatic interaction and H-bonding.

In case of Sb(V), new bands appear in zone 5 of the Figure 6.13 at 713 cm^{-1} (Sb-OH bending), 651 cm^{-1} (Sb-O stretching)⁴¹, 594 cm^{-1} (Sb(V)-O)⁴², 509 cm^{-1} (Sb(V)-O)³⁹, which are characteristic from $\text{K}[\text{Sb}(\text{OH})_6]$ and related compounds⁴³.

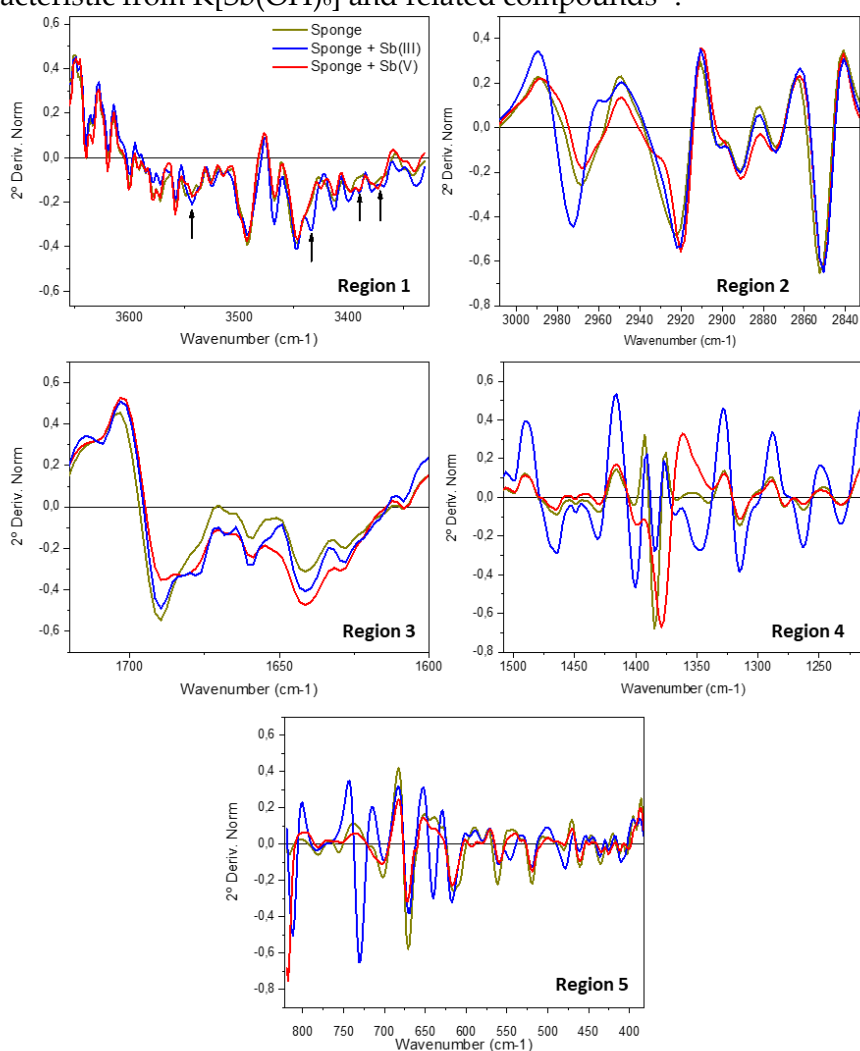


Figure 6.13. Sb(III) and Sb(V) adsorption on the bare sponge Savitzky–Golay second derivate and normalization at different ranges: region 1: $3650\text{--}3326\text{ cm}^{-1}$; region 2: $3000\text{--}2830\text{ cm}^{-1}$; region 3: $1720\text{--}1600\text{ cm}^{-1}$; region 4: $1508\text{--}1215\text{ cm}^{-1}$; and region 5: $822\text{--}382\text{ cm}^{-1}$

Similarly, Sb(III) or Sb(V) adsorption generate different effects in sponge+SPION FTIR spectrum. The 3600 – 3300 cm^{-1} region (zone 1 in Figure 6.14) is affected in a different way depending on the Sb speciation. Some bands in this region disappear after the adsorption of Sb (Figure 6.15), independent of the speciation, confirming the interaction between Sb and -OH groups at -Fe-OH. Other bands related to Fe-OH are affected because of the presence of Sb, like 796 cm^{-1} , 580 cm^{-1} and 443 cm^{-1} bands which are shifted to lower wavenumber or show an absorption loss. These changes on iron-related bands and the adsorption loss produced in -OH bands in the region 1 indicated the formation of chemical bands (-Fe-O-Sb)⁴⁴.

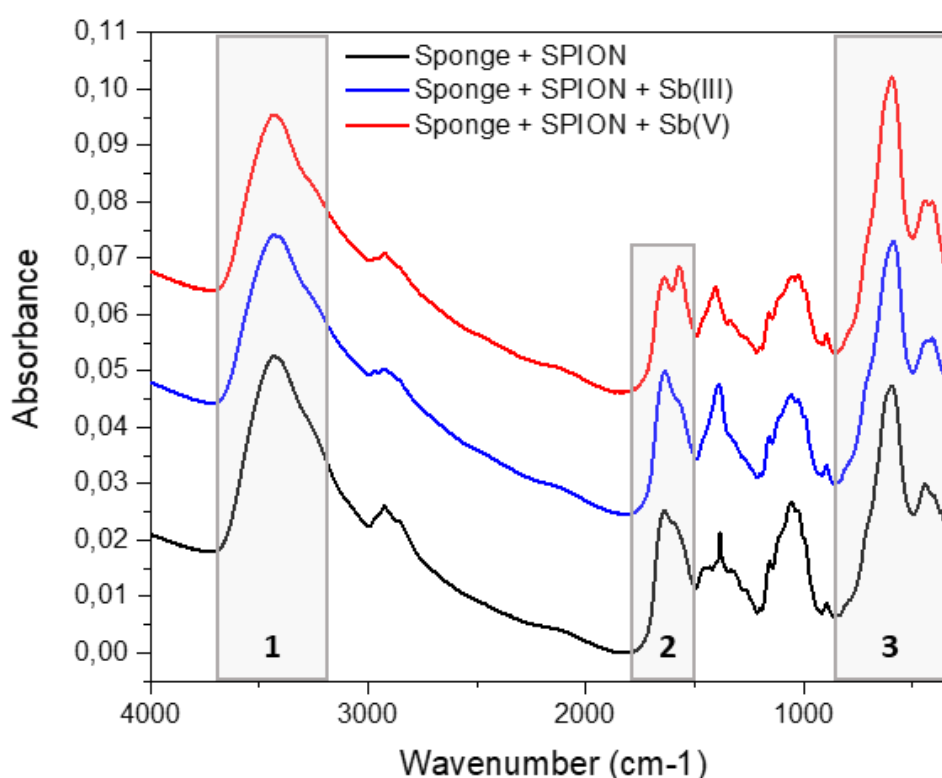


Figure 6.14. FTIR spectra of Sb(III) and Sb(V) adsorption on the sponge+SPION system.

The zone 2 is the most affected one after Sb adsorption. Sb(III) adsorption produces new bands (as it is observed in Figure 6.15) at 619 cm^{-1} and 431 cm^{-1} related to Sb-O stretching vibrations, and 568 cm^{-1} and 457 cm^{-1} from Sb(III)-O stretching and Sb-O-Sb bending, respectively. The small peak appearing at 590 cm^{-1} could be attributed to Sb(V)-O. This would suggest a possible oxidation of Sb(III) to Sb(V)⁴⁵, although it is risky to assess this fact due to the complexity of FTIR spectrum. XAS analysis may support or deny it (as will be shown later). Sb(V) adsorption also induce new bands formations in these regions, such as 700 cm^{-1} , 621 cm^{-1} , 586 cm^{-1} , 565 cm^{-1} and 451 cm^{-1} related to Sb-O-H out of plane deformation, Sb-O stretching⁴¹, Sb(V)-O stretching⁴² and Sb-O-Sb bending⁴⁶, respectively.

The FTIR spectra of the sponge and the sponge+SPION systems after Sb(III) adsorption shows some remarkable differences. Whereas, after Sb(III) adsorption on the sponge, the characteristics bands of tartrate-Sb(III) complex are observable, after its adsorption on the sponge+SPION system these bands have disappeared, indicating that in the adsorption mechanism of Sb(III) on this adsorbent the Sb(III)-complex is not present, and the interaction should occur between Fe and Sb(III) via oxygen bridge. On the other hand, the spectra after Sb(V) adsorption for both materials are very similar to the original material, except in the 600 – 400 cm^{-1} where Sb(V) band appears and the interaction with Fe-O is observed. It should be noted that in 3600 – 3300 cm^{-1} region are significant differences. Whereas the Sb(V) adsorption on the sponge spectrum is similar to the bare sponge, the spectrum after Sb(V) adsorption on sponge+SPION is very different, indicating the different sorption mechanism in the different materials. Furthermore, the bands related to $-\text{CH}_2$ absorption are affected, as in the sponge, increasing their intensity, and in some cases, a shifting is observed. These observations indicates the increase of H-bonding with $\text{Sb}(\text{OH})_6^-$.

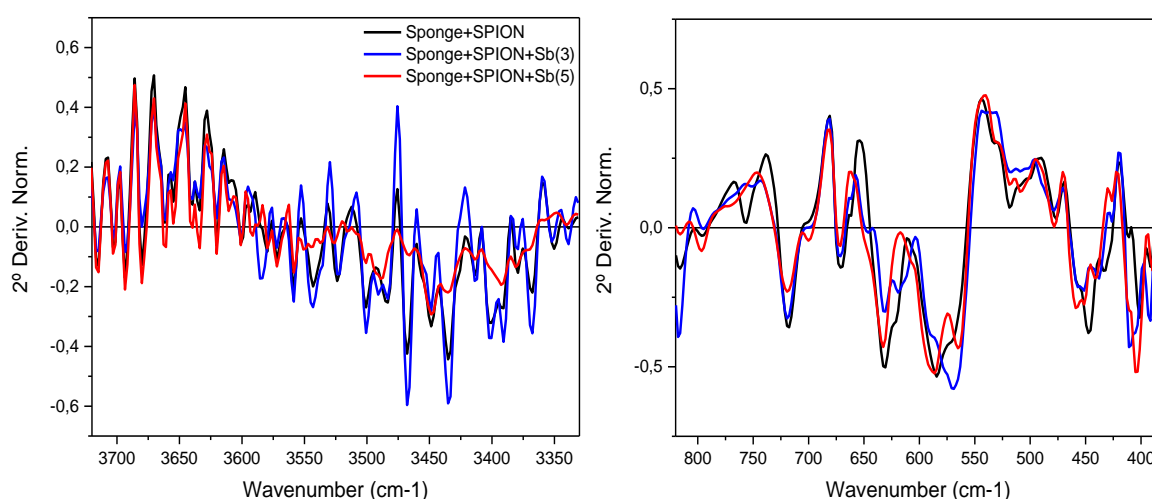


Figure 6.15. Sb(III) and Sb(V) adsorption on the sponge+SPION Savitzky–Golay second derivative and normalization at different ranges: region 1: 3600 – 3410 cm^{-1} ; region 2: 822 – 382 cm^{-1}

4.3. XAS measurements

To understand the binding mechanisms of the antimony adsorbed in the target adsorbents at different pHs, X-ray Absorption Spectroscopy (XAS) measurements were carried out on corresponding Sb loaded samples at Sb K-edge. Figures 6.16 and 6.17 show a comparison of the Sb K-edge spectra for Sb(V) and Sb(III) adsorbed in each one of target adsorbents. Regarding the reference compounds, as expected for lower oxidation states, the energy edge of the XANES spectra of the Sb(III) tartrate complex appears at lower energy (30492 eV) than the Sb(V) compound, $\text{KSb}(\text{OH})_6$, (30495 eV), and the white-line is less intense than in the case of Sb(V).

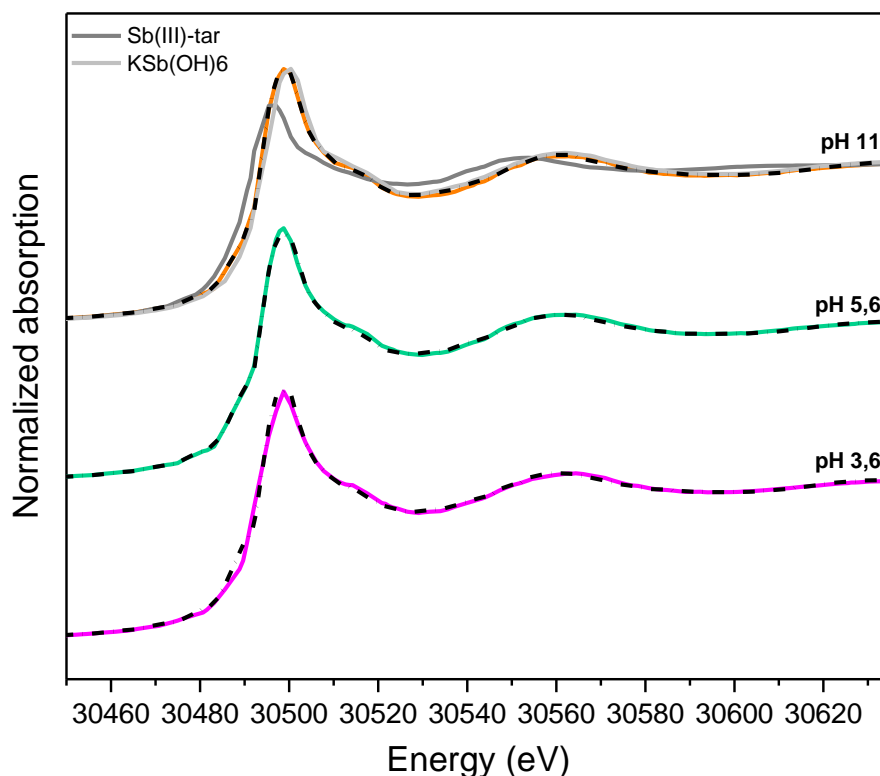


Figure 6.16 Sb(V). Normalised Sb K-edge XANES spectra for Sb(V) adsorption. Dashed line corresponds to sponge+SPION system while solid coloured lines represent the sponge. Grey lines correspond to Sb-XANES spectra of the reference materials (Sb(III)-tartrate complex and $\text{KSb}(\text{OH})_6$)

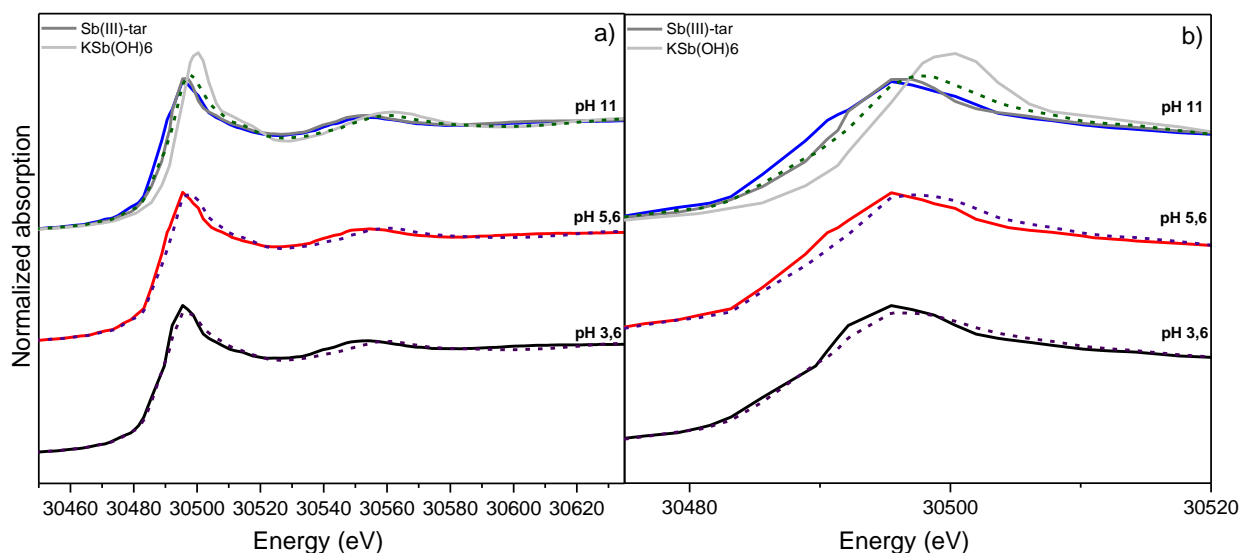


Figure 6.17. a) Normalised Sb K-edge XANES spectra for Sb(III) adsorption. Dashed line corresponded to sponge+SPION system while solid coloured lines represent the sponge. Grey lines correspond to Sb-XANES spectra of the reference materials (Sb(III)-tartrate complex and $\text{KSb}(\text{OH})_6$). b) whiteline enlargement

Figure 6.16 shows a comparison of XANES spectra of Sb(V) adsorption in the sponge and sponge+SPION systems at different pH. The spectra profile and position of the absorption edge is very similar for all the samples and it is almost identical to the Sb(V) reference compound. This results suggest that the chemical state and the local environment of Sb adsorbed species is similar to that of the reference compound, which

is six-coordinated in an octahedral geometry⁴⁷. Hence, it is highly probable that Sb(V) adsorption is performed by anion exchange mechanism, where only slightly changes will be appreciated due to alteration of the outer-sphere environment of the adsorbate from a close approach to the iron surface and interaction between adsorbed antimonate species¹⁶

For Sb(III) adsorption Figure 6.17 shows a comparison of XANES spectra in the sponge and sponge+SPION systems loaded with Sb(III) at different pH values. Sb(III) adsorbed on the sponge have a spectral profile similar to the Sb(III) reference compound (Sb(III)-tartrate complex), whereas Sb(III) adsorbed on sponge+SPION system is slightly different. The spectra of both samples are more similar to Sb(III)-tartrate reference. However, for the sponge+SPION system the white-line increases and shifts towards higher energy when increasing the pH, closing to Sb(V). This suggests that the presence of SPION produce the partial Sb(III) oxidation to Sb(V) which is favourable at higher pH. This result follows those obtained in the adsorption studies.

k² weighted EXAFS spectra of Sb(III) and Sb(V) adsorbed on the sponge (Figure 6.18) and sponge+SPION system (Figure 6.19) confirm the information obtained from the analysis of the XANES region. In the sponge without SPION, Sb(III) and Sb(V) samples are similar to the respective reference compounds. However, in the presence of SPION, there are no appreciable differences between Sb(III) and Sb(V) spectra. These similarities are greater as the pH increases, and all the spectra are like K₂Sb(OH)₆, used as a reference compound. According to this, it is reasonable to think that the presence of SPION favour Sb(III) oxidation to Sb(V).

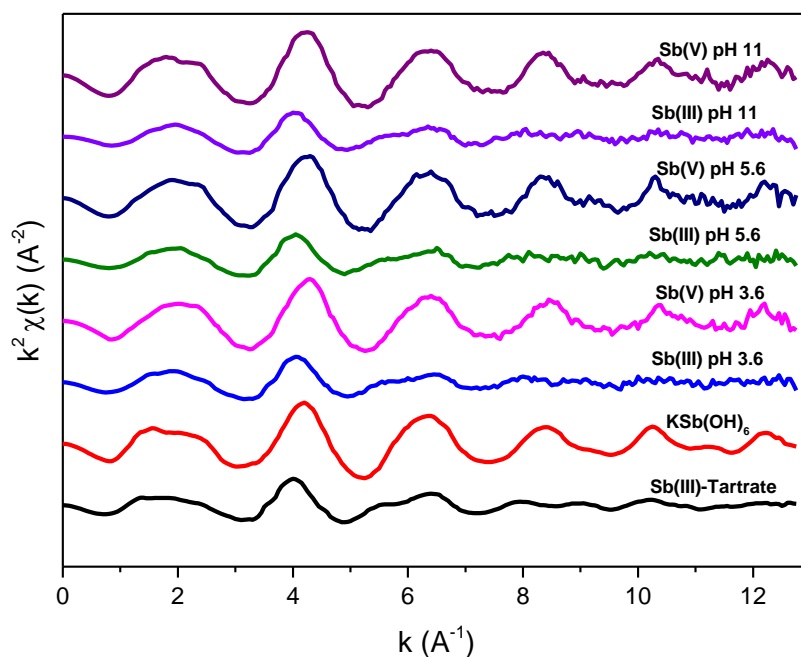


Figure 5.18 k^2 weighted EXAFS spectra of Sb(III) and Sb(V) adsorbed on the sponge and reference compounds (Sb(III)-tartrate complex and $K_2Sb(OH)_6$).

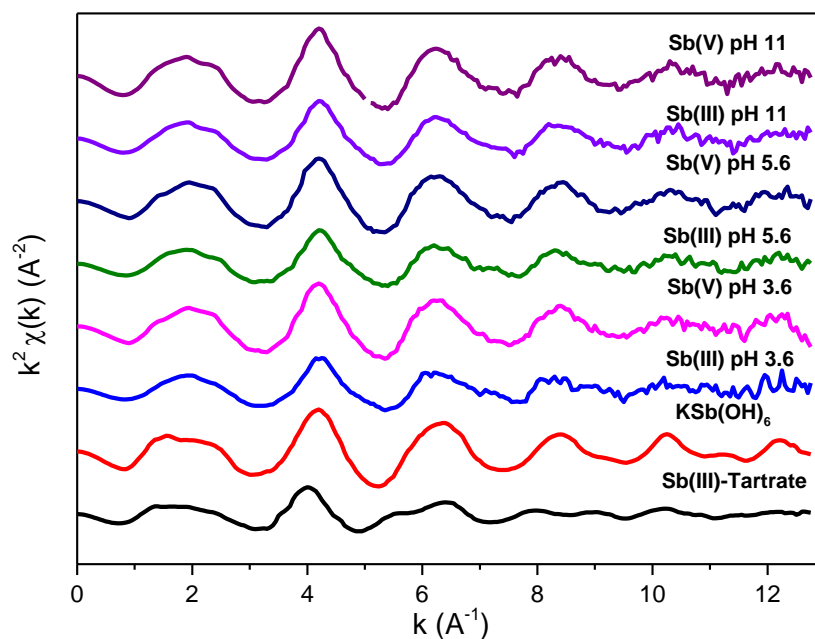


Figure 5.19 k^2 weighted EXAFS spectra of Sb(III) and Sb(V) adsorbed on sponge+SPION system and reference compounds (Sb(III)-tartrate complex and $K\text{Sb}(\text{OH})_6$).

Also, iron speciation after the adsorption has been studied. The normalised Fe K-edge XANES spectra of the different samples are shown in Figure 6.20. The direct comparison of XANES spectra determined that SPION keep the structure in the adsorption process in all cases, independently of the adsorbed species. This result was expected due to the ratio Fe/Sb present in the samples. SPION concentration in the samples, as it has been commented in Chapter 4, is around 40 %, whereas the Sb concentration is much less than the iron and if it is affected no observations will be shown in XANES spectra.

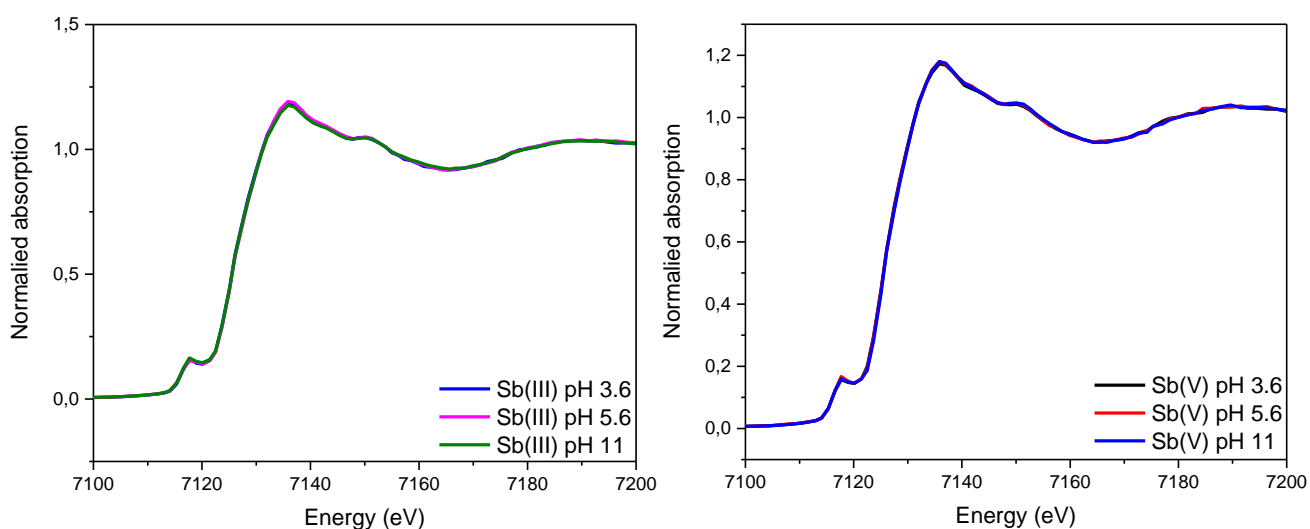


Figure 6.20 Normalized Fe K-edge XANES spectra for Sb(III) (left) and Sb(V) (right) adsorption.

4.4. Sorption mechanism

The study of Sb(III) and Sb(V) adsorption process on the sponge and sponge+SPION system has provided some information about their adsorption mechanism. Isotherm studies disclose that weak interactions are involved in Sb(III) and Sb(V) on the sponge, showing an S-type isotherm profile, which indicates a complete vertical behaviour of the adsorption capacity, possibly caused by surface precipitation of adsorbate on the surface of the adsorbent, where overall adsorbent–adsorbate interactions are weak in comparison with relatively strong adsorbate-adsorbate interactions. This behaviour was confirmed by selectivity and desorptions assays, which showed that both Sb species are desorbed easily in the presence of anions and complexant agents such as EDTA. On the other hand, adsorption of both Sb species on sponge+SPION system is performed by strong interactions. Isotherm profiles show an L-type shape which indicates chemical adsorption (chemisorption) and reflects a relatively high affinity between adsorbate and the adsorbent. The lack of anionic and cationic interference together with their difficult desorption with anionic and complexation stripping agents confirms the strong interactions between Sb and sponge+SPION system.

Taking into account the adsorption experiments FTIR and XAS result obtained in this Chapter, it is possible to state that Sb adsorption mechanisms on the sponge and the sponge+SPION system are different.

Adsorption experiments indicate that anion exchange is the main factor in Sb adsorption on the sponge, independently of its speciation, where the different pH affects the sorption capacity strongly. pH adsorption studies show that the high removal efficiency is reached at pH 2.4 and 2.8 for Sb(III) and Sb(V) adsorption, respectively, and it decreases when the pH is higher than these values, which is in concordance with pH_{zc} of the sponge, calculated in Chapter 4. This behaviour indicates that electrostatic interactions are also involved in the sorption mechanisms. XAS results confirm that Sb(III) and Sb(V) maintain their structure after the adsorption. Thus, no chemical bonds are formed between the sponge and Sb species. FTIR spectrum also confirms this fact, mainly for Sb(III) adsorption where the bands related to Sb(III)-tartrate complex are present. Moreover, FTIR results indicate the presence of H-bonding. Figure 6.21 explain the possible mechanism of Sb(III) and Sb(V) adsorption on the sponge. Figure 6.21a illustrates that the sponge is in its acidic form, where the positive charges on the surface are neutralised by the presence of the chloride anions (as SEM-EDS results shown in section 4.1). After the adsorption in Figure 6.21b, the chloride anions have been exchanged for Sb(III)-tartrate complex and Sb(V) anions and form electrostatic interaction and H-bonds with the positive charge of the surface. Both are weak interaction, which could be broken easily as it has been explaining in Chapter 5, in 4.5 section about the chemical desorption process

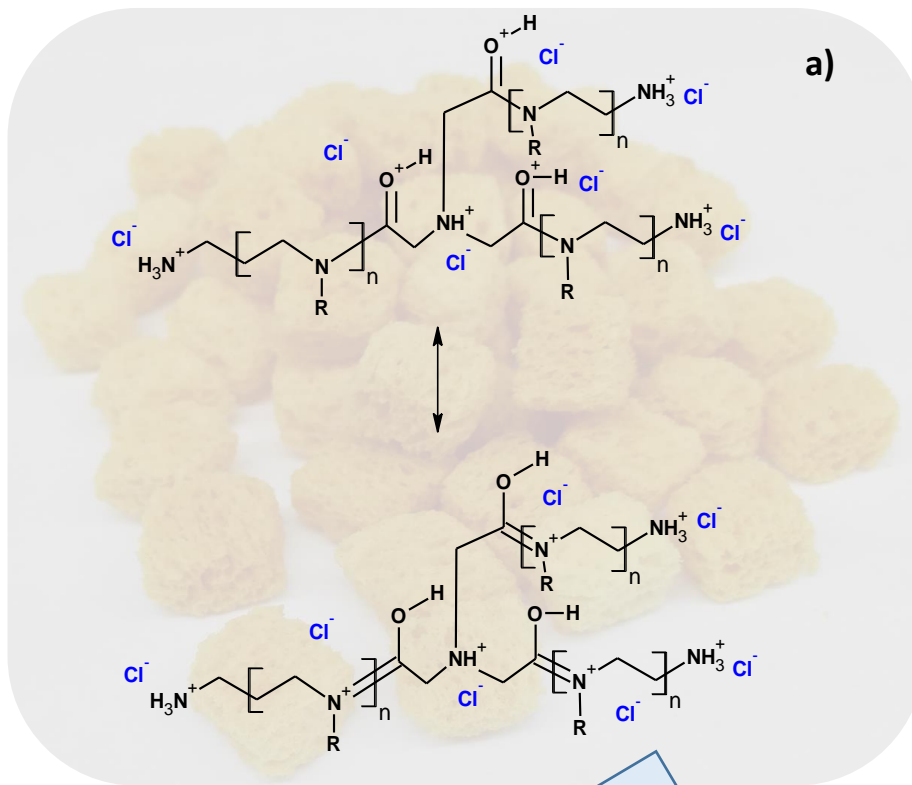
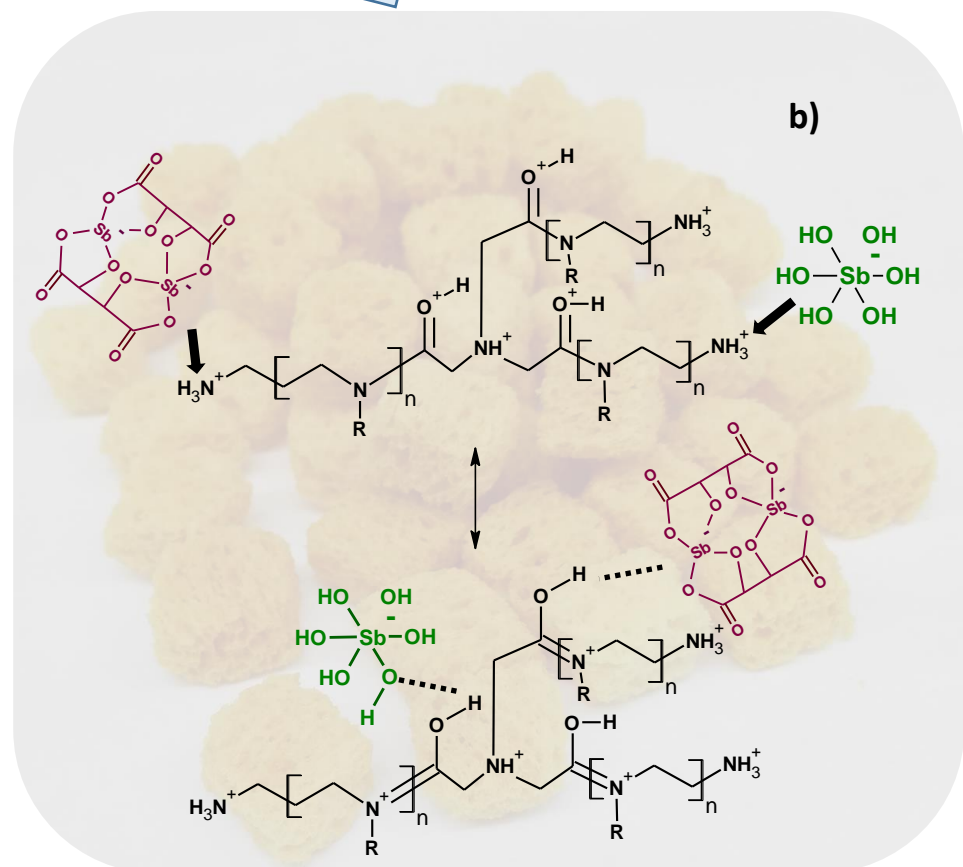


Figure 6.21. a) Sponge structure after acid pretreatment¹. b) Sb(III) and Sb(V) sorption mechanism on the sponge. Dashed line indicates hydrogen bonds and arrow indicate electrostatic interaction. Sb(III)-tartrate complex from Iyer et al. (1972)^{56,57}

**Sb(III) and Sb(V)
adsorption**



In addition, Sb(III) adsorption on sponge+SPION system presents different sorption mechanism than Sb(V). This different sorption mechanism for Sb(V) and Sb(III) in the presence of iron has been reported in previous studies. Qi and Pichler³¹ evaluated the sorption mechanism of both antimony species on ferrihydrite, showing that Sb(V) does not bind strongly to iron oxide surface due to the combination of outer- and inner-sphere complexes. By contrast, Sb(III) is bound strongly by specific inner-sphere binding. Watkins et al.⁴⁸ propose that Sb(III) is directly bonded to one of the bridging oxygen from goethite and a six-membered ring can be formed by a hydrogen bond. Guo et al.⁴⁹ determined that Sb(III) and Sb(V) be adsorbed onto iron oxy-hydroxides by the formation of an inner-sphere surface complex. Therefore, there is controversy in Sb(V) sorption mechanism. Few studies have been made using SPION as iron oxide adsorbent. Kirsch et al.⁵⁰ propose an inner-sphere Sb surface complex with magnetite, including the Sb(V) reduction during the sorption process. Verbinnen et al.⁵¹ also confirm this sorption mechanism on zeolite-supported magnetite. As well as, Shan et al.⁵² propose an inner-sphere complex formed by Sb(III) and hematite modified magnetic nanoparticles.

In this work, it is observed that, in the presence of SPION, the adsorption of Sb(V) decreases with increasing pH (Figure 6.7), but not drastically as in the case of the sponge alone. This behaviour can be interpreted based on these three differentiated types of interaction⁴⁴ (Figure 6.22). In one hand, SPION exhibited large amounts of hydroxyl groups on the surface, which could act as hydrogen donor and form hydrogen bonding with the oxygen atom on the Sb(V) molecule. Furthermore, at pH below the pHzc (pH 9), SPION surface is positively charged and adsorbs negative adsorbate species [Sb(OH)₆⁻]. Thus, Sb(V) could be bounded by outer-sphere complex with positive surface charges (and hence the adsorption decreases if the pH increase). On the other hand, it could be bounded by inner-sphere complexation with iron included in SPION, as FTIR spectra indicate due to de Fe-O-Sb bonds formation. Due to that at pH below 9 the adsorption decrease is not as sharp as in the sponge, there are grounds for believing that the main mechanism of Sb(V) adsorption onto sponge+SPION is the inner-sphere complexation.

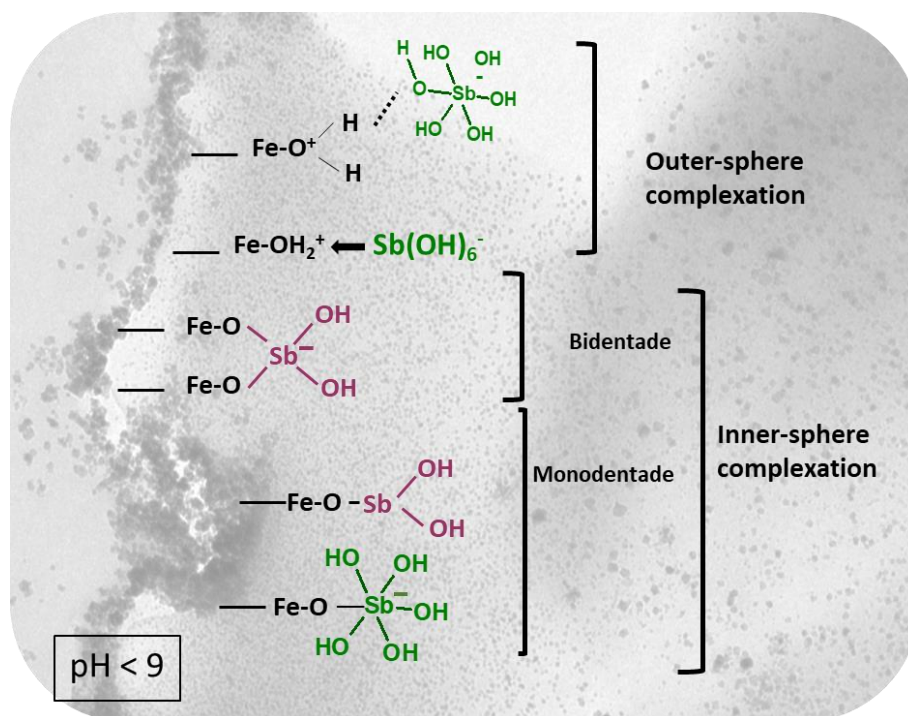


Figure 6.22. *Sb(III) and Sb(V) sorption suggested mechanism on the sponge+SPION system. Dashed line indicates hydrogen bonds and arrow indicate electrostatic interaction*

Sb(III) adsorption process is stable for a wide range of pH. XANES results confirm the observation obtained from FTIR analysis. The presence of SPION assists Sb(III) oxidation to Sb(V), and the adsorption capacity decreases at pH higher than 8, as the oxidation increases (Figure 6.7). Previous studies show that iron oxides such as goethite or ferrihydrite could oxidise Sb(III). Leuz et al.³⁴ propose the Sb(III) oxidation adsorbed in goethite in the presence of oxygen at pH 9.9. They suggest that Fe(III) could not be the oxidant because Fe(III) has a higher redox potential than Sb(III) only at acid or neutral pH, so Fe(III) would only be able to oxidise Sb(III) in acid media, which is not the case (oxidation has been shown at pH higher than 5.6). Watkins et al.⁴⁸ propose a Sb(III) sorption mechanism which involves the transfer of two electrons from Sb(III) to two Fe(III), producing the Sb(III) oxidation and the release of Sb(V) and Fe(II). Qi et al.³¹ show that oxygen alone could not be an oxidant for Sb(III), even in the presence of ferrihydrite can oxidise Sb(III) to Sb(V). This fact suggests that ferrihydrite surface acts as a catalyst in Sb(III) oxidation by dissolved oxygen. Adsorption and oxidation studies of Sb(III) on SPION, concretely on magnetite, are contradictories. While Kirsch et al.⁵⁰ show that reduction of Sb(V) to Sb(III) is possible in 22 h at basic pH. Verbinnen et al. prove that Sb(III) could be oxidised by dissolved oxygen but magnetite is not capable according to redox potential calculation. Also, Qi et al.⁵³ indicate that the presence of magnetite produce rather slight Sb(III) oxidation to Sb(V). No previous studies have been done using γ -Fe₂O₃ for Sb adsorption. Considering Sb similarities with As(III), or even with Se(IV), no oxidation-reduction processes are involved in Se(IV) adsorption onto maghemite^{54,55}.

Adsorption experiments show that Sb(III) interact with SPION forming bonds that are independent of the pH. FTIR and XANES measurements evidence that Sb(III) after adsorption on sponge+SPION is not present as tartrate complex. Also, FTIR confirms the presence of Fe-O-Sb bonds, and XANES results prove that Sb(III) is slightly oxidised in the presence of SPION at pH higher than 5.6. It stands to reason that Sb(III) is bounded to SPION strongly than Sb(V), forming an inner-sphere (monodentate or bidentate) complex (Figure 6.22) and the desorption process is produced by its oxidation, which is in concordance with adsorption experiments. Furthermore, information about the oxidant could not be inferred from the Fe K-edge XANES spectra due to the lower concentration of Sb in comparison with Fe, thus the adsorption of Sb on the surface of the nanoparticles does not influence the oxidation state of Fe enough to be detected.

5. CONCLUSIONS

In this Chapter, the Sb(III) and Sb(V) adsorption mechanism onto Metalzorb® and sponge+SPION system was investigated. Macroscopic characterisation of the adsorption process in Chapter 4 concluded that Sb(III) and Sb(V) adsorption to the bare sponge is performed involving weak interactions (as the isotherm, selectivity and desorption studies have shown) whereas, Sb(III) and Sb(V) present a higher affinity for sponge+SPION system and stronger interactions are formed. Microscopic adsorption characterisation (FTIR and XAS), performed in this chapter, confirms the results obtained in Chapter 4. The affinity of Sb(III) and Sb(V) toward the sponge and the sponge+SPION depends on the Sb speciation, the solution pH, and the proper characteristics of the SPION. Adsorption at different pHs, FTIR and XAS studies evidence that the sponge and sponge+SPION system are able to bind both antimonite (Sb(III)) and antimonate (Sb(V)) but with different affinity, and with different adsorption mechanisms. With a lower affinity, Sb(III) and Sb(V) are absorbed into the sponge through H-bonding and electrostatic interaction, which indicates the formation of outer-sphere complexes. The presence of SPION facilitates the formation of the Fe-O-Sb bonds, which participates on the Sb(III) and Sb(V) adsorption. For Sb(III), adsorption is independent of the pH, indicating that inner-sphere complexes are formed with a partial Sb(III) oxidation. On the contrary, Sb(V) adsorption depends on the pH, reducing its sorption capacity up to 40 % when the pH increases from 8 to 9. This pH dependency indicates that inner- and outer-sphere complexes are generated during Sb(V) adsorption.

6. REFERENCES

- (1) Rainer, N. B. Polymer Product for the Selective Absorption of Dissolved Ions. 5096946, 1992.
- (2) Muñoz, J. A.; Gonzalo, A.; Valiente, M. Arsenic Adsorption by Fe(III)-Loaded Open-Celled Cellulose Sponge. Thermodynamic and Selectivity Aspects. *Environ. Sci. Technol.* **2002**, *36* (15), 3405–3411.
- (3) Kitchener, J. A. Mechanisms of Adsorption from Aqueous Solutions: Some Basic Problems. *J. Photogr. Sci.* **1965**, *13* (3), 152–160.
- (4) Katz, L. E.; Hayes, K. F. Surface Complexation Modeling. I. Strategy for Modeling Monomer Complex Formation at Moderate Surface Coverage. *J. Colloid Interface Sci.* **1995**, *170*, 477–490.
- (5) Hiemstra, T.; Riemsdijk, W. H. Van; Conrad, R. Oxide – Solution Interfaces : Surface Structure and Ion Complexation. In *CRC Encyclopedia of Surface and Colloid Science, Third Edition*; 2015.
- (6) Rao, S. B. Oxide Materials for Water Treatment. *Encycl. Surf. Colloid Sci.* **2015**, 5115–5121.
- (7) Geckeis, H. Iron Oxide – Hydroxide Surfaces : Polyvalent Metal Ion Solid – Water Interface Reactions. *Encycl. Surf. Colloid Sci. Third Ed.* **2015**.
- (8) Kuan, W.-H.; Lo, S.-L.; Wang, M. K.; Lin, C.-F. Removal of Se(IV) and Se(VI) from Water by Aluminum-Oxide-Coated Sand. *Water Res.* **1998**, *32* (3), 915–923.
- (9) Rovira, M.; Giménez, J.; Martínez, M.; Martínez-Lladó, X.; de Pablo, J.; Martí, V.; Duro, L. Sorption of Selenium(IV) and Selenium(VI) onto Natural Iron Oxides: Goethite and Hematite. *J. Hazard. Mater.* **2008**, *150* (2), 279–284.
- (10) Zhu, M.; Northrup, P.; Shi, C.; Billinge, S. J. L.; Sparks, D. L.; Waychunas, G. A. Structure of Sulfate Adsorption Complexes on Ferrihydrite. *Environ. Sci. Technol. Lett.* **2014**, *1* (1), 97–101.
- (11) Liu, C. H.; Chuang, Y. H.; Chen, T. Y.; Tian, Y.; Li, H.; Wang, M. K.; Zhang, W. Mechanism of Arsenic Adsorption on Magnetite Nanoparticles from Water: Thermodynamic and Spectroscopic Studies. *Environ. Sci. Technol.* **2015**, *49* (13), 7726–7734.
- (12) Zhang, G.; Liu, F.; Liu, H.; Qu, J.; Liu, R. Respective Role of Fe and Mn Oxide Contents for Arsenic Sorption in Iron and Manganese Binary Oxide: An X-Ray Absorption Spectroscopy Investigation. *Environ. Sci. Technol.* **2014**.
- (13) Deng, R. J.; Jin, C. S.; Ren, B. Z.; Hou, B. L.; Hursthouse, A. S. The Potential for the Treatment of Antimony-Containing Wastewater by Iron-Based Adsorbents. *Water (Switzerland)* **2017**, *9* (10)..
- (14) Vithanage, M.; Rajapaksha, A. U.; Dou, X.; Bolan, N. S.; Yang, J. E.; Ok, Y. S. Surface Complexation Modeling and Spectroscopic Evidence of Antimony Adsorption on Iron-Oxide-Rich Red Earth Soils. *J. Colloid Interface Sci.* **2013**, *406*, 217–224.
- (15) Goldberg, S.; Criscenti, L. J.; Turner, D. R.; Davis, J. A.; Cantrell, K. J. Adsorption–Desorption Processes in Subsurface Reactive Transport Modeling. *Vadose Zo. J.* **2007**, *6* (3), 407.
- (16) McComb, K. A.; Craw, D.; McQuillan, A. J. ATR-IR Spectroscopic Study of Antimonate Adsorption to Iron Oxide. *Langmuir* **2007**, *23* (24), 12125–12130.
- (17) Pokrovski, G. S.; Borisova, A. Y.; Roux, J.; Hazemann, J.-L.; Petdang, A.; Tella, M.; Testemale, D. Antimony Speciation in Saline Hydrothermal Fluids: A Combined X-Ray Absorption Fine Structure Spectroscopy and Solubility Study. *Geochim. Cosmochim. Acta* **2006**, *70*, 4196–4214.
- (18) Fawcett, S. E.; Gordon, R. a.; Jamieson, H. E. Optimizing Experimental Design, Overcoming Challenges, and Gaining Valuable Information from the Sb K-Edge XANES Region. *Am. Mineral.* **2009**, *94* (10), 1377–1387.

- (19) Muñoz, J. A.; Gonzalo, A.; Valiente, M. Arsenic Adsorption by Fe(III)-Loaded Open-Celled Cellulose Sponge. Thermodynamic and Selectivity Aspects. *Environ. Sci. Technol.* **2002**, *36* (15), 3405–3411.
- (20) Amanda, A. Development of Polymeric Nanocomposites with Enhanced Distribution of Catalytically Active or Bactericide Nanoparticles. *PhD thesis UAB* **2012**.
- (21) Alain, M.; Jacques, M.; Diane, M.-B.; Karine, P. MAX: Multiplatform Applications for XAFS. *J. Phys. Conf. Ser.* **2009**, *190*.
- (22) Ravel, B.; Newville, M. ATHENA, ARTEMIS, HEPHAESTUS: Data Analysis for X-Ray Absorption Spectroscopy Using IFEFFIT. In *Journal of Synchrotron Radiation*; 2005.
- (23) Filella, M.; Belzile, N.; Chen, Y.-W. Antimony in the Environment: A Review Focused on Natural Waters II. *Earth-Science Rev.* **2002**, *59* (1–4), 265–285.
- (24) Nishad, P. A.; Bhaskarapillai, A.; Velmurugan, S. Towards Finding an Efficient Sorbent for Antimony: Comparative Investigations on Antimony Removal Properties of Potential Antimony Sorbents. *Int. J. Environ. Sci. Technol.* **2017**, *14* (4), 777–784.
- (25) Tella, M.; Pokrovski, G. S. Antimony(III) Complexing with O-Bearing Organic Ligands in Aqueous Solution: An X-Ray Absorption Fine Structure Spectroscopy and Solubility Study. *Geochim. Cosmochim. Acta* **2009**, *73* (2), 268–290.
- (26) Zheng, J.; Iijima, A.; Furuta, N. Complexation Effect of Antimony Compounds with Citric Acid and Its Application to the Speciation of Antimony(III) and Antimony(V) Using HPLC-ICP-MS. *J. Anal. At. Spectrom.* **2001**, *16* (8), 812–818.
- (27) Filella, M.; Williams, P. A. Antimony Biomethylation in Culture Media Revisited in the Light of Solubility and Chemical Speciation Considerations. *Environ. Toxicol.* **2010**, *25* (5), 429–532.
- (28) Ungureanu, G.; Santos, S. C. R.; Volf, I.; Boaventura, R. A. R.; Botelho, C. M. S. Biosorption of Antimony Oxyanions by Brown Seaweeds: Batch and Column Studies. *J. Environ. Chem. Eng.* **2017**, *5* (4), 3463–3471.
- (29) Puigdomenech, I. Medusa. Royal Institut of Technology, Stockholm 1999.
- (30) Morillo, D.; Pérez, G.; Valiente, M. Efficient Arsenic(V) and Arsenic(III) Removal from Acidic Solutions with Novel Forager Sponge-Loaded Superparamagnetic Iron Oxide Nanoparticles. *J. Colloid Interface Sci.* **2015**, *453*, 132–141.
- (31) Qi, P.; Pichler, T. Sequential and Simultaneous Adsorption of Sb(III) and Sb(V) on Ferrihydrite: Implications for Oxidation and Competition. *Chemosphere* **2016**, *145*, 55–60.
- (32) Vithanage, M.; Rajapaksha, A. U.; Ahmad, M.; Uchimiya, M.; Dou, X.; Alessi, D. S.; Ok, Y. S. Mechanisms of Antimony Adsorption onto Soybean Stover-Derived Biochar in Aqueous Solutions. *J. Environ. Manage.* **2015**, *151*, 443–449.
- (33) Hristovski, K. D.; Markovski, J. Engineering Metal (Hydr)Oxide Sorbents for Removal of Arsenate and Similar Weak-Acid Oxyanion Contaminants: A Critical Review with Emphasis on Factors Governing Sorption Processes. *Sci. Total Environ.* **2017**, *598*, 258–271.
- (34) Leuz, A. K.; Mönch, H.; Johnson, C. A. Sorption of Sb(III) and Sb(V) to Goethite: Influence on Sb(III) Oxidation and Mobilization. *Environ. Sci. Technol.* **2006**, *40* (23), 7277–7282.
- (35) The Council of the European Union. *Council Directive 98/83/EC of 3 November 1998 on the Quality of Water Intended for Human Consumption*; 1998; Vol. L330, pp 32–54.
- (36) Mishra, S.; Dwivedi, J.; Kumar, A.; Sankararamkrishnan, N. Removal of Antimonite (Sb(III)) and Antimonate (Sb(V)) Using Zerovalent Iron Decorated Functionalized Carbon Nanotubes. *RSC Adv.* **2016**, *6* (98), 95865–95878.

- (37) Vithanage, M.; Rajapaksha, A. U.; Ahmad, M.; Uchimiya, M.; Dou, X.; Alessi, D. S.; Ok, Y. S. Mechanisms of Antimony Adsorption onto Soybean Stover-Derived Biochar in Aqueous Solutions. *J. Environ. Manage.* **2015**, *151*, 443–449.
- (38) Maillo, J.; Pages, P.; Vallejo, E.; Lacorte, T.; Gacén, J. FTIR Spectroscopy Study of the Interaction between Fibre of Polyamide 6 and Iodine. *Eur. Polym. J.* **2005**, *41* (4), 753–759.
- (39) Reddy, J. R.; Ravi, G.; Suresh, P.; Veldurthi, N. K.; Velchuri, R.; Vithal, M. Antimony Potassium Tartrate: A Novel Single Source Precursor for the Preparation of Sb_2O_3 , KSb_3O_5 , $K_{0.51}Sb_{0.67}^{III}Sb_2^{V}O_{6.26}$, and $KSbO_3$. *J. Therm. Anal. Calorim.* **2014**, *115* (2), 1321–1327.
- (40) Mazali, I. O.; Las, W. C.; Cilense, M. Synthesis and Characterization of Antimony Tartrate for Ceramic Precursors. *J. Mater. Synth. Process.* **1999**, *7* (6), 387–391.
- (41) Mishra, S.; Dwivedi, J.; Kumar, A.; Sankararamkrishnan, N. Removal of Antimonite (Sb(III)) and Antimonate (Sb(V)) Using Zerovalent Iron Decorated Functionalized Carbon Nanotubes. *RSC Adv.* **2016**, *6* (98), 95865–95878.
- (42) Lan, B.; Wang, Y.; Wang, X.; Zhou, X.; Kang, Y.; Li, L. Aqueous Arsenic (As) and Antimony (Sb) Removal by Potassium Ferrate. *Chem. Eng. J.* **2016**, *292*, 389–397.
- (43) Drátovský, M.; Karlicek, J. Lithium and Sodium Antimonates. *Chem. zvesti* **1981**, *35* (5), 629–640.
- (44) Wang, L.; Wang, J.; Wang, Z.; He, C.; Lyu, W.; Yan, W.; Yang, L. Enhanced Antimonate (Sb(V)) Removal from Aqueous Solution by La-Doped Magnetic Biochars. *Chem. Eng. J.* **2018**, *354* (August), 623–632.
- (45) Xu, W.; Wang, H.; Liu, R.; Zhao, X.; Qu, J. The Mechanism of Antimony(III) Removal and Its Reactions on the Surfaces of Fe-Mn Binary Oxide. *J. Colloid Interface Sci.* **2011**, *363*, 320–326.
- (46) Zhao, X.; Dou, X.; Mohan, D.; Pittman, C. U.; Ok, Y. S.; Jin, X. Antimonate and Antimonite Adsorption by a Polyvinyl Alcohol-Stabilized Granular Adsorbent Containing Nanoscale Zero-Valent Iron. *Chem. Eng. J.* **2014**, *247*, 250–257.
- (47) Tella, M.; Pokrovski, G. S. Stability and Structure of Pentavalent Antimony Complexes with Aqueous Organic Ligands. *Chem. Geol.* **2012**, *292–293*, 57–68.
- (48) Watkins, R.; Weiss, D.; Dubbin, W.; Peel, K.; Coles, B.; Arnold, T. Investigations into the Kinetics and Thermodynamics of Sb(III) Adsorption on Goethite (α -FeOOH). *J. Colloid Interface Sci.* **2006**, *303* (2), 639–646.
- (49) Guo, X.; Wu, Z.; He, M.; Meng, X.; Jin, X.; Qiu, N.; Zhang, J. Adsorption of Antimony onto Iron Oxyhydroxides: Adsorption Behavior and Surface Structure. *J. Hazard. Mater.* **2014**, *276*, 339–345.
- (50) Kirsch, R.; Scheinost, A. C.; Rossberg, A.; Banerjee, D.; Charlet, L. Reduction of Antimony by Nano-Particulate Magnetite and Mackinawite. *Mineral. Mag.* **2008**, *72* (1), 185–189.
- (51) Verbinnen, B.; Block, C.; Lievens, P.; Van Brecht, A.; Vandecasteele, C. Simultaneous Removal of Molybdenum, Antimony and Selenium Oxyanions from Wastewater by Adsorption on Supported Magnetite. *Waste and Biomass Valorization* **2013**, *4* (3), 635–645.
- (52) Shan, C.; Ma, Z.; Tong, M. Efficient Removal of Trace Antimony(III) through Adsorption by Hematite Modified Magnetic Nanoparticles. *J. Hazard. Mater.* **2014**, *268*, 229–236.
- (53) Qi, Z.; Lan, H.; Joshi, T. P.; Liu, R.; Liu, H.; Qu, J. Enhanced Oxidative and Adsorptive Capability towards Antimony by Copper-Doping into Magnetite Magnetic Particles. *RSC Adv.* **2016**, *6* (71), 66990–67001.
- (54) Auffan, M.; Rose, J.; Proux, O.; Borschneck, D.; Masion, A.; Chaurand, P.; Hazemann, J. L.; Chaneac, C.; Jolivet, J. P.; Wiesner, M. R.; et al. Enhanced Adsorption of Arsenic onto Maghemite Nanoparticles: As(III) as a Probe of the Surface Structure and Heterogeneity. *Langmuir* **2008**, *24* (7), 3215–3222.

- (55) Jordan, N.; Ritter, A.; Scheinost, A. C.; Weiss, S.; Schild, D.; Hübner, R. Selenium(IV) Uptake by Maghemite (γ -Fe₂O₃). *Environ. Sci. Technol.* **2014**, *48* (3), 1665–1674. <https://doi.org/10.1021/es4045852>.
- (56) Iyer, R. K.; Desphande, S. G.; Rao, G. S. Studies on Complexes of Tartaric Acid -I. Antimony (III)-Tartaric Acid System. *J. Inorg. Nucl. Chem.* **1972**, *34*, 3351–3356.
- (57) Hao, H.; Liu, G.; Wang, Y.; Shi, B.; Han, K.; Zhuang, Y.; Kong, Y. Simultaneous Cationic Cu(II)–anionic Sb(III) Removal by NH₂-Fe₃O₄-NTA Core-Shell Magnetic Nanoparticle Sorbents Synthesized via a Facile One-Pot Approach. *J. Hazard. Mater.* **2019**, *362* (August 2018), 246–257. <https://doi.org/10.1016/j.jhazmat.2018.08.096>.

CONCLUSIONS

CHAPTER 7

GENERAL CONCLUSIONS

1. CONCLUSIONS.....	231
Chapter 2. Electrochemical regeneration for arsenic removal.	231
Chapter 3. Antimony environmental significance pollution and removal techniques	232
Chapter 4. Optimisation and characterisation of superparamagnetic iron oxide (SPION) adsorbent for antimony removal	233
Chapter 5. Characterisation of Sb(III) and Sb(V) sorption process on the sponge and sponge+spion system.....	234
Chapter 6. Spectroscopic study of the adsorption mechanism of Sb(III) and Sb(V) on Sponge-SPION-direct system	236
2. FUTURE PERSPECTIVES	237

1. CONCLUSIONS

Considering the general objectives of the present study, and the specific objectives included in the different chapters, the results obtained in this work involve the development of a method to remove and recover oxyanions from polluted water by adsorption process, and the regeneration and reuse of the adsorbent. Specifically, the methods concern with antimony removal from aqueous solution (**Part 2**) and with the adsorbent regeneration loaded with arsenic (**Part 1**). Polymeric (sponge) and polymeric-nanostructured materials (sponge+SPION system) have been implemented as adsorbent materials, being SuperParamagnetic Iron Oxide Nanoparticles (SPION) the active adsorption sites on the last material. Various synthetic pathways for the nanostructure materials have been proved, studying its properties and characterisation to understand how the nanoparticles are attached to the polymeric material and how this fact can influence in the Sb adsorption (**Chapter 4**). Regarding Sb removal (**Chapter 3**), the influence of the pH, contact time, initial concentration, and temperature have been investigated, as well as, the influence of interfering ions (**Chapter 5**). These results, besides the chemical desorption and spectroscopy studies, allow determining the Sb, as Sb(III) and Sb(V), adsorption mechanism to the different adsorbents (**Chapter 6**). Concerning to the adsorbent regeneration (**Chapter 2**) when it is loaded with As, the influence of the applied current, the electrolyte and electrolyte concentration and the electrode material have been checked to determine that an Sn chemical species is needed for a successfully As desorption and remove from the solution.

The conclusion obtained during this PhD thesis is included in each chapter, although they are summarised below.

Chapter 2. Electrochemical regeneration for arsenic removal

Under patent protection

Chapter 3. Antimony environmental significance pollution and removal techniques

Due to its scarcity, toxicity and the effects which produce on human health, Sb has been considered as Critical Raw material, and as a pollutant of priority interest, thus its removal and recovery from drinking water are compulsory.

Despite the challenges mentioned above, adsorption treatment has emerged as “the best treatment” practice for Sb-wastewater due to its advantages such as low cost, simplicity, flexibility and the possibility for Sb recovery and the reuse of the adsorbent. The

adsorption process can competently reduce the total effluent content of antimony while allowing for lower operating costs and easier operation.

Among the different materials used as adsorbents, iron oxides are promising materials due to their high affinity for Sb and their excellent properties for the adsorption process. In Chapter 4, iron oxides properties and characteristics will be discussed, especially for superparamagnetic iron oxide nanoparticles. In this concern, a critical fact is the nanoparticles handling for both separations from treated liquor and to avoid nanoparticles aggregation. To overcome both barriers, the use of special nanoparticles support has been proposed that also offers excellent properties to minimise the diffusion barriers that limits the adsorption dynamics.

Chapter 4. Optimisation and characterisation of superparamagnetic iron oxide (SPION) adsorbent for antimony removal

Under patent protection

Chapter 5. Characterisation of Sb(III) and Sb(V) sorption process on the sponge and sponge+spion system

Under patent protection

Chapter 6. Spectroscopic study of the adsorption mechanism of Sb(III) and Sb(V) on Sponge-SPION-direct system

In this Chapter, the Sb(III) and Sb(V) adsorption mechanism onto Metalzorb® and sponge+SPION system was investigated. Macroscopic characterisation of the adsorption process in Chapter 4 concluded that Sb(III) and Sb(V) adsorption to the bare sponge is performed involving weak interactions (as the isotherm, selectivity and desorption studies have shown) whereas, Sb(III) and Sb(V) present a higher affinity for sponge+SPION system and stronger interactions are formed. Microscopic adsorption characterisation (FTIR and XAS), performed in this chapter, confirms the results obtained in Chapter 4. The affinity of Sb(III) and Sb(V) toward the sponge and the sponge+SPION depends on the Sb speciation, the solution pH, and the proper characteristics of the SPION. Adsorption at different pHs, FTIR and XAS studies evidence that the sponge and sponge+SPION system are able to bind both antimonite

(Sb(III)) and antimonate (Sb(V)) but with different affinity, and with different adsorption mechanisms. With a lower affinity, Sb(III) and Sb(V) are absorbed into the sponge through H-bonding and electrostatic interaction, which indicates the formation of outer-sphere complexes. The presence of SPION facilitates the formation of the Fe-O-Sb bonds, which participates on the Sb(III) and Sb(V) adsorption. For Sb(III), adsorption is independent of the pH, indicating that inner-sphere complexes are formed with a partial Sb(III) oxidation. On the contrary, Sb(V) adsorption depends on the pH, reducing its sorption capacity up to 40 % when the pH increases from 8 to 9. This pH dependency indicates that inner- and outer-sphere complexes are generated during Sb(V) adsorption.

2. FUTURE PERSPECTIVES

Taking into account the results described, the following aspects can be considered for future research and development purposes.

Regarding the As desorption system, additional studies are needed to identify an electrolyte which does not desorb the As from the sponge and allow to perform the proof of concept by producing the As(V) reduction to As(III) and the related desorption from the sponge to allow the reuse of the adsorbent.

About the sponge+SPION synthesis, further studies are needed in order to obtain a more homogeneous nanoparticles size distribution, and more nanoparticles concentration in the sponge matrix, improving the nanoparticles diffusion. Also, the synthesis pathway, which presents the best results for Sb adsorption should be tested using the supporting material in a different mode (bigger pieces of the material).

It is necessary to test this material with real wastewater containing Sb to check the feasibility and the behaviour of the material in a real application. Furthermore, it is interesting to use this adsorbent system in a continuous mode, studying its maximum adsorption capacity and its useful life.

On the other hand, it is well known that removal of arsenic, antimony and bismuth impurities from copper electrolytes is a primary target in copper electrorefineries. In this concern, the actual results on arsenic and antimony could be investigated on applications to such electrolytes.

To improve the adsorbent system, modifying SPION surface or supporting a different kind of nanoparticles on the sponge will be an option to obtain a selective adsorbent for Sb removal. In addition, it is necessary to look for a desorption system which allows specific recovering of Sb adsorbed to the target adsorbent, avoiding the desorption of other pollutants that can be simultaneously adsorbed.

Another interesting point of view will be to study the Sb-Fe formed in the adsorption process and its uses as a catalyst or as an anode in Na or Li-ion batteries. Deeper studies are needed regarding the Sb adsorption mechanism. Thus, it is necessary to characterise Sb as discrete precipitated compound or as insoluble polymer onto the sponge at high initial concentration and when it is adsorbed on the sponge+SPION system should be confirmed the related speciation.

ANNEXES

Annexe 1. INSTRUMENTAL TECHNIQUES

Introduction

The detailed characterisation of the different adsorbent systems and the precipitate formed during the adsorption-desorption process is essential for the appropriate development of such new material and adsorption-desorption methods. It allows a better understanding of the main features of their synthesis, explaining their properties, and determining areas for their potential application. Several widely used techniques are applicable to the characterisation of nanomaterials and the main parameter that usually characterise them include composition, size and distribution of nanoparticles, nanomaterials morphology, and special properties (i.e., magnetism).

Additionally, liquid phases containing the target compound to be removed must be characterised to determine the main parameters providing the adsorption capacity of the new materials that are being tested.

The techniques indicated below have been used in this work for the characterisation and analytic purposes.

Analytical techniques

Inductively Coupled Plasma Mass Spectrometry, ICP-MS

ICP-MS technique was employed to analyse the metal content in the liquid phases in all the adsorption experiments when varying several adsorption parameters. These parameters include antimony and arsenic as the target species under the adsorption process and other metal ions (i.e., zinc, nickel or iron), either in experiments where the stability control of SPION is checked or either in experiments where the adsorption selectivity was evaluated. Equipment description is specified in Table a1.1 and the ICP-MS equipment scheme is presented in Figure a1.1.

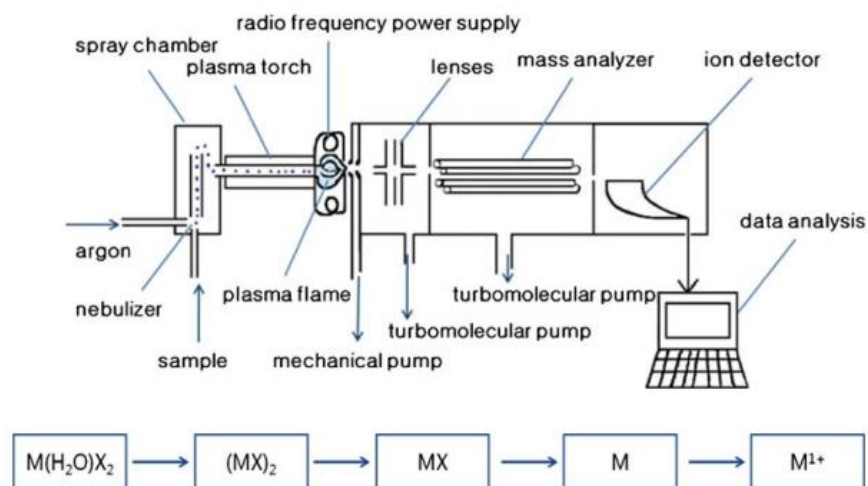

Figure a1.1. ICP-MS scheme¹

Table a1.1. ICP-MS equipment used in present studies

Equipment	ICP-MS
Model	VG Plasma Quad ExCell and XSeries 2
Company and Country	Thermo Scientific, UK
Laboratory of analysis	Centre Grup de Tècniques de Separació en Química, GTS (UAB, Barcelona, Spain)
Image	

In an ICP-MS, the sample, which usually should be in a liquid form, is pumped at 1 mL/min, usually with a peristaltic pump into a nebuliser, where it is converted into a fine aerosol with argon gas at about 1 L/min. The fine droplets of the aerosol, which represent only 1–2% of the sample, are separated from larger droplets using a spray chamber. The fine aerosol then emerges from the exit tube of the spray chamber and is transported into the plasma torch via a sample injector.

The plasma is formed by the interaction of an intense magnetical field (produced by radiofrequency passing through a copper coil) on a tangential flow of Argon, at about 15 L/min flowing through a concentric quartz tube (torch). This has the effect of ionising the gas and when seeded with a source of electrons from a high-voltage spark, forms a very-high-temperature plasma discharge (approx 10,000 K) at the open end of the tube. The plasma torch, which is positioned horizontally in the VG Plasma Quad equipment, is used to generate positively charged ions. It is the production and the detection of large quantities of these ions that give ICP-MS its characteristic low parts per trillion (ppt) detection capability.

Once the ions are produced in the plasma, they are directed into the mass spectrometer via the interface region, which is maintained at a vacuum of 1–2 Torr with a mechanical roughing pump. This interface region consists of two metallic cones (usually nickel), called the sampler and the skimmer cones, each with a small orifice (0.6–1.2 mm) to allow the ions to pass through to the ion optics, where they are guided into the mass separation device.

Once the ions have been successfully extracted from the interface region, they are directed into the main vacuum chamber by a series of electrostatic lens, called ion optics. The operating vacuum in this region is maintained at about 10^{-3} Torr with a turbomolecular pump. The main function of the optical region is to electrostatically focus the ion beam toward the mass separation device while stopping photons, particulates, and neutral species from reaching the detector. The ion beam containing all the analytes and matrix ions exits the ion optics and now passes into the heart of the mass spectrometer—the mass separation device, which is kept at an operating vacuum of approximately 10^{-6} Torr with a second turbomolecular pump. The mass separation device allows analyte ions of a particular mass-to-charge ratio through to the detector and to filter out all the non-analyte, interfering, and matrix ions.

The final process is to convert the ions into an electrical signal with an ion detector. When the ions emerge from the mass filter, they impinge on the first dynode and are converted into electrons. As the electrons are attracted to the next dynode, electron multiplication takes place, which results in a very high stream of electrons emerging from the final dynode. This electronic signal is then processed by the data handling system conventionally and then converted into analyte concentration using ICP-MS calibration standards.

Experimental conditions

Table a1.2. ICP-MS experimental conditions

Parameters	Conditions
<i>Nebuliser Gas Flow</i>	0.9 mL/min
<i>ICP-MS configuration</i>	Collision Cell ICP-MS (CCT)
<i>Forward Plasma Power</i>	1400 W
<i>Data Acquisition</i>	Mode transient Time Resolved Acquisition (TRA)
<i>Monitored Masses</i>	^{121}Sb , ^{75}As
<i>Dwell Times (mass-specific)</i>	50 ms
<i>Run Duration</i>	6
<i>Detection Limit</i>	300 ppt

Colorimetric technique UV-Vis Spectrophotometer

UV-Vis spectrophotometer (Figure a1.2) is a device in which light is coming from a continuous source pass through a monochromator, which selects a narrow band of wavelengths of the incident beam². This monochromatic light goes through a cuvette in which the sample is and measured the radiant power of light that emerges. The amount of absorbed radiation is related to the Lambert-Beer law (equation a1.1)³.

$$A = \varepsilon \cdot b \cdot C \quad (a1.1)$$

where A is the absorbance, ε (L/mol·cm) is the wavelength-dependent molar absorptivity coefficient, b (cm) is the cuvette length and C (mol/L) the concentration.

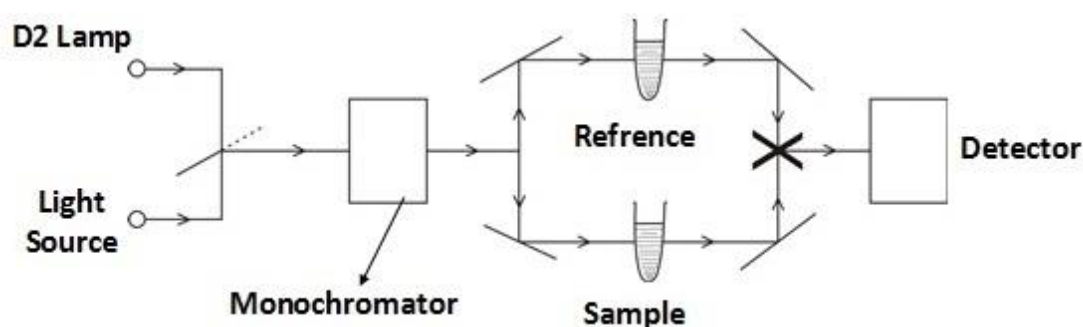



Figure a1.2. UV-Vis spectrophotometer scheme

In a double beam spectrophotometer, the light passes through the sample cuvette and the reference cuvette alternately (as shown in Figure a1.2). Comparing repeatedly both energies, the double beam device can correct some error associated with the intensity of the source and with the detector⁴. The UV-Visible equipment description is specified in Table a1.3.


Table a1.3. UV-Vis equipment used in present studies

Equipment	UV-vis
<i>Models</i>	UV-2 200 UV-Vis double-beam spectrophotometer
<i>Company and Country</i>	UNICAM, USA
<i>Laboratory of analysis</i>	Grup the Tècniques de Separació en Química. GTS (UAB, Barcelona, SPAIN) Cantabria University (Santander, SPAIN)
<i>Image</i>	

Field Portable X-Ray Fluorescence, FP-XRF

For the direct determination of the presence of arsenic and its total concentration FP-XRF technique is used. Equipment description is specified in Table a1.4.

Table a1.4. *FP-XRF equipment employed in XRF analysis*

Equipment	FP-XRF
<i>Models</i>	FP-XRF ALPHA 6500R
<i>Company and Country</i>	Innov-X System, USA
<i>Laboratory of analysis</i>	Grup the Tècniques de Separació en Química. GTS (UAB, Barcelona, SPAIN)
<i>Image</i>	

The analysing time for each sample was set to 120 s for the heavy elements and 90 s for the light elements. This period is established as the best tradeoff between accuracy and speed of analysis. For accuracy, an instrument blank and calibration verification check (NIST 2710) were done each working day before and after analysis. Such controls must be conducted once every twenty samples following EPA Method 6200.

A blank is used to verify the absence of contamination in both the spectrometer and the probe window. In our case, silicon dioxide samples are employed as a blank following the one used in EPA Method 6200 described before, although there are other alternatives as polytetrafluoroethylene (PFTE) block, a quartz block, 'clean' sand, or lithium carbonate. An instrument blank should also be analysed whenever the analyst suspects contamination.

A calibration verification check sample is used to examine the accuracy of the instrument and to assess the stability and consistency of the analysis for the target analytes.

Characterisation techniques

Transmission Electron Microscopy, TEM

TEM technique was employed to characterise the morphology of the SPION and their particle size distribution. These microscopes are also equipped for X-Ray diffraction techniques that allow characterising the crystalline structure of the SPION nanoparticles by diffraction patterns. Equipment description is specified in Table a1.5.

Table a1.5. TEM equipment used in present studies

Equipment	TEM
<i>Models</i>	JEOL JEM-2011, JOEL JEM-1400
<i>Company and Country</i>	Jeol Ltd., Japan
<i>Laboratory of analysis</i>	Servei de microscopía (UAB, Barcelona)

Image



Sample preparation

SPION: SPION is dispersed in ethanol by sonication and a Cu-grid, used as a support for TEM samples, is immerse in SPION suspension twice to the deposit of the nanoparticles on it. Then, the solvent evaporation on the Cu-grid is carried out at room temperature.

Sponge+SPION system: Samples are embedded in an epoxy resin and cross-sectioned with a Leica EM UC6 ultramicrotome using a 35° diamond knife from Diatome to obtain thin layer containing the material. This thin layer is placed on a Cu-grid.

Particle size distribution

By the digital treatment of TEM images, it is possible to produce size histograms from the sample data. The measurements of the diameter of a representative number of NP is needed and was obtained by a measuring tool ImageJ software⁵, and the related histograms were represented by Originlab software. The frequency (in %) of the NP size

is generally described by corresponding Amp Gaussian equation of four parameters (Equation a1.2), where D_{TEM} is the centre peak position (corresponding to the most frequent diameter), A is the area of the curve's peak, σ is the width of the peak, indicating sample polydispersity and D is NPs size^{6,7}.

$$y = Ae^{-\frac{(D-D_{TEM})^2}{2\sigma^2}} \quad (a1.2)$$

Basic TEM fundamentals

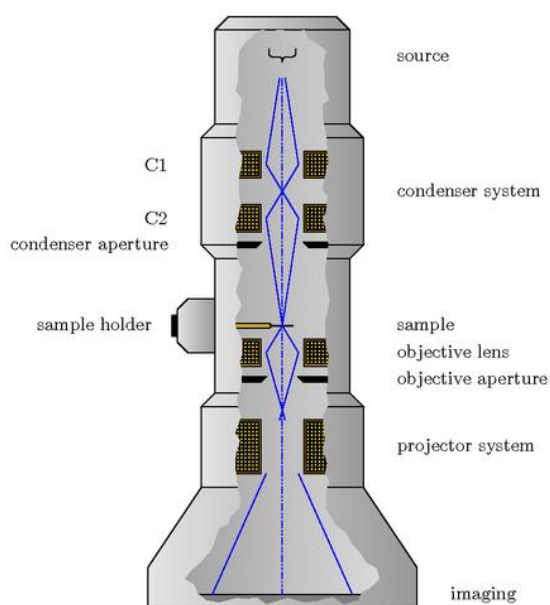


Figure a1.3. TEM scheme

TEM operates on the same basic principles as the light microscope but uses electrons instead of light. Because the wavelength of electrons is much smaller than that of light, the optimal resolution attainable for TEM images is many orders of magnitude better than that from a light microscope. It is based on the generation of a high energy electrons beam (100-200keV) which is focused through a very thin sample interacting with it. Certain parts of the irradiated beam are transmitted through the sample creating the TEM image by the elastic and inelastic scattered electrons that traverse the sample (Figure a1.3). The interactions between

the electrons and the atoms of the sample give the structural features of the material of analysis. The instrument requires to work under vacuum conditions, and the sample must be thin enough to transmit sufficient electrons to form an image with minimum energy loss.

Scanning Electron Microscopy, SEM, and Energy Dispersive X-ray Spectrometer, EDS or EDX

SEM technique is employed to study the morphology of the adsorbent systems surface. Coupled to SEM, EDS/EDX provides the elemental chemical composition of the samples based on the X-Ray emitted by specific atoms which have been interacted with a particular electron beam. Each atom has a unique X-Ray spectrum. Thus the elemental composition can be obtained by detected radiation. Equipment description is specified in Table a1.6.

Table a1.6. SEM equipment used in present studies

Equipment	SEM
<i>Models</i>	MERLIN FE-SEM + Detector EDS Oxford LINCA X-Max FEI Quanta 650FEG ESEM + EDS Inca 250 SSD XMax20 detector
<i>Company and Country</i>	Carl Zeiss Microscopy, LLC., Germany
<i>Laboratory of analysis</i>	Servei de microscopía (UAB, Barcelona) Servei de microscopía (ICN2, Barcelona)

Image



Sample preparation

A double-sided carbon tape sticker is attached to an aluminium stub where a small amount of sample is placed. Bare sponge due to its non-conductive properties needs to be coated by a thin layer, in this case, a platinum layer using a sputter coater.

Basic SEM fundamentals

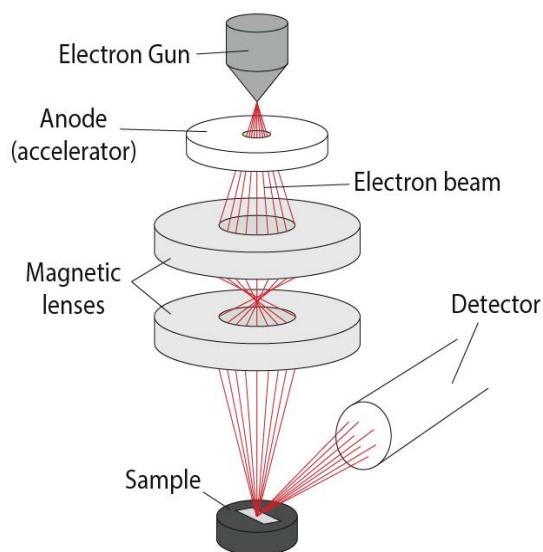


Figure a1.4. SEM scheme

SEM images are obtained by the signal produced from the electron beam and specimen interactions, by scanning an electron probe across the surface and monitoring the secondary electrons emitted (Figure a1.4). Those are produced when an incident electron excites an electron in the sample giving some of its energy in the process, resulting in the emission of these secondary electrons. Then, these are collected by a detector and converted to an image^{8,9}. An ultra-high vacuum system is indispensable for SEMs in order to avoid the scattering on the electron beam and the contamination of the electron guns and other components^{8,9}.

X-Ray Diffraction, XRD

The determination of SPION crystallographic phase is also undertaken by X-Ray powder diffraction (XRD). In a diffraction pattern, the location of the peaks on the 2θ scale can be compared to reference peaks. Furthermore, the crystallographic phase of the precipitate formed during the arsenic reduction is studied using this technique. Equipment description is specified in Table a1.7.

Table a1.7. XRD equipment employed in present studies

Equipment	XRD
Models	X'Pert-MPD X-ray Diffraction System
Company and Country	Philips, Netherlands
Laboratory of analysis	Servei Difracció Raigs X (UAB, Barcelona, Spain)

Image



Sample preparation

For the analysis, samples in powder form were deposited in a metallic sample holder. Diffraction patterns are collected by a monochromatized X-ray beam with nickel-filtered Cu(K α) radiation with a wavelength of 0.154021 nm in similar conditions that already reported in the literature¹⁰. In Table a1.8, experimental conditions during the XRD spectra acquisition are described.

Table a1.8. Experimental conditions during XRD spectra acquisition

Parameter	Conditions
Monochromatic Beam	Cu K α
Wavelength (nm)	0.154021
2θ (°)	5 – 80 or 15 - 90
Step size (°)	0.026
Time of step (s)	0.3

Basic XRD fundamentals

XRD monitors the diffraction of X-rays after they interact with the electrons in the atoms of the sample; the X-rays are reflected, and in most cases, the waves interfere between them being cancelled. However, when a regular crystalline sample is concerned, a proportion of waves are reinforced, forming a constructive interference which is known as diffraction. Such diffraction holds information about the electron distribution in the material producing a characteristic pattern⁹ of the crystal structure and only occurs when incident angles fulfil the Bragg condition represented in Eq. a1.3.⁹

$$n \lambda = 2 d \sin \theta \quad \text{a1.3}$$

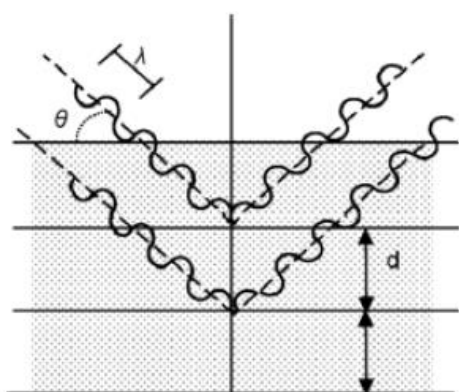


Figure a1.5. Representation of condition for constructive interference

By varying the angle θ , the Bragg Law condition is satisfied for different d-spacing in polycrystalline materials (Figure a1.5.). Plotting the angular positions versus intensities produces a diffraction pattern, which is characteristic of the sample. When a mixture of different phases is present, the resultant diffractogram is a superposition of the individual patterns⁹.

In a typical XRD pattern, the diffracted intensities are plotted versus the detector angle 2θ . Then, the crystal phases may be identified by comparison of the obtained patterns

with those of reference, found in internationally recognised databases (such as Joint Committee on Powder Diffraction Standards database – JCPDS).

A useful phenomenon is that as crystallite dimensions enter the nanoscale, the peaks broaden with decreasing crystal size. The widths of the diffraction peaks allow the determination of crystalline size, by using variants of the Scherrer equation⁹ (Eq. a1.4):


$$t = \frac{K \lambda}{B \cos \theta} \quad \text{a1.4}$$

where t is the thickness of the crystal, K is the Scherrer constant which depends on the crystallite shape, λ is the radiation wavelength used to obtain the diffractogram and B is the full width at half maximum of the broadened peak. If a Gaussian function is used to describe the broadened peak, then the Scherrer's constant K is equal to 0.89. The Scherrer equation is derived from Bragg's law and may be used to determine crystallite sizes if the crystals are smaller than 1000\AA .

Superconducting Quantum Interference Device, SQUID

Magnetic susceptibility of SPION and sponge+SPION system is characterised by SQUID. It is one of the most sensitive methods to measure magnetisation. It is made in a magnetic field range from -50 to 50 KOe, to measure extremely weak magnetic fields based on superconducting loops. The knowledge of the magnetic susceptibility will mark the required magnetic field to remove the SPION from the treated solution easily. Equipment description is specified in Table a1.9.

Table a1.9. SQUID equipment employed in present studies

Equipment	SQUID
<i>Models</i>	MPMS-2 SQUID
<i>Company and Country</i>	Quantum Design, USA
<i>Laboratory of analysis</i>	ICMAB (Barcelona, Spain)
<i>Image</i>	

Sample preparation

Different quantities of sample, depending on their SPION concentration, are accurately introduced in suitable test tubs and the magnetization is analysed at 300 K. The magnetic properties of the nanocomposites were represented by plotting the magnetic moment (normalised by the amount of magnetic component in the sample) versus the applied magnetising field (H), emu/g vs Oesterds (Oe) in cgs units (table a1.10))^{11,12}. Table a1.10 summarizes the quantities and units used in magnetism measurements.

Table a1.10. Table of quantities and units used in magnetism

Quantity	Symbol	SI unit	Cgs unit
Length		10^{-2} m	1 cm
Mass	M	10^{-3} kg	1 g
Force	F	10^{-5} N	1 dyne
Energy	E	10^{-7} J	1 erg
Magnetic induction	B	10^{-4} T	1 G
Magnetic Field Strength	H	$10^3/4\pi$ A/m	1 Oe
Magnetic moment	μ	10^{-3} J/T or Am ²	1 erg/G or emu
Magnetization	M	10^3 A/m or J/Tm ³	1 Oe or emu/cm ³
Magnetic susceptibility	χ	4π	1emu/cm ³ or emu/cm ³ Oe
Molar susceptibility	χ_m	$4\pi \cdot 10^{-6}$ m ³ /mol	1emu/mol or emu/mol Oe
Mass susceptibility	χ_g	$4\pi \cdot 10^{-3}$ m ³ /kg	1 emu/g or emu/g Oe
Magnetic flux	ϕ	10^{-8} Tm ² or Wb	1 G cm ² or Mx
Demagnetization factor	N	$0 < N < 1$	$0 < N < 4\pi$

Basic SQUID fundamentals

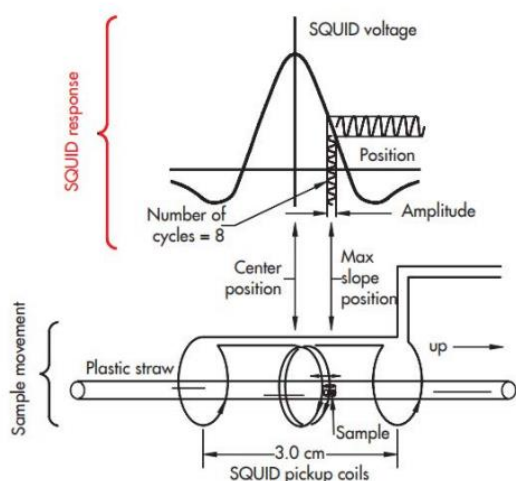



Figure a1.6. Schematics of SQUID magnetometer with longitudinal pickup coils.

SQUID is mounted in a magnetometer with a sensor consisting of a superconducting ring with one or more Josephson junctions that act as resistive barriers that separate superconducting regions. The sensor is connected to a pickup coil with four windings (Figure a1.6). When the sample is moved up and down, it produces an alternating magnetic flux in the pick-up coil which leads to a small alternating output voltage when transferred to a flux-to-voltage converter. This voltage is then amplified and read out as a voltage that is proportional to the magnetic moment of the sample.

Fourier Transform Infrared spectroscopy, FTIR

FTIR spectrum of the sponge and sponge+SPION-direct system were measured to identify the functional groups present on both materials surface. This information is useful to understand the binding sites of SPION on the surface of the sponge. Besides, some insight into the iron phase in the SPION can be obtained. Furthermore, the functional groups involved in Sb adsorption are identified. Equipment description is specified in a1.11.

Table a1.11. FTIR employed in the study

Equipment	FTIR
<i>Models</i>	Vertex70 spectrometer (TE Cooled DLaTGS Detector with KBr windows)
<i>Company and Country</i>	Bruker
<i>Laboratory of analysis</i>	MIRAS beamline (ALBA synchrotron, Barcelona, Spain)
<i>Image</i>	

Sample preparation

Samples for FTIR determination were ground with special grade KBr in an agate mortar, by mixing a fixed amount of sample (1% w/w) in KBr which was used to prepare the pellet. The analysis is carried out at 4000-350 cm^{-1} wavelength range in transmittance mode and 256 scans per sample.

Basic FTIR fundamentals

IR spectrum takes place due to linked atoms' frequency vibration are inside the infrared region. These energy changes are produced by transitions between different energy levels of vibrational and/or rotational states of the different atomic groups. Each atomic group or molecule has a characteristic absorption spectrum, and it is a composition of different absorption bands, each one due to a certain type of bond (characterised by the bonding strength and the atoms that form it) and its vibration way¹³ (Figure a1.7).

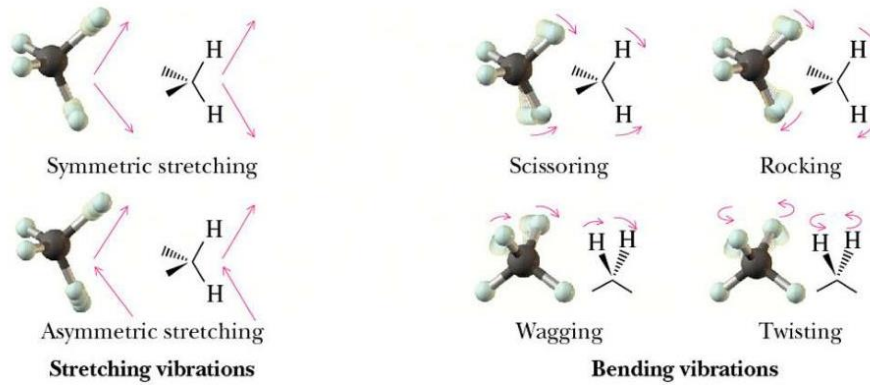


Figure a1.7. Different bonds vibrations modes

If vibration is recorded in the spectrum, there must be changes on the net molecular dipole moment. The frequency at which each vibration appears is inversely proportional to the reduced mass of the atoms that form it and directly proportional to the strength of the bond¹⁴. The energies to which the most common bonds of the molecules tend to appear are shown in Figure a1.8.

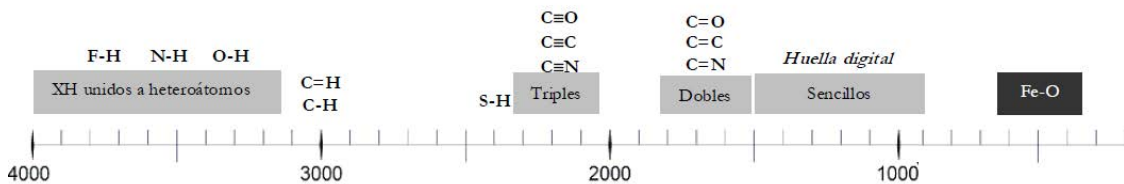



Figure a1.8. More vibrations of the more commons atoms groups (modified from Roca et al.¹⁵)

Thermogravimetric Analysis, TGA

Thermograms are carried out to determine the polymer degradation temperatures in composite materials. The process is accomplished by heating the samples with a heating range of 10°C/min until 900°C under N₂ atmosphere (60 mL/min). The weight loss percentage versus temperature is represented^{16,17}. The equipment description is specified in Table a1.12.

Table a1.12. TGA employed in the study

Equipment	TGA
<i>Model</i>	Q500 TGA
<i>Company and Country</i>	TA Instruments (New Castle, USA)
<i>Laboratory analysis</i>	Università degli Studi di Udine
<i>Image</i>	

Basic TGA fundamentals

Thermogravimetry (TGA) is a technique based on the variation in a sample mass (gain or loss) when subjected to heat treatment as a function of temperature and/or time^{18,19}. Three modes of TGA are commonly used; (1) isothermal TGA (Figure a1.9-A); where the variations in the sample mass are recorded as a function of time at constant temperature, (2) quasi-isothermal TGA (Figure a1.9- B); in which the sample is heated to constant mass at each of a series of increasing temperatures, and (3) dynamic TGA (Figure a1.9-C); the sample is heated with a temperature changing in a predetermined manner, generally at a linear rate. Dynamic TGA is the most used procedure. Therefore it is commonly designated as TGA method¹⁹.

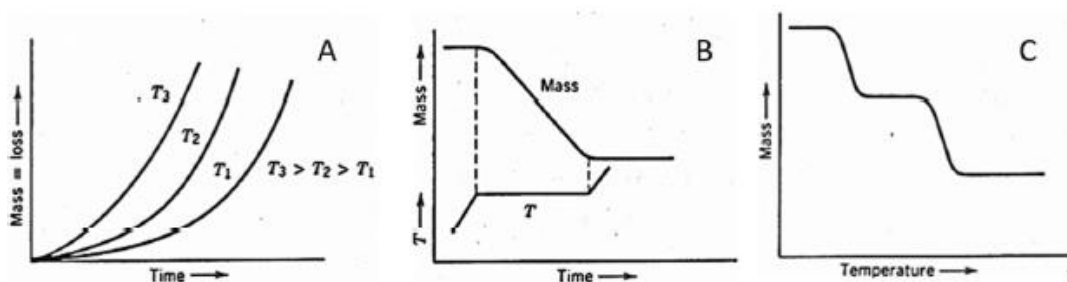
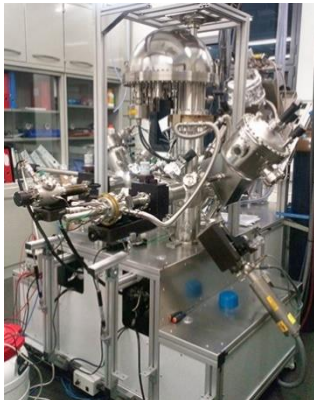


Figure a1.9. Representation of TGA graphics of the three different modes¹⁹.

X-ray photoelectron spectroscopy, XPS

XPS is used to obtain information about the composition of the material. In this work, the stoichiometric rate of the precipitate formed during arsenic reduction-adsorption process was studied by XPS. The equipment description is specified in Table a1.13.

Table a1.13. XPS employed in the study

Equipment	XPS
<i>Model</i>	Phoibos 150 electron energy analyser
<i>Company and Country</i>	SPECS, Germany
<i>Laboratory analysis</i>	ICN2 (Barcelona, Spain)
<i>Image</i>	

Sample preparation

Powders samples are sprinkled onto the surface of sticky carbon tape or pressed into a tablet for analysis.

Basic XPS fundamentals

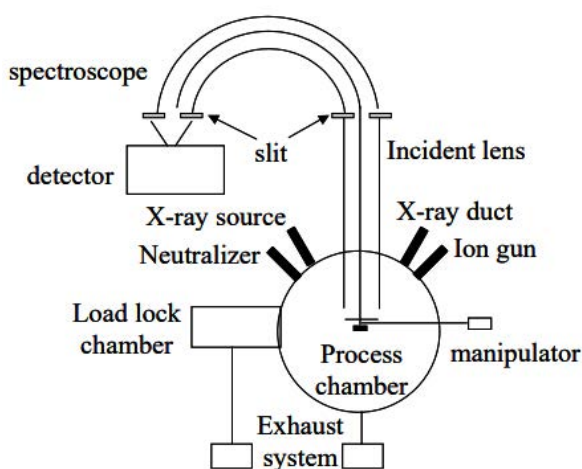


Figure a1.10. Schematic XPS system

An electron is emitted by the photoelectric effect when homogeneous light is applied material. The measuring method of electron energy and intensity distribution is called XPS method (Figure a1.10) (equation a1.5).

$$E_{kin}^v = h\nu - E_b - \phi \quad (a1.5)$$

where E_{kin}^v , $h\nu$, E_b and ϕ are kinetic energy of liberated photoelectron, incident X-ray energy, binding energy of emitted electron for sample and work function for a sample. If $h\nu$ is constant, binding


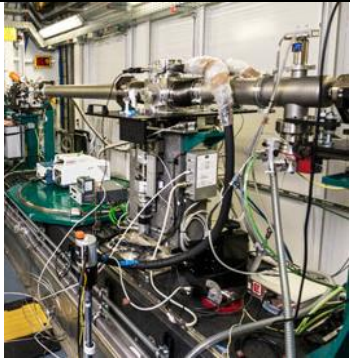
energy can be obtained by measuring the kinetic energy of the emitted electron. Identification of element is easily possible by measuring E_{kin} because binding energy of each electron orbit is different. On the other hand, binding energy of the same orbit of the same element is changed a little by an atomic surrounding state and environment. A state analysis of element is possible by measuring this change variation called chemical shift. Additionally, the mean free path of the electron is not so long because of scattering and absorption process of electron in solid. Therefore, since XPS method can observe only the surface of nm order, it is suitable for thin film evaluation

X-Ray Absorption Near Edge Structure, XANES

XAS experiments were carried out in two different Synchrotron facilities. While XAS experiments for antimony speciation on the sponge and sponge+SPION system at different pH were developed at ESRF (Grenoble, France), experiments for antimony speciation at different initial concentrations as well as iron speciation were performed at ALBA (Cerdanyola del Valles, Spain)

The experimental beamlines and the specific conditions for each beamline setup are specified in Table a1.14.

Table a1.14. Beamline setup for each synchrotron radiation source facilities

	Synchrotron facilities	
	ESRF	ALBA
<i>Synchrotron image</i>		
<i>Beamline</i>	BM25-16 bunch mode	CLAESS
<i>Energy Source</i>	5-45 KeV	2.4-63.2 keV
<i>Monochromator crystals</i>	Si (111)	Si(111) and Si(311)
<i>Spot size at the sample</i>	1.5 x 1.0 mm	100x200 μm^2 to 1x10 mm ²
<i>Detectors</i>	3 Ionization chambers (Transmittance) and Si(Li) 13 elements (Fluorescence)	silicon-drift and CdTe single channel fluorescence detector
<i>Temperature</i>	Room temperature	Room temperature

Sample preparation

For antimony and iron XAS analysis, sponge and sponge+SPION samples were dried, homogenised, milled to a fine powder in a mortar and mixed with cellulose powder, which is transparent to X-rays. Then, they were converted into pellets by hydraulic pressure (hydraulic press 25 t RIIC, London) to be analysed at the experimental station of the synchrotron facility. The obtained pellets were encapsulated in Kapton® foils in order to avoid direct contact with the atmosphere and conserve the sample properties. Kapton® is a high-temperature polyimide, and it is used in the sample preparative for synchrotron analysis due to its excellent physicochemical properties such as high temperature resistance, being chemically inert and high resistance to ionising radiation performance.

As the different samples, the reference samples for individual antimony and iron species consist of a homogenised mixture of reference sample with cellulose to dilute and give consistency to the pellet. Later, the samples were homogenised, milled to a fine powder and converted into pellets by hydraulic pressure like the target samples.

Compounds that were employed in the SPION synthesis or the antimony adsorption process were used as reference compounds. Thus, $C_4H_4KO_7Sb \cdot 0,5H_2O$ and $(K[Sb(OH)_6])$ are the compounds employed to prepare the reference samples for antimony. For iron, chloride salts ($FeCl_2 \cdot 4H_2O$ and $FeCl_3 \cdot 6H_2O$) which were used in the SPION synthesis and SPION references were the principal references to determine if any structural change is produced in the adsorption process. The necessary amount of sample in each pellet was calculated with Absorbix v3.02.S3¹⁹.

XAS measurements

XAS experiments for the antimony and iron speciation studies were carried out at both BM25, and CLAESS beamlines described in the previous section, the influence of pH in adsorption process were studied in ESRF whereas the influence of the initial concentration was studied in ALBA. As can be observed in Figure a1.11, a common experimental setup is composed of 3 ionisation chambers (IC) aligned with the sample position and a fluorescence detector perpendicular to the sample position.

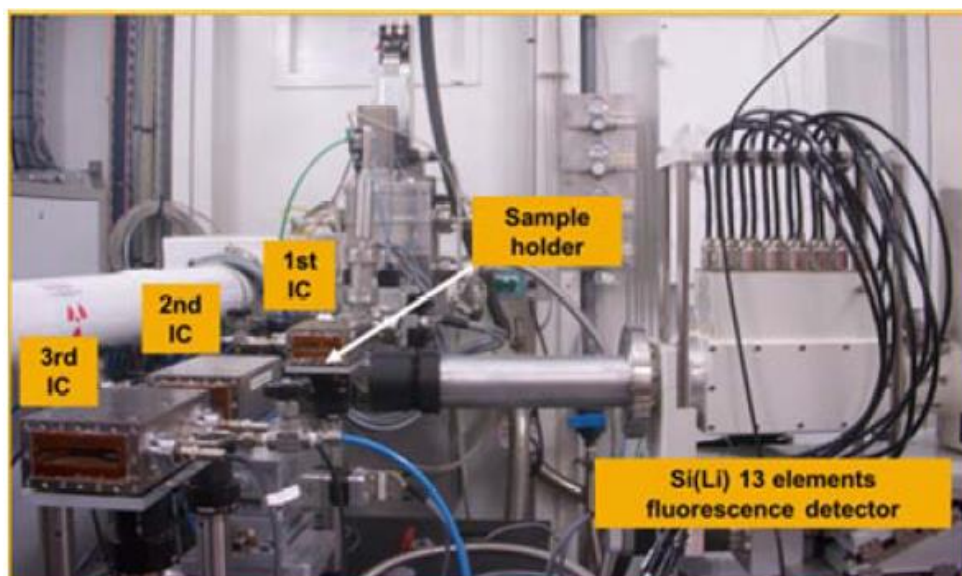


Figure a1.11. Experimental setup for XAS analysis in ESRF BM25 beamline in Grenoble.

Antimony absorption was recorded at the edge energy for its K line 30491 eV and its fluorescence $K_{\alpha 1}$ at eV and $K_{\beta 1}$ at eV. In the same way, iron absorption was recorded at the edge energy for its K line at 7112 eV and its fluorescence $K_{\alpha 1}$ at 6405.2 eV and $K_{\beta 1}$ at 7059.3 eV.

Three main spectral regions can be observed in the typical XAS absorption spectra. Such regions contain related, but slightly different, information about an element's local coordination and oxidation state as Figure a1.12 shows.

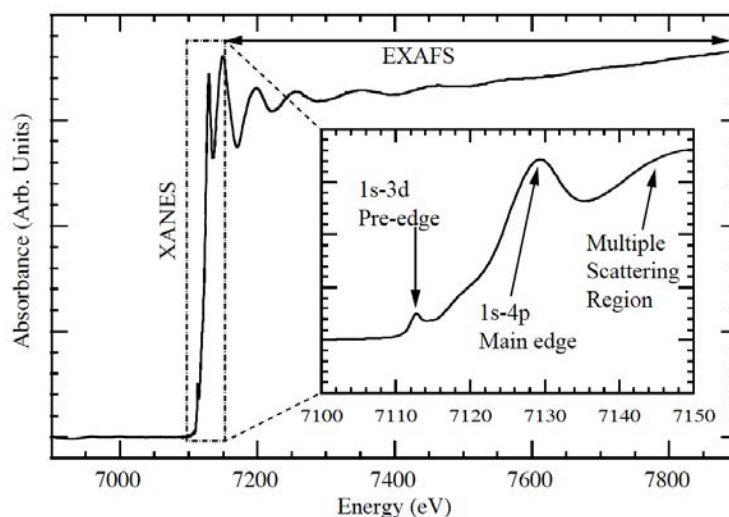


Figure a1.12. Typical X-ray absorption spectrum

- a) *Pre-edge* ($E < E_0$): About 2-50 eV below the main absorption edge. In this region where no significant absorption phenomena occur, only electronic transitions from the core level to the higher unfilled or half-filled orbitals.
- b) *XANES*: In the region between 2eV below up to 50 eV above the absorption edge. In this region, transitions of core electrons to non-bound levels with close energy occur. Because of the high probability of such a transition, a sudden rise of absorption is observed.
- c) *EXAFS*: The region starts approximately from 50 eV and continues up to 1000 eV above the edge. In this region, the photoelectrons have high kinetic energy, and single scattering by the nearest neighbouring atoms normally dominates.

Before starting the XAS analysis, an X-Ray absorption experiment must be recorded over the sample to determine the actual absorption peak for the element of interest (intensity vs wavelength) under the established conditions. Once the possible interferences are determined and removed, the optimum spot size is selected. A fluorescence spectrum is performed (fluorescence intensity vs energy), which is scanned by energy steps according to the region of interest. In this sense, pre-edge and edge region are needed to be thoroughly studied, being the number of the steps in this region higher than in the rest of the spectra and subsequently, the resolution of the XAS spectra is higher.

Both fluorescence and transmittance intensities are registered by using different detectors. The selection of the detection mode depends upon the sample concentration and the matrix background²⁰. Transmission mode measures sample absorption and is typically used for a high concentration of absorber (>2 wt%). The absorption by a sample of thickness x and the absorption coefficient μ is related to the ration I_0 , and I show the following equation a1.6.

$$\mu x = \ln(I/I_0) \quad (a1.6)$$

Consequently, the right thickness for transmission measurements requires a uniform sample, free of pinholes. Fluorescence detection follows the fluorescent X-Ray yield from the front face of the sample. Fluorescence detection is used for samples with lower absorber concentrations (>2 wt%), with high matrix absorption or for very small samples, and therefore, I/I_0 is proportional to μ . Hence, due to a higher signal-to-noise ratio, the fluorescence yield is 10 to 100 times more sensitive than absorption coefficients measured in transmittance mode.

Therefore, reference compounds were analysed by transmittance mode. Due to these standards are pure samples with high concentration, the spectra are very sharp and fewer replicates are needed. The unknown samples were analysed by fluorescence detection mode (multi-element solid state detector) as they present more noise when the

concentration is lower. Then, more replicated and more analysis time are needed to obtain sharp spectra.

XAS data treatment

The XAS spectra were analysed with XAS data analysis software ATHENA (distributed with the Demeter software package²¹). Data analysis is focused in XANES region, which informs about the oxidation state for the antimony adsorbed in the sponge+SPION system. Samples were analysed after the antimony adsorption.

Average of spectra replicates for each reference, and unknown sample was made, the energy is calibrated, and background correction and edge normalisation were performed.

Antimony quantitative speciation is performed in two main steps:

- Principal Components Analysis (PCA): it consists of a mathematical decomposition of a set of data files into the minimum number of components needed to describe the variance in the data. These principal components are mathematically sufficient to reconstruct each of the experimental spectra by any linear combination. The main outcome of this procedure is the determination of the number and type of reference compounds needed to describe the set of data files within the experimental error (REF 16,17).
- Least squares are fitting: this is the second step regarding speciation analysis, which consists of the fitting of reference compounds to the already corrected experimental data. The fingerprint adjustments are normally achieved by the minimisation of the least squares fitting between the sample spectra and a combination of reference spectra.

ATHENA is the data treatment software used to perform the speciation analysis. That program produces, in a first step, the iterative PCA adjustments until no more significant components are identified and, in a second one, the linear combination of all components spectra by least squares fitting to get a 100 % fit ($\pm 10\%$ error is allowed) (ref 18).

The relative quality of the fit was quantified by the residual value, a measure of how close the fit (xfit) is to the data (xdata) based on a sum of square differences.

References

- (1) Ha, Y.; Tsay, O. G.; Churchill, D. G. A Tutorial and Mini-Review of the ICP-MS Technique for Determinations of Transition Metal Ion and Main Group Element Concentration in the Neurodegenerative and Brain Sciences. *Monatshefte für Chemie* **2011**, *142* (4), 385–398.
- (2) Khlebtsov, N. G. Determination of Size and Concentration of Gold Nanoparticles from Extinction Spectra. *Anal. Chem.* **2008**, *80* (17), 6620–6625.
- (3) Volkamer, R.; Spietz, P.; Burrows, J.; Platt, U. High-Resolution Absorption Cross-Section of Glyozal in the UV-Vis and IR Spectral Ranges. *J. Photochem. Photobiol. A Chem.* **2005**, *172* (1), 35–46.
- (4) Culbertson, C. T.; Jorgenson, J. W. Lowering the UV Absorbance Detection Limit in Capillary Zone Electrophoresis Using a Single Linear Photodiode Array Detector. *Anal. Chem.* **1998**, *70* (13), 2629–2638.
- (5) Rueden, C. T.; Schindelin, J.; Hiner, M. C.; DeZonia, B. E.; Walter, A. E.; Arena, E. T.; Eliceiri, K. W. ImageJ2: ImageJ for the next Generation of Scientific Image Data. *BMC Bioinformatics* **2017**, *18* (1), 1–26.
- (6) Zhu, Y.; Jiang, F. Y.; Chen, K.; Kang, F.; Tang, Z. K. Size-Controlled Synthesis of Monodisperse Superparamagnetic Iron Oxide Nanoparticles. *J. Alloys Compd.* **2011**, *509* (34), 8549–8553.
- (7) Maleki, H.; Simchi, A.; Imani, M.; Costa, B. F. O. Size-Controlled Synthesis of Superparamagnetic Iron Oxide Nanoparticles and Their Surface Coating by Gold for Biomedical Applications. *J. Magn. Magn. Mater.* **2012**, *324* (23), 3997–4005.
- (8) *Scanning Microscopy for Nanotechnology.*; Zhou, W., Wang, Z. L., Eds.; Springer-Verlag New York, 2007.
- (9) Kalantar-zadeh, K.; Fry, B. *Nanotechnology-Enabled Sensors*; Springer US, 2008.
- (10) Cullity, B. D. *Elements of X-Ray Diffraction*; Addison-Wesley, Reading, 1978.
- (11) Adolphi, N. L.; Huber, D. L.; Jaetao, J. E.; Bryant, H. C.; Lovato, D. M.; Fegan, D. L.; Venturini, E. L.; Monson, T. C.; Tessier, T. E.; Hathaway, H. J.; et al. Characterization of Magnetite Nanoparticles for SQUID-Relaxometry and Magnetic Needle Biopsy. *J. Magn. Magn. Mater.* **2009**, *321* (10), 1459–1464.
- (12) Tayefeh, A.; Mousavi, S. A.; Wiesner, M.; Poursalehi, R. Synthesis and Surface Characterization of Magnetite-Titania Nanoparticles/Polyamide Nanocomposite Smart RO Membrane. *Procedia Mater. Sci.* **2015**, *11*, 342–346.
- (13) Nakamoto, K. *Infrared and Raman Spectra of Inorganic and Coordination Compounds*; John Wiley&Sons, 1986.
- (14) Colthup, N. B.; Daly, L. H.; Wiberley, S. E. Vibrational and Rotational Spectra. In *Introduction to Infrared and Raman Spectroscopy (Third Edition)*; Colthup, N. B., Daly, L. H., Wiberley, S. E., Eds.; Academic Press: San Diego, 1990; pp 1–73.
- (15) Alejandro Gómez Roca. Preparación de Nanopartículas Magnéticas Uniformes y de Alta Cristalinidad Para Biomedicina, Universidad Complutense de Madrid, 2009.
- (16) Zhang, C.; Xie, X. Controllable Assembly of Hydrophobic Superparamagnetic Iron Oxide Nanoparticle with MPEG-PLA Copolymer and Its Effect on MR Transverse Relaxation Rate. *J. Nanomater.* **2011**, *1*, 7pp.
- (17) Mahmoudi, M.; Simchi, A.; Milani, A. S.; Stroeve, P. Cell Toxicity of Superparamagnetic Iron Oxide Nanoparticles. *J. Colloid Interface Sci.* **2009**, *336* (2), 510–518.
- (18) Warner, C. L.; Addleman, R. S.; Cinson, A. D.; Droubay, T. C.; Engelhard, M. H.; Nash, M. A.;

- Yantasee, W.; Warner, M. G. High-Performance, Superparamagnetic, Nanoparticle-Based Heavy Metal Sorbents for Removal of Contaminants from Natural Waters. *ChemSusChem* **2010**, 3 (6), 749–757.
- (19) Wendlandt, W. W. *Thermal Analysis*; Wiley, 1986.
- (20) Koningsberger, D. C.; Prins, R. *X-Ray Absorption : Principles, Applications, Techniques of EXAFS, SEXAFS, and XANES*; Wiley, 1988.
- (21) Ravel, B.; Newville, M. ATHENA, ARTEMIS, HEPHAESTUS: Data Analysis for X-Ray Absorption Spectroscopy Using IFEFFIT. In *Journal of Synchrotron Radiation*; 2005.

Annexe 2. ELECTROCHEMICAL SETUP REVIEW¹⁻³

Electrodes used in Electrochemistry

The **working electrode** is the electrode in an electrochemical system on which the reaction of interest is occurring. Common working electrodes can be made of inert materials such as Au, Ag, Pt, glassy carbon (GC) and Hg drop and film electrodes. For corrosion applications, the material of the working electrode is the material under investigation (which is actually corroding). The size and shape of the working electrode also varies, and it depends on the application.

The **counter electrode (also known as an auxiliary electrode)**, is an electrode which is used to close the current circuit in the electrochemical cell. It is usually made of an inert material (e.g. Pt, Au, graphite, glassy carbon) and usually it does not participate in the electrochemical reaction. Because the current is flowing between the WE and the CE, the total surface area of the CE (source/sink of electrons) must be higher than the area of the WE so that it will not be a limiting factor in the kinetics of the electrochemical process under investigation.

The **reference electrode** is an electrode which has a stable and well-known electrode potential, and it is used as a point of reference in the electrochemical cell for the potential control and measurement. The high stability of the reference electrode potential is usually reached by employing a redox system with constant (buffered or saturated) concentrations of each participant of the redox reaction. Moreover, the current flow through the reference electrode is kept close to zero (ideally, zero) which is achieved by using the CE to close the current circuit in the cell together with a very high input impedance on the electrometer (> 100 GOhm).

Basic principle of a potentiostat/galvanostat

A basic diagram of a potentiostat/galvanostat is presented in Figure a2.1.

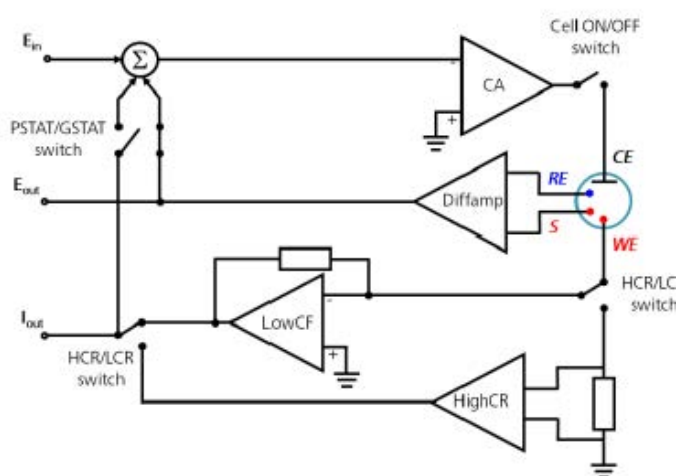


Figure a2.1. Basic diagram of a potentiostat/galvanostat

In *potentiostatic mode*, a potentiostat/galvanostat will accurately control the potential of the *Counter Electrode* (CE) against the *Working Electrode* (WE) so that the potential difference between the working electrode (WE) and the *Reference Electrode* (RE) is well defined, and correspond to the value specified by the user. In *galvanostatic mode*, the current flow between the WE and the CE is controlled. The potential difference between the RE and WE and the current flowing between the CE and WE are continuously monitored. The value specified by the user (i.e. applied potential or current) is accurately controlled, anytime during the measurement by using a negative feedback mechanism.

As can be seen from the diagram, the CE is connected to the output of an electronic block, which is called *Control Amplifier* (CA). The control amplifier forces a current to flow through the cell. The value of the current is measured using a *Current Follower* (LowCF) or a *Shunt* (HighCR), for low and high currents, respectively. The potential difference is always measured between the RE and S (Sense connection, used to sense the voltage of the WE) with a *Differential Amplifier* (Diffamp). The signal is then fed into the *Summation Point* (Σ) which, together with the waveform set by the digital-to-analogue converter (E_{in}), will be used as an input for the control amplifier.

The cell cables of the potentiostat/galvanostat (Figure a2.2) have a total of five connectors: WE, CE, RE, S and ground. The potential is always measured between the RE (blue) and the S (red) and the current is always measured between the WE (red) and CE (black). The ground connector (green) can be used to connect external devices to the same ground of the potentiostat/galvanostat.

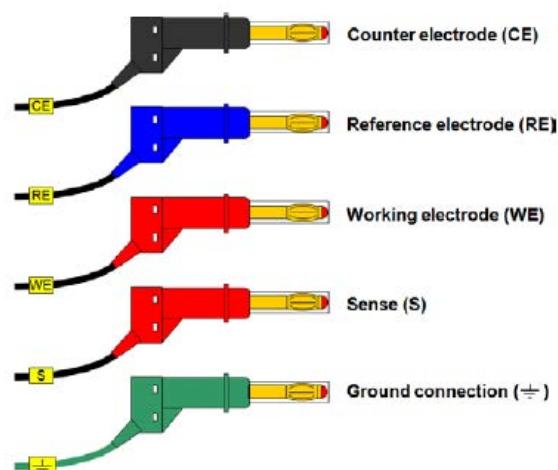


Figure a2.2. The connections available on the cell cables of the potentiostat/galvanostat and the colour code used

Controlled-Potential Electrolysis with a Three-Electrode Cell

An **electroactive species** is one that can be oxidised or reduced at an electrode. We regulate the potential of the working electrode to control which electroactive species react and which do not. Metal electrodes are said to be **polarizable**, which means that their potentials are easily changed when small currents flow. A reference electrode such as calomel or is said to be **nonpolarizable** because its potential does not vary much unless a significant current is flowing. Ideally, we want to measure the potential of a polarizable working electrode concerning a nonpolarizable reference electrode. How can we do this if there is to be significant current at the working electrode and negligible current at the reference electrode? The answer is to introduce a third electrode (Figure a2.3 a)

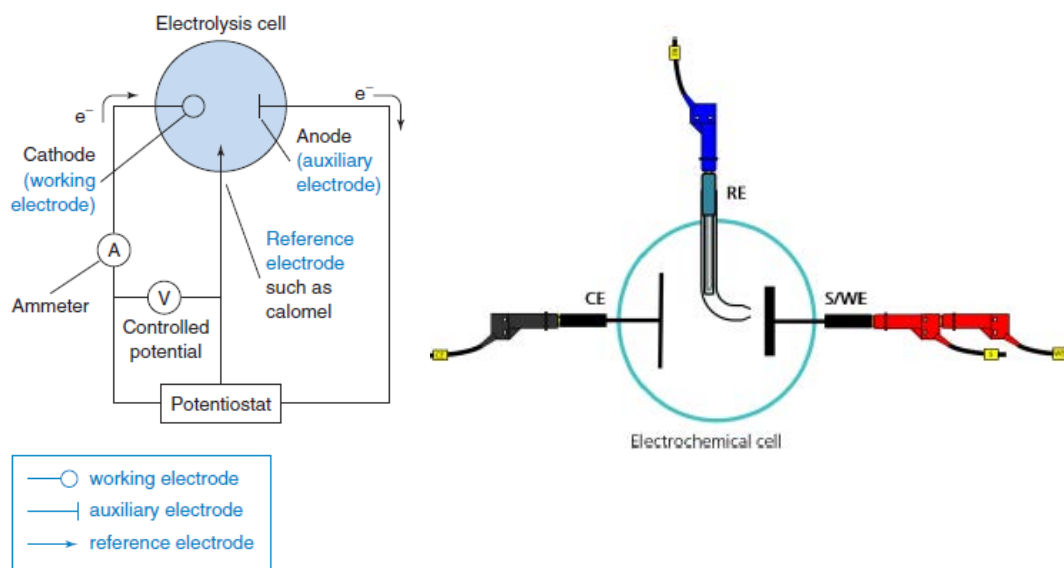


Figure a2.3. a) The circuit used for controlled potential electrolysis with a three-electrode cell. b) Schematic view of the three electrodes setup.

Three-electrode cell setup (Figure a2.3 b) is the most common electrochemical cell setup used in electrochemistry. In this case, the current flows between the CE and the WE. The potential difference is controlled between the WE and the CE and measured between the RE (kept at proximity of the WE), and S. Because the WE is connected with S and WE is kept at pseudo-ground (fixed, stable potential), by controlling the polarization of the CE, the potential difference between RE and WE is controlled all the time. The potential difference between the WE and CE usually is not measured. This is the voltage applied by the control amplifier, and it is limited by the compliance voltage of the instrument. It is adjusted so that the potential difference between the WE and RE will be equal to the potential difference specified by the user. This configuration allows the potential across the electrochemical interface at the WE to be controlled concerning the RE.

References

- (1) Bard, A. J.; Faulkner, L. R. *Electrochemical Methods, Fundamentals and Applications*; Swain, E., Robey, C., Eds.; John Wiley & Sons, Ltd., 2001.
- (2) Pansini, M.; Sannino, F.; Marocco, A.; Allia, P.; Tiberto, P.; Barrera, G.; Polisi, M.; Battista, E.; Netti, P. A.; Esposito, S. Novel Process to Prepare Magnetic Metal-Ceramic Nanocomposites from Zeolite Precursor and Their Use as Adsorbent of Agrochemicals from Water. *J. Environ. Chem. Eng.* **2018**, 6 (1), 527–538.
- (3) Autolab B.V, M. *Autolab Application Note EC08. Basic Overview of the Working Principle of a Potentiostat/Galvanostat (PGSTAT)*; 2011.

Annexe 3. MAGNETISM

Magnetism is a unique physical property that helps in water purification. Its combination with adsorption techniques, using magnetic adsorbents, has therefore been used extensively in water treatment and for environmental purposes¹⁻⁴. Magnetic separation technology as an efficient, fast and economical method for separating magnetic adsorbents has been widely used in textile, biology, and environmental protection⁵. The advantages of these products are that it can dispose a mass of wastewater in a very short period and produce no contaminants⁵ and its ease of separation by an external magnetic field and possibility of simple recovery after washing with acidic aqueous solution¹.

Magnetic materials

The magnetism of a solid depends, basically, on electrons of the atoms that formed it, in particular on the number of unpaired valence electrons present in the atoms of solid, as well as, on the orbital in which they are. If an external magnetic field is applied to the solid, the electrons give rise to magnetic dipoles that are ordered with the field generating a magnetic moment inside this one.

Solids can be classified according to the magnetic response by applying an external magnetic field. If the solid presents atoms with paired electrons, it is *diamagnetic*. In this case, if a magnetic field is applied, the magnetic dipoles generation is forced, giving rise to an induced current that tends to oppose that magnetic field. An example of a diamagnetic material is water and proteins within the human body that contain carbon, hydrogen and nitrogen⁶.

On the other hand, if the solid has atoms with unpaired electrons and the interactions between them are weak, the solid is *paramagnetic*. When an external magnetic field is applied, dipoles are generated and aligned in the same direction to the field. However, by removing the magnetic field, the thermal fluctuations cause that the magnetic moments move randomly obtaining a magnetic moment zero.

When the interactions between the unpaired electrons of neighbouring atoms are stronger, the solid has a *ferromagnetic* behaviour. In this case, all the magnetic moments are oriented in the same direction, parallel or antiparallel (even in the absence of applied external magnetic field), because the electrons interact by an exchange mechanism⁷. If the electrons are aligned antiparallel and if the magnetic moment is cancelled by itself, the solid is *antiferromagnetic*, but if the resulting magnetic moment is not cancelled, the solid is *ferrimagnetic*.

Considering a ferromagnetic solid, if all the magnetic moments are oriented in the same direction a large amount of magnetostatic energy is generated, and the solid regroups the spins in regions called magnetic domains⁸ (Figure a3.1). Within each domain, the spins are oriented towards the same direction but different from the other magnetic domains. Although energy is generated in the interface between domains (domain walls), this multidomain configuration within the solid is the most favourable energetically. The size of the magnetic domain depends on the intrinsic properties of the solid (magnetic anisotropy, magnetic moment and the exchange anisotropy) and the shape^{4, 10}.

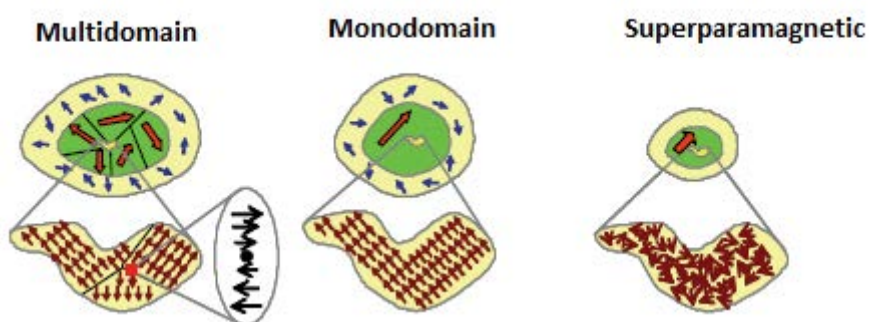


Figure a3.1. Magnetic structure of ferromagnetic solids based on particle size (multidomain and monodomain) and superparamagnetic. (modified from Roca et al.⁸).

Nano effect. Superparamagnetism

Magnetic properties of bulk materials depend mainly on their composition, their crystallographic structure, their energy of magnetic anisotropy, their vacancies and defects⁹. However, when the size decreases until reaching the nanometric regime, the surface/volume ratio becomes a key parameter that controls the magnetic properties of the particles¹⁰.

As explained above, ferromagnetic bulk materials have a net magnetic moment in the absence of a magnetic field. However, by decreasing the volume until reaching the monodomain regime, there is a transition temperature (T_B), known as blocking temperature, above which the material behaves as superparamagnetic. When a ferromagnet is sufficiently small, it acts like a single magnet spin that is subject to Brownian motion¹¹. In the absence of an external magnetic field, their magnetisation appears to be in average zero: such materials are said to be in the superparamagnetic state. In this state, an external magnetic field can magnetise the NPs, similarly to a paramagnet but with higher stability. If enough energy is supplied, magnetism can be reversed along this axis. Therefore no hysteresis is observed.

Magnetic characterisation

When a magnetic field is applied to a ferromagnetic specimen, the magnetisation may vary from zero to the saturation value, which is the point at which all of the domains are parallel to each other. The graphical representation of a material's magnetisation against the strength of an applied magnetic field provides the magnetisation curve with a characteristic sigmoidal shape, where the magnetic saturation is reached if the applied magnetic field is large enough as the Figure a3.2 shows, which is called hysteresis loop.

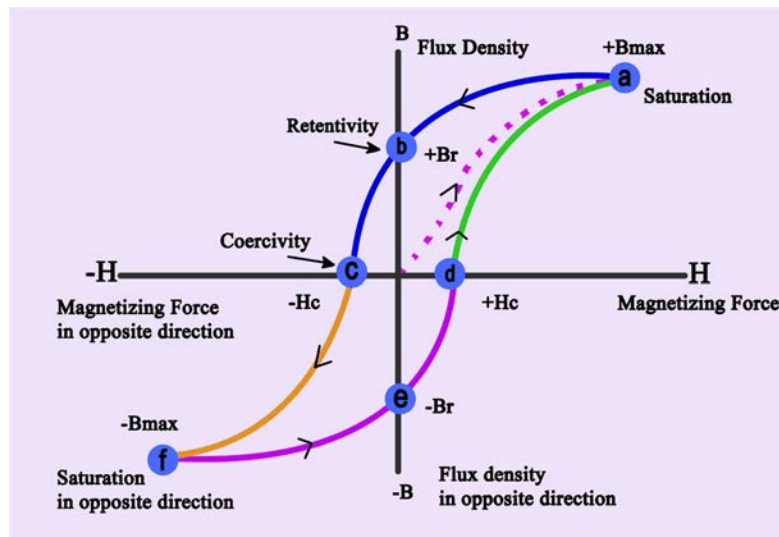


Figure a3.2. Magnetisation curve displaying hysteresis loop.

A hysteresis loop shows the relationship between the induced magnetic flux density (B) and the magnetising force (H). A ferromagnetic material that has never been previously magnetised or has been thoroughly demagnetised will follow the dashed line as H is increased. As the line demonstrates, the greater the amount of current applied (H+), the stronger the magnetic field in the component (B+). At point "a" almost all of the magnetic domains are aligned, and an additional increase in the magnetising force will produce very little increase in magnetic flux. The material has reached the point of *magnetic saturation*. When H is reduced to zero, the curve will move from point "a" to point "b." At this point, it can be seen that some magnetic flux remains in the material even though the magnetising force is zero. This is referred to as the point of *retentivity* on the graph and indicates the *remanence* or *level of residual magnetism in the material*. (Some of the magnetic domains remain aligned, but some have lost their alignment.) As the magnetising force is reversed, the curve moves to point "c", where the flux has been reduced to zero. This is called the *point of coercivity* on the curve. (The reversed magnetising force has flipped enough of the domains so that the net flux within the material is zero.) The force required to remove the residual magnetism from the material is called the *coercive force* or *coercivity* of the material.

As the magnetising force is increased in the negative direction, the material will again become magnetically saturated but in the opposite direction (point "d"). Reducing H to zero brings the curve to point "e." It will have a level of residual magnetism equal to that achieved in the other direction. Increasing H back in the positive direction will return B to zero. Notice that the curve did not return to the origin of the graph because some force is required to remove the residual magnetism. The curve will take a different path from point "f" back to the saturation point where it will complete the loop.

From the hysteresis loop, several primary magnetic properties of a material can be determined¹²:

Saturation magnetisation M_s (emu/g): strictly, the magnetisation of a uniformly magnetised region (domain) in a homogeneous magnetic medium. It is the magnetisation value when all the magnetic moments are aligned with the applied external magnetic field. This is an intrinsic property, a function of temperature, and weakly dependent on magnetic field and stress. In practice, M_s is also used for the magnetisation M of any (not necessarily homogeneous) magnetic material in a large applied field (point an in Figure a3.2).

Remanent magnetisation, M_r (emu/g): the magnetisation of a magnetic object that remains after it has been magnetised in a large applied field that is subsequently removed. Remanence is an extrinsic quantity that depends on microstructure, shape (point b and e in Figure a3.2)

Coercivity H_c (Oe): the value of reverse applied magnetic field required to reduce the magnetisation from remanence to zero in the presence of the reversing field (point c and d in Figure a3.2).

Initial susceptibility, χ_i (emu/gT): the magnetisation observed in low fields, on the order of the earth's field (± 100 Oe).

For some magnetic particles, particularly for magnetic iron oxides, the shape of the magnetisation curve is often dependent on the nanoparticle size. If the particles are of large size ($1\mu\text{m}$), hysteresis is observed, while for nanoparticles, no hysteresis is observed due to a superparamagnetism¹³.

Zero Field Cooled and Field Cooled (ZFC/FC) curves. Blocking temperature

As stated above, the **blocking temperature**, T_B (K) represents the threshold temperature above which magnetic anisotropy barrier is overcome by thermal activation energy alone, causing nanoparticles to relax from the ferrimagnetic state to the superparamagnetic state characterised by randomised magnetic moments of the particles in the absence of an external magnetic field¹⁴. Also, the temperature where the maximum magnetisation is reached (in ZFC), T_m , is an important parameter to be considered. This parameter is calculated by studying the hysteresis loop at different temperatures. In this work, the T_B and T_m value is calculated using Zero Field Cooled/Field Cooled (ZFC/FC) curves.

ZFC/FC curves provide more information about magnetic properties, providing information about the T_B and quality information about particles size distribution. In this kind of experiment, a sample is cooled from a temperature where all particles show superparamagnetic behaviour to the lowest reachable temperature (usually around 3-5 K), then, a small constant field usually between 50-100 Oe is applied, and the sample is heated to a temperature high enough to observe an initial growth and subsequent decrease of its magnetization, i.e., up to the temperature range where the sample shows superparamagnetic behaviour (ZFC) again. The sample is then cooled again to the lowest temperature with the constant field still applied. Then, magnetisation is registered until room temperature applying the same constant field (FC). In the ideal case of a monosize non interacting MNPs sample, a narrow temperature region should exist in which the system performs a transition between irreversible and reversible regimes (Figure a3.3 a). Real samples always present a size dispersion, usually reasonably well described by a log-normal distribution. So, in real ZFC-FC experiments, the blocking region is wide, and a representative T_B value of the ensemble is not well defined (Figure a3.3 b).

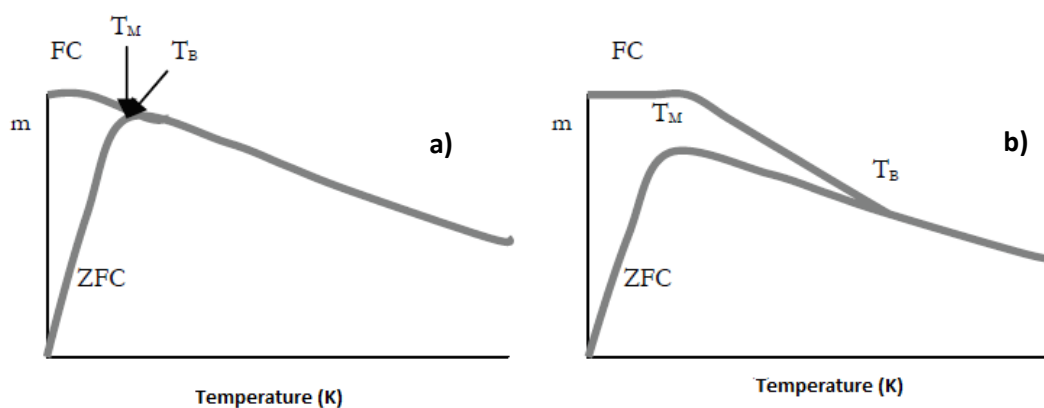


Figure a3.3. Example of ZFC/FC curves in a) Particle system with a narrow distribution of sizes b) Particle system with broad size distribution (modified from Roca et al.⁸).

In the case of a superparamagnetic material at room temperature, the magnetic moments of the particles are initially aligned randomly, and its direction fluctuates. When the temperature decreases, the magnetic moments are locked randomly. The application of a magnetic field while the temperature rises produce the increase of the magnetic moments of the smaller particles that will be unlocked and aligned with the magnetic field direction, increasing the magnetisation value. As the temperature continues growing, the larger ones will progressively reach a temperature where all the particles have their moments unlocked and aligned with the field. When 50% of the particles have reached the superparamagnetic state, the maximum magnetisation value is reached. Once that temperature has passed, the value of the magnetisation decreases due to temperature effect.

Regarding the FC curve, magnetisation value is constant, theoretically, until the TB is reached, where ZFC and FC curves converged, and all the magnetic moments are unlocked.

References

- (1) Mahdavian, A. R.; Mirrahimi, M. A. S. Efficient Separation of Heavy Metal Cations by Anchoring Polyacrylic Acid on Superparamagnetic Magnetite Nanoparticles through Surface Modification. *Chem. Eng. J.* **2010**, *159* (1–3), 264–271.
- (2) Zhang, G.; Qu, J.; Liu, H.; Liu, R.; Wu, R. Preparation and Evaluation of a Novel Fe-Mn Binary Oxide Adsorbent for Effective Arsenite Removal. *Water Res.* **2007**.
- (3) Gong, J. L.; Wang, B.; Zeng, G. M.; Yang, C. P.; Niu, C. G.; Niu, Q. Y.; Zhou, W. J.; Liang, Y. Removal of Cationic Dyes from Aqueous Solution Using Magnetic Multi-Wall Carbon Nanotube Nanocomposite as Adsorbent. *J. Hazard. Mater.* **2009**, *164* (2–3), 1517–1522.
- (4) Cui, H. J.; Cai, J. K.; Zhao, H.; Yuan, B.; Ai, C. L.; Fu, M. L. Fabrication of Magnetic Porous Fe-Mn Binary Oxide Nanowires with Superior Capability for Removal of As(III) from Water. *J. Hazard. Mater.* **2014**.
- (5) Feng, Y.; Gong, J. L.; Zeng, G. M.; Niu, Q. Y.; Zhang, H. Y.; Niu, C. G.; Deng, J. H.; Yan, M. Adsorption of Cd (II) and Zn (II) from Aqueous Solutions Using Magnetic Hydroxyapatite Nanoparticles as Adsorbents. *Chem. Eng. J.* **2010**, *162* (2), 487–494.
- (6) Pankhurst, Q. A.; Connolly, J.; Jones, S. K.; Dobson, J. Applications of Magnetic Nanoparticles in Biomedicine. *J. Phys. D Appl. Phys. To cite this Artic.* **2003**, *36*, 167–181.
- (7) Coey, J. M. D. Magnetic Properties of Iron in Soils, Iron Oxides and Clay Minerals. In *Iron in soils and clay minerals*; J.W. Stucki W. Goodman, B. A. S., Ed.; D. Reidel Publishing Company, 1988; pp 397–466.
- (8) Alejandro Gómez Roca. Preparación de Nanopartículas Magnéticas Uniformes y de Alta Cristalinidad Para Biomedicina, Universidad Complutense de Madrid, 2009.
- (9) Cornell, R. M.; Schwertmann, U. *The Iron Oxides. Structure, Properties, Reactions, Occurrences and Uses*; 1996.
- (10) Batlle, X.; Labarta, A. Finite-Size Effects in Fine Particles: Magnetic and Transport Properties. *J. Phys. D Appl. Phys.* **2002**, *35*, R15–R42.
- (11) Mishima, N.; Petrosky, T. Y.; Minowa, H.; Goto, S. Model Experiment of Two-dimensional Brownian Motion by Microcomputer. *Am. J. Phys.* **1980**, *48* (12), 1050–1055.

- (12) Indeck, R. S.; Muller, M. W.; Avazpour, L. Magnetic Recording Measurements. *Ref. Modul. Mater. Sci. Mater. Eng.* **2015**, *5* (September 2015), 1–19.
- (13) Lu, A. H.; Salabas, E. L.; Schüth, F. Magnetic Nanoparticles: Synthesis, Protection, Functionalization, and Application. *Angew. Chemie - Int. Ed.* **2007**, *46* (8), 1222–1244.
- (14) Tahar, L. Ben; Oueslati, M. H.; Abualreish, M. J. A. Synthesis of Magnetite Derivatives Nanoparticles and Their Application for the Removal of Chromium (VI) from Aqueous Solutions. *J. Colloid Interface Sci.* **2018**, *512*, 115–126.

Annex 4. KINETIC AND ISOTHERM MODEL

Table 1. Kinetic models

Models	Characteristics
<p><u>Pseudo-first order model (PFO)</u>¹⁻³</p> $q_t = q_e(1 - e^{-k_1 t})$ $\log(q_e - q_t) = \log q_e - k_1 t / 2.303$ <p>q_e (mg/g) = amount of adsorbate uptake per mass of adsorbent at equilibrium.</p> <p>q_t (mg/g) = amount of adsorbate uptake per mass of adsorbent at any time.</p> <p>k_1 (min⁻¹) = rate constant of the PFO equation.</p>	<p>The pseudo-first-order model is described by the non-reversible equation:</p> $S + M \rightarrow MS$ <p>The kinetic equation rests on five assumptions:</p> <ul style="list-style-type: none"> - Sorption only occurs on localised sites and involves no interaction between the sorbed ions - The energy of adsorption is not dependent on surface coverage - Maximum adsorption corresponds to a saturated monolayer of adsorbates on the adsorbent surface - The concentration of M is considered to be constant - The metal ion uptake on the activated carbon is governed by a first-order rate equation <p>k_1 parameter is the time-scaling factor, the value which decides how fast the equilibrium in the system can be reached. k_1 usually decreases with the increasing initial solute concentration in the bulk phase⁴</p>
<p><u>Pseudo-second order model (PSO)</u>^{2,3,5}</p> $q_t = \frac{k_2 q_e^2 t}{1 + k_2 q_e t}$ $\frac{t}{q_t} = \frac{1}{k_2 q_e^2} + \frac{t}{q_e}$ <p>q_e (mg/g) = amount of adsorbate uptake per mass of adsorbent at equilibrium.</p> <p>q_t (mg/g) = amount of adsorbate uptake per mass of adsorbent at any time.</p> <p>k_2 (g/mg min) = rate constant of the PSO equation</p>	<p>The kinetics of metal ion removal is described by the pseudo-second-order model as follows:</p> $2S + M \rightarrow M(S)_2$ <ul style="list-style-type: none"> - The assumptions are almost the same as for the pseudo-first-order model except the metal ion uptake is governed by a second-order rate equation - It is usually associated with the situation when the rate of direct adsorption/desorption process controls the overall sorption kinetics. The <i>rate-limiting step</i> may be chemical adsorption which involving valence forces through sharing or exchange of electrons between adsorbate and sorbent - The value of k_2 strongly depends on the applied operating conditions. It is usually strongly dependent on the applied initial solute concentration. It decreases with the increasing initial concentration as a rule, which is a commonly known fact related to the interpretation of k_2 as a time-scaling factor⁴

Elovich model^{6,7}

$$q_t = \frac{1}{\beta} \ln(1 + \alpha\beta t)$$

$$q_t = \left(\frac{1}{\beta}\right) \ln(\alpha\beta) + \left(\frac{1}{\beta}\right) \ln t \quad \alpha\beta t \gg 1$$

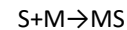
q_t (mg/g) = amount of adsorbate uptake per mass of adsorbent at any time.

a (mg/g·min) = Initial adsorption rate of Elovich equation

b = Related to the extent of surface coverage and activation energy for chemisorption

It is proposed for the description of the kinetics of the chemisorption of adsorbate by a solid in an aqueous medium⁶. Suppose a strong heterogeneity of the adsorbent surface

The kinetic of metal ion removal is described by the Elovich model as follows:



- Sorption only occurs on localised sites, and there is an interaction between the sorbed ions
- The energy of adsorption increases linearly with the surface coverage according to the law:
- The concentration of M is considered to be constant
- The metal ion uptake is negligible before the exponential (equivalent to a metal ion uptake governed by a zero order rate equation)

The applicability of the Elovich equation is restricted to the initial times of sorption process when the system is relatively far from equilibrium⁴

Intraparticle diffusion model (IPD)^{2,8}

$$q_t = k_p \sqrt{t} + C$$

q_t (mg/g) = amount of adsorbate uptake per mass of adsorbent at any time.

k_p (mg/g·min^{1/2}) = Rate constant of the intra-particle diffusion model

C (mg/g) = Constant associated with the thickness of the boundary layer

Adsorption onto porous materials is controlled in part by the intra-particle diffusion rate of the adsorbate. It can be useful for identifying the reaction pathways and adsorption mechanisms and predicting the rate-controlling step

For kinetics controlled solely by IPD:

- The linear fitting should pass through the origin ($C=0$). However, in most studies, this plot shows multilinearity over the entire adsorption period and provides better fit if not forced through the origin ($C>0$)
- Multilinearity is an indication of multiple mechanisms that control the process. Each linear segment represents a controlling mechanism or several simultaneous controlling mechanisms⁹:
 - Initial step: external surface adsorption or instantaneous adsorption occurs.
 - Second step: IPD begins.
 - Third step: the system approaches equilibrium

A higher value of C corresponds to a greater effect on the limiting boundary layer

Hyperbolic tangent model¹⁰

$$q = q_e [\tanh(kt)]^n$$

$$k = \frac{\pi}{t_e}$$

q_e (mg/g) = amount of adsorbate uptake per mass of adsorbent at equilibrium.

q_t (mg/g) = amount of adsorbate uptake per mass of adsorbent at any time.

k (min^{-1}) = rate constant

t_e (min) = required time for adsorption to reach the equilibrium state

n = constant

- The ability to predict the equilibrium time of adsorption, which is crucial to optimise the cost of the adsorption system design
- Model restriction: $q/q_e > 0.995$
- this model cannot only be used under this scale, but

Table 2. Isotherm models

Models	Characteristics
<p>Langmuir^{11,12}</p> $q_e = \frac{q_m K_L C_e}{1 + K_L C_e}$ <p>q_e (mg/g) = amount of solute adsorbed</p> <p>C_e (mg/L) = equilibrium concentration of the solute in the bulk solution</p> <p>q_m (mg/g) = maximum saturated monolayer adsorption capacity of the adsorbent</p> <p>K_L (L/mg) = Langmuir constant related to the affinity between the adsorbent and adsorbate</p>	<p>The model has the following hypotheses:</p> <ul style="list-style-type: none"> - Monolayer adsorption (the adsorbed layer is one molecule thick) - Adsorption takes place at specific homogeneous sites within the adsorbent - Once a molecule occupies a site, no further adsorption can take place at that site - Adsorptional energy is constant and does not depend on the degree of occupation of an adsorbent's active centre - The strength of the attractive intermolecular forces is believed to fall off rapidly with distance - The adsorbent has a finite capacity - All sites are identical and energetically equivalent - The adsorbent is structurally homogeneous - There is no interaction between molecules adsorbed on neighbouring sites
<p>Freundlich¹³⁻¹⁵</p> $q_e = K_F C_e^{1/n}$ <p>K_F (mg/g) = is the Freundlich constant, which characterizes the strength of adsorption</p> <p>n ($0 < n < 1$) = Freundlich intensity parameter that reflects the magnitude of the adsorption driving force or surface heterogeneity</p>	<ul style="list-style-type: none"> - Empirical equation - Describes non-ideal and reversible adsorption - Assumes that as adsorbate concentration increases so too does the concentration of adsorbate on the adsorbent surface - May be used to describing heterogeneous systems - An infinite amount of adsorption can occur. - Favourable adsorption tends to have Freundlich constant n between 1 and 10. Larger value of n implies stronger interaction between adsorbent and adsorbate¹⁴ <ul style="list-style-type: none"> • $n \approx 1$ Linear adsorption isotherm • $1/n > 1$ concave curve (S-type) • $1/n < 1$ convex L-type - Unable to predict adsorption equilibria data at extreme concentration.
<p>Koble-Corrigan^{11,16}</p> $q_e = \frac{A C_e^n}{1 + B C_e^n}$ <p>q_e (mg/g) = amount of solute adsorbed</p> <p>C_e (mg/L) = equilibrium concentration of the solute in the bulk solution</p> <p>A, B, n = constants</p>	<ul style="list-style-type: none"> - Langmuir + Freundlich - Heterogeneous adsorption surface

Sips^{14,17}

$$q_e = \frac{K_S q_m C_e^n}{1 + K_S C_e^n}$$

q_e (mg/g) = amount of solute adsorbed

C_e (mg/L) = equilibrium concentration of the solute in the bulk solution.

q_m (mg/g) = maximum saturated monolayer adsorption capacity of the adsorbent

K_S (L/mg) = Sips isotherm constant

n = Sips isotherm exponent

- Langmuir + Freundlich
- Similar to Freundlich but differs on the finite limit of adsorbed amount at sufficiently high concentration
- Parameter n is regarded as the parameter characterising the system's heterogeneity
- At low adsorbate concentration, this model reduces to the Freundlich model, but at high concentration of adsorbate, it predicts the Langmuir model¹⁸

Redlich-Peterson^{11,14,19}

$$q_e = \frac{K_R C_e}{1 + a_R C_e^g}$$

q_e (mg/g) = amount of solute adsorbed

C_e (mg/L) = equilibrium concentration of the solute in the bulk solution

K_R (L/g) = Redlich-Peterson isotherm Constant

a_R (L/mg) = constant

g = exponent that lies between 0 and 1

- Langmuir + Freundlich isotherm
- Mechanism of adsorption is a hybrid and does not follow ideal monolayer adsorption
- Homogeneous and heterogeneous systems
- Represents adsorption equilibria over a wide concentration range
- Reduce to Langmuir isotherm when $g=1$
- Incorporate the characteristics of Langmuir and Freundlich isotherm into a single equation
- Limiting behaviour: Langmuir forms for $g=1$ and Henry's law form for $g=0$, and transforms into the Freundlich isotherm when K_R and $a_R \gg 1$ and $g=1$ ⁵
- If the g value is outside the range of 0-1, the data is not adequately explained by Redlich-Peterson equation⁵

BET^{20,21}

$$q_e = \frac{q_s \cdot C_{BET} \cdot C_e}{(C_s - C_e) \cdot [1 + (C_{BET} - 1) \cdot (C_e/C_s)]}$$

q_e (mg/g) = amount of solute adsorbed

C_e (mg/L) = equilibrium concentration of the solute in the bulk solution

C_{BET} (L/mg) = BET adsorption isotherm

C_s (mg/L) = adsorbate monolayer saturation concentration

q_s (mg/g) = theoretical isotherm saturation capacity

- Multilayer adsorption model
- No saturated value at high concentration. It can rise indefinitely
- Assumes that the first layer of adsorbate adsorbs on the surface with energy comparable to the heat of adsorption for monolayer adsorption and subsequent layer have
- equal energies

References

- (1) Lagergren, S. About the Theory of So-Called Adsorption of Soluble Substances. *K. Sven. Vetensk. Handl.* **1898**, 24 (4), 1–39.
- (2) Lemus, J.; Palomar, J.; Gilarranz, M. A.; Rodriguez, J. J. On the Kinetics of Ionic Liquid Adsorption onto Activated Carbons from Aqueous Solution. *Ind. Eng. Chem. Res.* **2013**, 52 (8), 2969–2976.
- (3) Largitte, L.; Pasquier, R. A Review of the Kinetics Adsorption Models and Their Application to the Adsorption of Lead by an Activated Carbon. *Chem. Eng. Res. Des.* **2016**, 1 (6), 495–504.
- (4) Plazinski, W.; Rudzinski, W.; Plazinska, A. Theoretical Models of Sorption Kinetics Including a Surface Reaction Mechanism: A Review. *Adv. Colloid Interface Sci.* **2009**, 152 (1–2), 2–13.
- (5) Tran, H. N.; You, S. J.; Hosseini-Bandegharai, A.; Chao, H. P. Mistakes and Inconsistencies Regarding Adsorption of Contaminants from Aqueous Solutions: A Critical Review. *Water Res.* **2017**, 120, 88–116.
- (6) Fan, H.-T.; Sun, W.; Jiang, B.; Wang, Q.-J.; Li, D.-W.; Huang, C.-C.; Wang, K.-J.; Zhang, Z.-G.; Li, W.-X. Adsorption of Antimony(III) from Aqueous Solution by Mercapto-Functionalized Silica-Supported Organic-Inorganic Hybrid Sorbent: Mechanism Insights. *Chem. Eng. J.* **2016**, 286, 128–138.
- (7) Mclintock, I. The Elovich Equation in Chemisorption Kinetics. *Nature* **1967**, 216, 1204–1205.
- (8) Luo, J.; Luo, X.; Crittenden, J.; Qu, J.; Bai, Y.; Peng, Y.; Li, J. Removal of Antimonite (Sb(III)) and Antimonate (Sb(V)) from Aqueous Solution Using Carbon Nanofibers That Are Decorated with Zirconium Oxide (ZrO₂). *Environ. Sci. Technol.* **2015**, 49 (18), 11115–11124.
- (9) Tan, K. L.; Hameed, B. H. Insight into the Adsorption Kinetics Models for the Removal of Contaminants from Aqueous Solutions. *J. Taiwan Inst. Chem. Eng.* **2017**, 74, 25–48.
- (10) Eris, S.; Azizian, S. Analysis of Adsorption Kinetics at Solid/Solution Interface Using a Hyperbolic Tangent Model. *J. Mol. Liq.* **2017**, 231, 523–527.
- (11) Shahbeig, H.; Bagheri, N.; Ghorbanian, S. A.; Hallajisani, A.; Poorkarimi, S. A New Adsorption Isotherm Model of Aqueous Solutions on Granular Activated Carbon. *World J. Model. Simul.* **2013**, 9 (4), 243–254.
- (12) Langmuir, I. The Constitution and Fundamental Properties of Solids and Liquids. Part I. Solids. *J. Am. Chem. Soc.* **1916**, 38 (11), 2221–2295.
- (13) Allen, S. J.; Mckay, G.; Porter, J. F. Adsorption Isotherm Models for Basic Dye Adsorption by Peat in Single and Binary Component Systems. *J. Colloid Interface Sci.* **2004**, 280 (2), 322–333.
- (14) Febrianto, J.; Kosasih, A. N.; Sunarso, J.; Ju, Y. H.; Indraswati, N.; Ismadji, S. Equilibrium and Kinetic Studies in Adsorption of Heavy Metals Using Biosorbent: A Summary of Recent Studies. *J. Hazard. Mater.* **2009**, 162 (2–3), 616–645.
- (15) Freundlich, H. M. F. Over the Adsorption in Solution. *J. Phys. Chem.* **1906**, 57, 385–471.
- (16) Koble, R. A.; Corrigan, T. E. Adsorption Isotherms for Pure Hydrocarbons. *Ind. Eng. Chem.* **1952**, 44 (2), 383–387.
- (17) Sips, R. Combined Form of Langmuir and Freundlich Equations. *J. Chem. Phys.* **1948**, 16, 490–495.
- (18) Ayawei, N.; Ebelegi, A. N.; Wankasi, D. Modelling and Interpretation of Adsorption Isotherms. *J. Chem.* **2017**, 2017.

- (19) Redlich, O.; Peterson, D. L. A Useful Adsorption Isotherm. *J. Phys. Chem.* **1959**, *63* (6), 1024.
- (20) K.Y. Foo, B. H. H. Insights into the Modeling of Adsorption Isotherm Systems. *Chem. Eng. J.* **2010**, *156*, 2–10.
- (21) Brunauer, S.; Emmett, P. H.; Teller, E. Adsorption of Gases in Multimolecular Layers. *J. Am. Chem. Soc.* **1938**, *60* (2), 309–319.

Annexe 5. COMPLEXATION CONSTANTS

Stripping agent		Reaction	Log K	Ref.
Sb(III)	Citric acid	$\text{Sb(OH)}_3 + \text{H}_3\text{Cit}^- = \text{Sb(OH)}_2(\text{HCit})^{2-} + \text{H}_2\text{O} + \text{H}^+$	0.1	1
		$\text{Sb(OH)}_3 + \text{H}_3\text{Cit}^- + \text{H}^+ = \text{Sb(OH)}_2(\text{H}_2\text{Cit})^- + 2\text{H}_2\text{O}$	4.6	
		$\text{Sb(OH)}_3 + 2\text{H}_3\text{Cit}^- + \text{H}^+ = \text{Sb(H}_2\text{Cit)}_2^- + 2\text{H}_2\text{O} + \text{H}^+$	-3.9	
	EDTA	$\text{Sb(OH)}_3 + 3\text{H}^+ + \text{EDTA}^{4-} = \text{SbEDTA}^- + 3\text{H}_2\text{O}$	26.77	2
		$\text{Sb(OH)}_3 + 4\text{H}^+ + \text{EDTA}^{4-} = \text{SbHEDTA} + 3\text{H}_2\text{O}$	28.00	
		$\text{Sb(OH)}_3 + 2\text{H}^+ + \text{EDTA}^{4-} = \text{SbEDTA(OH)}^{2-} + 2\text{H}_2\text{O}$	20.76	
		$\text{Sb(OH)}_3 + \text{H}^+ + \text{EDTA}^{4-} = \text{SbEDTA(OH)}_2^{3-} + \text{H}_2\text{O}$	12.68	
	Oxalic acid	$\text{Sb(OH)}_3 + \text{HOxa}^- = \text{Sb(OH)}_2\text{Oxa}^- + \text{H}_2\text{O}$	3.8	1
		$\text{Sb(OH)}_3 + 2\text{HOxa}^- = \text{Sb(Oxa)}_2^- + \text{OH}^- + 2\text{H}_2\text{O}$	-5.9	
	Tartaric acid	$\text{Sb(OH)}_3 + 3\text{H}^+ + \text{Tar}^{2-} = 3\text{H}_2\text{O} + \text{SbTar}^+$	9.85	2
		$\text{Sb(OH)}_3 + 3\text{H}^+ + 2\text{Tar}^{2-} = 3\text{H}_2\text{O} + \text{SbTar}_2^{2-}$	17.18	
		$\text{Sb(OH)}_3 + 2\text{H}^+ + \text{Tar}^{2-} = 2\text{H}_2\text{O} + \text{Sb(OH)Tar}^-$	9.41	
		$2\text{Sb(OH)}_3 + 2\text{H}^+ + 2\text{Tar}^{2-} = 4\text{H}_2\text{O} + \text{Sb}_2\text{H}_2(\text{OH})_2\text{Tar}_2^{2-}$	22.17	
		$\text{Sb(OH)}_3 + \text{Tar}^{2-} = 2\text{H}_2\text{O} + \text{SbH}_2(\text{OH)Tar}^{2-}$	2.05	
	Fe Surface complexation	$-\text{FeOH} + \text{Sb(OH)}_3 = -\text{FeOSb(OH)}_2 + \text{H}_2\text{O}$ (monodentate)	19.15 (HFO) 13.5 (goethite)	3
		$-\text{FeOH} + \text{Sb(OH)}_3 = -\text{FeOSbO(OH)}^- + \text{H}_2\text{O} + \text{H}^+$ (bidentate)	15.45 (HFO) 7.5 (Goethite)	
		$2-\text{Fe(OH)} + \text{Sb(OH)}_3 = (-\text{FeO})_2\text{Sb(OH)} + 2\text{H}_2\text{O}$ (bidentate binuclear)	15.16	4
		$-\text{Fe(OH)}_2 + \text{Sb(OH)}_3 = -\text{FeO}_2\text{Sb(OH)} + \text{H}_2\text{O} + \text{H}^+$ (Bidentate mononuclear)	7.59	

Sb(V)	Citric acid	$\text{Sb(OH)}_6^- + \text{H}_3\text{Cit}^- = \text{Sb(OH)}_4\text{H}_2\text{Cit}^- + \text{H}_2\text{O} + \text{OH}^-$	-6.5	5
		$\text{Sb(OH)}_6^- + \text{H}_2\text{Cit}^{2-} + \text{H}^+ = \text{Sb(OH)}_4\text{HCit}^{2-} + 2\text{H}_2\text{O}$	7.8	
		$\text{Sb(OH)}_6^- + \text{HCit}^{3-} + \text{H}^+ = \text{Sb(OH)}_4\text{Cit}^{3-} + 2\text{H}_2\text{O}$	8.0	
	EDTA	No complexation		6-8
	Oxalic acid	$\text{Sb(OH)}_6^- + \text{HOxa}^- = \text{Sb(OH)}_4\text{Oxa}^- + \text{H}_2\text{O}$	-6.4	5
	Tartaric acid	No complexation constant. Sb(V)-tartrate complexes more stable than antimonious acid in solution		9
	Fe Surface complexation	$-\text{Fe(OH)}_2 + \text{Sb(OH)}_6^- = -\text{FeO}_2\text{Sb(OH)}_4^- + 2\text{H}_2\text{O}$	5.21 (Goethite)	10
		$-\text{FeOH} + \text{Sb(OH)}_6^- = -\text{FeOSb(OH)}_5^- + \text{H}_2\text{O}$ (monodentate)	13.45 (HFO)	3
		$-\text{FeOH} + \text{Sb(OH)}_6^- = -\text{FeOSbO(OH)}_4^- + \text{H}_2\text{O} + \text{H}^+$ (bidentate)	13.85 (Goethite)	
		$2-\text{FeOH} + \text{Sb(OH)}_6^- = (-\text{FeO})_2\text{Sb(OH)}_4^- + 2\text{H}_2\text{O}$ (bidentate binuclear)	4.15 (HFO)	
		$-\text{Fe(OH)}_2 + \text{Sb(OH)}_6^- = -\text{FeO}_2\text{Sb(OH)}_4^- + 2\text{H}_2\text{O}$ (Bidentate mononuclear)	5.20 (Goethite)	4
Fe	Citric acid	$\text{Fe}^{2+}: \text{Fe}^{2+} + \text{Cit}^{4-} = \text{FeCit}^{2-}$	4.4	11
		$\text{Fe}^{2+} + \text{HCit}^{3-} = \text{FeHCit}^-$	2.65	
		$\text{Fe}^{3+}: \text{Fe}^{3+} + \text{Cit}^{4-} = \text{FeCit}^-$	11.50	11
		$\text{Fe}^{3+} + \text{HCit}^{3-} = \text{FeHCit}$	24.84	
		$\text{Fe}^{3+} + 2\text{Cit}^{4-} = \text{FeCit}_2^{5-}$	32.73	12
		$\text{Fe}^{3+} + 2\text{Cit}^{4-} + \text{H}^+ = \text{FeH(Cit)}_2^{4-}$	38.74	
		$\text{Fe}^{3+} + 2\text{HCit}^{3-} = \text{FeH}_2\text{Cit}_2^{3-}$	43.53	
	$2\text{Fe}^{3+} + \text{Cit}^{4-} = \text{Fe}_2\text{Cit}_2^{2-}$	48.0		

Fe	EDTA	$Fe^{2+}: [Fe(H_2O)_6]^{2+} + EDTA^{4-} = [Fe(EDTA)]^{2-} + 6H_2O$	14.33	13
		$Fe^{3+}: [Fe(H_2O)_6]^{3+} + EDTA^{4-} = [Fe(EDTA)]^{-} + 6H_2O$	25.10	
	Oxalic acid	$Fe^{2+}: Fe^{2+} + Oxa^{2-} = FeOxa$	3.05	11
	$Fe^{2+} + 2Oxa^{2-} = FeOxa^{2-}$	5.15		
	$Fe^{3+}: Fe^{3+} + Oxa^{2-} = FeOxa^{+}$	7.59		
	$Fe^{3+} + 2Oxa^{-} = FeOxa^{2-}$	13.64		
	Tartaric acid	$Fe^{2+}: Fe^{2+} + Tar^{2-} = FeTar$	1.43	11
		$Fe^{2+} + 2Tar^{2-} = FeTar_2^{2-}$	2.50	
		$Fe^{3+}: Fe^{3+} + Tar^{2-} = FeTar^{+}$	5.73	
		$2Fe^{3+} + 2Tar^{2-} = Fe_2(H_{-1}Tar)_2 \cdot 2H$	10.9	
		$3Fe^{3+} + 3Tar^{2-} = Fe_3(H_{-2}Tar)_3 \cdot 6H$	9.5	

References

- (1) Tella, M.; Pokrovski, G. S. Antimony(III) Complexing with O-Bearing Organic Ligands in Aqueous Solution: An X-Ray Absorption Fine Structure Spectroscopy and Solubility Study. *Geochim. Cosmochim. Acta* **2009**, *73* (2), 268–290.
- (2) Filella, M.; May, P. M. Critical Appraisal of Available Thermodynamic Data for the Complexation of Antimony(III) and Antimony(V) by Low Molecular Mass Organic Ligands. *J. Environ. Monit.* **2005**, *7* (12), 1226–1237.
- (3) Guo, X.; Wu, Z.; He, M.; Meng, X.; Jin, X.; Qiu, N.; Zhang, J. Adsorption of Antimony onto Iron Oxyhydroxides: Adsorption Behavior and Surface Structure. *J. Hazard. Mater.* **2014**, *276*, 339–345.
- (4) Vithanage, M.; Rajapaksha, A. U.; Dou, X.; Bolan, N. S.; Yang, J. E.; Ok, Y. S. Surface Complexation Modeling and Spectroscopic Evidence of Antimony Adsorption on Iron-Oxide-Rich Red Earth Soils. *J. Colloid Interface Sci.* **2013**, *406*, 217–224.
- (5) Tella, M.; Pokrovski, G. S. Antimony(V) Complexing with O-Bearing Organic Ligands in Aqueous Solution: An X-Ray Absorption Fine Structure Spectroscopy and Potentiometric Study. *Mineral. Mag.* **2008**, *72* (1), 205–209.
- (6) Kolbe, F.; Mattusch, J.; Wennrich, R.; Weiss, H.; Sorkau, E.; Lorenz, W.; Daus, B. Analytical Investigations of Antimony-EDTA Complexes and Their Use in Speciation Analysis. *Fresenius Environ. Bull.* **2012**, *21* (11 C), 3453–3456.
- (7) Hansen, C.; Schmidt, B.; Larsen, E. H.; Gammelgaard, B.; Stürup, S.; Hansen, H. R. Quantitative HPLC-ICP-MS Analysis of Antimony Redox Speciation in Complex Sample Matrices: New Insights into the Sb-Chemistry Causing Poor Chromatographic Recoveries. *Analyst* **2011**, *136* (5), 996–1002.
- (8) Hansen, H. R.; Pergantis, S. A. Analytical Techniques and Methods Used for Antimony Speciation Analysis in Biological Matrices. *J. Anal. At. Spectrom.* **2008**, *23*, 1328–1340.

- (9) Gate, S. H.; Richardson, E. Some Studies on Antimonic Acid—II. *J. Inorg. Nucl. Chem.* **1961**, *23* (3–4), 265–273.
- (10) Leuz, A. K.; Mönch, H.; Johnson, C. A. Sorption of Sb(III) and Sb(V) to Goethite: Influence on Sb(III) Oxidation and Mobilization. *Environ. Sci. Technol.* **2006**, *40* (23), 7277–7282.
- (11) Martell, A. E.; Smith, R. M. *Critical Stability Constant 3. Other Organic Ligands*; 1977.
- (12) Silva, A. M. N.; Kong, X.; Parkin, M. C.; Cammack, R.; Hider, R. C. Iron(III) Citrate Speciation in Aqueous Solution. *Dalt. Trans.* **2009**, *40*, 8616–8625.
- (13) Harris, D. C. *Quantitative Chemical Analysis*, 9th ed.; WH Freeman.